SHEAR BAND NUCLEATION AND INDENTATION SIZE EFFECT IN METALLIC GLASS

SONG WANG

Ph.D

The Hong Kong Polytechnic University

2015

The Hong Kong Polytechnic University
Department of Mechanical Engineering

Shear Band Nucleation and Indentation Size Effect in Metallic Glass

Song WANG

A thesis submitted in partial fulfilment of the requirements for the degree of Doctor of Philosophy

May 2015

CERTIFICATE OF ORIGINALITY

I hereby declare that this thesis is my own work and that, to the best of my knowledge and belief, it reproduces no material previously published or written, nor material that has been accepted for the award of any other degree or diploma, except where due acknowledgement has been made in the text.

(Signed)

Song WANG (Name of the student)

Dedication

This dissertation is dedicated with love to my parents and my wife, who always support my research studies and bring the greatest joy and encouragement into my life.

Abstract

Since the Bronze Age, the search for strong-and-ductile metals has been one of the central themes in all kinds of tool-making activities. After centuries of dedicated efforts, plasticity in crystalline metals has now been well understood; however, it still remains unclear in many fundamental aspects for amorphous metals, i.e. metallic-glasses. Despite the absence of microstructural features, metallic glasses (MGs) could display size-dependent hardness at the submicron scale. While most early studies attributed this size effect to Weibull statistics, here I proposed a shear-band nucleation controlled mechanism giving rise to a deterministic indentation size effect in MGs. In line with this mechanism, an explicit relation is derived linking the size dependency of hardness to a critical shear-band nucleation length in MGs. Through a series of carefully designed spherical indentation tests, this mechanism is experimentally justified, from which we are able to extract the shear-band nucleation lengths for a Zr-based MG at different indentation strain rates. On the basis of the combined theoretical/experimental efforts, our current work provides quantitative insights into the shear-band nucleation mechanism in MGs.

Then spherical indentation was also conducted on the bent MG samples to study the effect of residual stress on the shear band nucleation. The Young‘s modulus was

measured via the Joslin-Oliver based Berkovich nanoindentation approach. It is shown that the elastic modulus keeps at a constant while its hardness drops more significantly in the compression region than that in the tension region. The trend of indentation size effect for varies residual stress was found. It is obvious that the shear band nucleation in the Zr-based MG influenced by the presence of compression or tension residual stress, which can be rationalized by the different shear softening rate in MGs. Spherical indentation was further carried out on the ribbon and annealed MG samples to explore the thermal history effect on shear band nucleation. The hardness increases with annealing time and the ribbon one lower than the other three, demonstrating that denser structure has a higher hardness. Meanwhile, with the increasing annealing time, the Young's modulus increases. We can found that thermal history effect on the nucleation length which is not caused by the significantly change the softening rate, but the variation of Young's modulus.

At last, various MGs with nine different spherical indenters were studies by spherical nanoindentation. The size effect is same as previous findings for large indenters while the reverse size effect was found for smaller ones. And the changing point is different for different MGs. Also the shear band nucleation length is correlated with the fragility and Poisson's ratio. The MGs with a higher fragility and Poisson's ratio represent a higher possibility for a BMG to have better plasticity and to form shear band.

Acknowledgements

I would like to express my appreciation to my chief supervisor Professor Sanqiang Shi, for his supervision and support throughout my Ph.D. study. Also I would like to express my sincere gratitude to my co-supervisor Professor Yong Yang. I thank him for choosing me as his Ph.D. student. I am so grateful for his valuable guidance, patience and constant encouragement throughout the whole period of my research work. Without his broad knowledge and academic insight, I will not finish my Ph.D. study successfully.

I am grateful to all those who have helped me during my Ph.D. study, specially Dr. Qing Wang, Dr. Jifang Zeng, Dr. Jianchao Ye , Dr. Baoan Sun, for their friendship, help and suggestion on my experiments. Moreover, I would also like to thank Dr. Haibo Ke, Dr. Xiaoling Fu, Yifan Ye and Yumiao Lu for their great help and assistance during my whole study. There has been full of unforgettable memories and warm friendships with all of you in my life at PolyU.

I would like to thank Mr. M. N.Yeung and Dr. Hardy Lui from Materials Research Center of the Hong Kong Polytechnic University for their technical assistance. Special thanks go to the staffs in the Electron Microscope Unit of the Hong Kong University including Frankie, Amy, who provided technical supports to my research.

Last but not least, I give my appreciation to my parents and wife for the support, love and encouragement during the tough time in the research.

Table of contents

List of Tables

List of Figures

1 Introduction and literature review

1.1 Introduction of metallic glass

Metallic glass is a type of non-crystalline (amorphous, disordered) metallic alloys lacking long-range periodicity of the atomic arrangement. The first metallic glass, produced over fifty years ago by Pol Duwez(W. Klement 1960, Willens 1963) at the California Institute of Technology , was discovered by rapid quenching of Au- Si binary metallic melts at a very high cooling rate (approximately 106K/s). As atoms don't have enough time to rearrange for crystal nucleation, the liquid reaches the glass transition temperature, Tg, and solidifies as a metallic glass. The metallic glass so obtained is less brittle than oxide glass and looks like a metal. Its amorphous structure was metastable and could be converted into crystalline phase after annealing.

Early glass-forming alloys had to be cooled extremely rapidly to avoid crystallization. An important drawback of this was that metallic glasses could only be fabricated in the forms of thin sheets or ribbons of micron size. In the 1970's, Chen(Chen 1974) demonstrated the casting of millimeter diameter rods of Pd-Cu-Si alloy at significantly low cooling rates in the range of 10^3 K/s. In the 1990s, however, new alloys were developed that form glasses at cooling rates as low as 1 K/s(Inoue and Takeuchi 2002, Johnson 1999)，enabling the metallic glasses cast into parts of up to several centimeters in thickness while remaining an amorphous structure.

The amorphous atomic structure of metallic glasses provides many outstanding mechanical properties compared to crystalline counterparts. It is of current interest and significance in several fields, such as physics, materials science and chemistry because of its unique disordered structural and superb mechanical, applicable physical and chemical properties(Greer 1993, Loffler 2003). Metallic glasses also provide new insights into our fundamental understanding of liquids and glasses. The combination of the unique mechanical properties(Byrne and Eldrup 2008, Cheng and Johnson 1987, Spaepen 1987, Dyre 2008, Greer 1993, Loffler 2003) with easy shaping provides the potential for next generation of structural materials in a variety of industries including aerospace and aeronautics, high-performance sports equipment, armor and microelectromechanical systems devices, biomedical, and conventional structural applications(Johnson 2002).

Metallic glass absorbs less energy upon stress induced deformation through damping and returns more by rebounding elastically to its initial shape. With no crystal defects, metallic glasses have very high yield strength and very high elastic limit. The elastic strain of metallic glass can support in tension or in bending is almost double that of a commercially available crystalline material. Metallic glasses are premier spring materials. They have very high fracture strength coupled with 2-3% of elastic strain. Conventional aluminum, titanium alloys and steels can sustain 1-2% of elastic strain. The high corrosion resistance of metallic glasses is contrary to expectation, as they are in a higher energy state. The absence of grain boundaries and defects and their chemical

homogeneity confer on them high corrosion resistance. The composition of the glass plays an important role. Cr, Mo and P can enhance corrosion resistance as has been revealed in many early studies on melt spun ribbons. High electrical resistivity leads to low eddy current losses. Easy magnetization and demagnetization allows lower losses in applications.

Unlike their crystalline counterparts, metallic glasses typically exhibit limited ductility and essentially no work hardening. Unconstrained deformation modes such as tension typically produce fracture immediately upon reaching the yield stress in nearly all metallic glasses via the initiation and propagation of highly localized deformation zones (i.e., shear bands) with minimum thickness of tens of nanometers. Understanding shear band initiation and propagation, therefore, is of great importance in advancing our knowledge of deformation in non-crystalline materials in general, while the application of metallic glasses will require careful control and manipulation of this deformation mechanism.

1.2 Fabrication of metallic glasses

Bulk metallic glasses can be synthesized by solidification or by solid state processing, a drastic change from the rapid solidification techniques previously employed for

synthesis of conventional alloys. At first, the technique in solidification route is water-quenching. In this method the alloy is melted in a vacuum-sealed quartz tube and is then water-quenched. Cooling rate available in this technique generally varies in the range of 10-100Ks^{-1}. Because of the free flow of the liquid metal under pressure, the cross section of the solidified metal layer obtained by the gun technique of rapid solidification is not uniform because of the free flow of the liquid metal under pressure. To overcome this drawback, a number of other ways were developed to improve the uniformity of the cross section of the solidified layers. The most significant milestone in this direction was the development of the chill block melt-spinning technique in the 1970s and several of its variants. With the introduction of these techniques, there was a rapid progress in this field, and the technology of rapid solidification processing has come to stay as an important branch of materials science and engineering. It will be difficult to describe all the different techniques that were developed to achieve high solidification rates in metallic melts, so here I will describe only the melt-spinning technique. This has been the most popular technique of rapid solidification processing used by a number of researchers all over the world. Its main advantages are that (1) it will be possible to produce ribbons of uniform cross section, (2) its process parameters have been optimized, and (3) melt spinners are commercially available. Modern techniques of preparing bulk metallic glasses involve unidirectional zone melting, arc melting and then injection molding or suction casting in a copper mold. This process has got many variants. The melt can be electromagnetically levitated and then cast into copper mold. Conner *et al*(Conner, Dandliker and Johnson 1998) have reported the

synthesis of bulk metallic glass composites by introducing tungsten, steel and silicon carbide fiber or particles into amorphous matrix. The reinforcements do not act as heterogeneous nucleation sites and mechanical properties of the composite are better than those of the bulk glass.

Die casting is a common method to produce different types of castings in the industry. Compared with the conventional sand-casting methods, die casting methods offer higher solidification rates (because heat is extracted more rapidly by the metal mold) and more complex shapes can also be produced. Therefore, this method has been used by several researchers to synthesize BMGs in different alloy systems.

1.3 Atomic structures in metallic glasses

The physical properties of amorphous alloys are determined by the short-range atomic arrangement which cannot be easily determined experimentally (cite the work of Prof. Chen M.W. in Nat Mater and Science here). To determine the amorphous structure of metallic glasses, a lot of models were proposed by different method. Three models (Free volume conception, dense random packing of hard sphere model, Miracle's model) are discussed here. There are also many other models such as tight-bond cluster model(Fan, Liaw and Liu 2009) and core-shell model(Ye et al. 2010a) etc.

1.3.1 Free volume

The concept of free-volume goes back a long time. For polymer materials, it was presumed that the viscosity of a material was strongly related to its free volume. The idea of free volume for metallic glass was proposed by Cohen(Cohen 1980) and Turnbull(Turnbull 1961). The key point of this conception was the viscosity of a liquid highly correlates to its volume. The total volume of a metallic glass can be separated into the space occupied by the dense atomic clusters and the empty space among these atomic clusters due to packing frustrations. Different from a gas, a liquid is a densely packed matter in which an atom is located in the "cage" constituted by the neighboring atoms. Most of the time, an atom that is fixed in the "cage" cannot move from one place to another Only if it gets enough space, larger than a critical volume ***v****, next to the atom, the atom can jump into this space (or free volume), shown in Figure 1.1.

The diffusivity is given by [63]

$$D = D(v^*)\int_{v^*}^{\infty} p(v)dv = D(v^*)exp\left(-\frac{\gamma v^*}{v_f}v^*\right) \tag{1.1}$$

where $p(v)$ is the probability distribution of space between atoms, γ is a constant of order of unity and v_f is the total free volume.

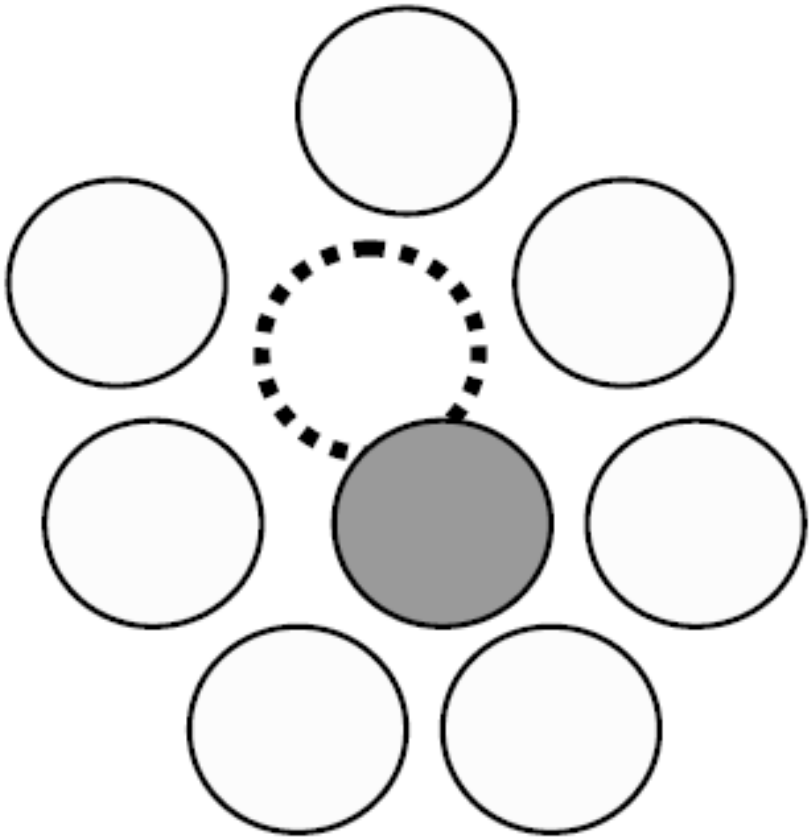

Figure 1.1 Schematic of free-volume for an atom to move into

For most of molecular liquids, the magnitude of v^* is around 80% of the atomic volume, close to the atomic volume itself, but it is only about 10% for metallic glass. For crystal materials, the lattice structure will not be changed while the volume expands only due to the vibration of atoms during heating while no phase transformation

occurred. By contrast, the structure and volume of a liquid shows significant temperature dependence. There is some difference in the structure change at different temperatures. At the temperature higher than T_g, the slope of volume change as a function of temperature is steeper than the one of the temperature lower than T_g, which reflects that above T_g the changes in the structure with temperature change occur quickly while below T_g, however, the kinetics of changes slows down. Below a certain temperature, the change becomes so sluggish that the structure appears to be frozen because of "kinetic arrest." While the metallic glass annealed below T_g, the structure will be slowly relaxed from an energetically higher metastable state towards an energetically lower metastable state(Chen 1980) with a decrease of free volume and correlated changes in topological and chemical short-range order (SRO).

The free volume theory was also used to explain plastic flow during deformation (Spaepen 1977a, Steif, Spaepen and Hutchinson 1982). However, free volume cannot induce shear deformation by itself, although atoms could move because of diffusion. The basic conception is that shear bands need free space to operate. Therefore, the free volume controls shear flow. However, the assumption is only for hard-sphere models, and elastic bodies can undergo local shear without volume changes. Furthermore, plastic deformation induces free volume in the shear bands(Yang et al. 2005).

1.3.2 Dense random packing and Bernal's model

The dense random packing model was proposed by Bernal(Bernal 1960), The atomic arrangement is determined by purely geometrical sphere packing, the atomic structure was determined based on the dense random packing which is restricted by the principle that two atoms cannot come closer than one atomic diameter using ratios of atomic radii. Bernal's idea can result in a satisfactory model for monatomic metals and alloys in which constituent species have comparable atomic sizes the atomic arrangement of a simple liquid is determined by volume exclusion.

Glasses are not truly a random distribution of atoms because no two atoms can be closer than a typical bonding distance or farther apart than a few nearest neighbors. This distribution of atoms gives rise to a diffuse intensity peak in X-ray, neutron and electron scattering experiments. However, glasses still exhibit some short-range order of the atoms. Structural information on short-range order is typically obtained from the pair correlation function.

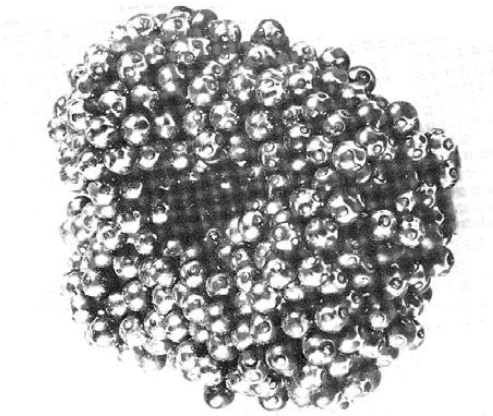

Figure 1.2 A laboratory-constructed random close packing of hard-spheres shows no lattice ordering

The random close packing model structure is illustrated in Figure 1.2. It is obvious that the structure reveals no crystallinity. Although it is simple, this model demonstrated many of the structure features of simple liquids, and provided excellent explanation of super cooling, nucleation, melting, fluidity and diffusion. Bernal's model is satisfied for monatomic metals and alloys in which constituent species have comparable atomic sizes. But the drawback is that there is no deep insight into the short-range and medium-range ordering which is important for this kind of material. Moreover, this model fails to describe metal-metalloid-based alloys in which the chemical SRO is pronounced.

The random close packing model was further developed by Finney(Finney 1970) who made a large model with 7994 atoms.

1.3.3 Miracle's model

Miracle (Miracle and Senkov 2003a, Miracle and Senkov 2003b, Sheng et al. 2008) reported an atomic structure model for metallic glasses which is based on a new sphere-packing scheme -the dense packing of atomic clusters. Random positioning of solvent atoms and medium-range atomic order of solute atoms are combined to reproduce diffraction data successfully over radial distances up to ~1 nm. The model describes a structural model for metallic glasses that extends well beyond the nearest- neighbor shell.

The primary atomic cluster is constituted by the largest, primary solute atom α wrapped by the solvent atoms Ω. The preferred size of primary clusters is determined by using the discrete solute to solvent radius ratio R' which satisfies an efficient solute centered packing in the local cluster. The cluster ordering provides two additional topological species, which is a secondary solute β sitting in an octahedral cavity and a tertiary solute γ sitting in a tetrahedral interstice. This means that only three topologically distinct solutes are contained in a metallic glass. All solutes satisfying the ratio R' (solute radius/solvent radius) can be efficiently packed in the first coordination shell. Hence, only in the first coordination shell, the clusters are densely packed to form a structure of overlapping clusters. If the difference of atomic radius between two solutes is within ±2%, these two solutes can be considered as topologically equivalent. This model presents not only the short-range order; medium-range atomic order up to

~1 nm can also be explained.

The dense cluster-packing model includes both size and chemical effects, and is summarized by these features: (i) efficiently packed solute-centered atomic clusters with solvent atoms only in the first coordination shell are densely packed to form a structure of overlapping clusters; (ii) three topologically distinct solutes exist: primary cluster-forming solutes (α), cluster-octahedral solutes (β) and cluster-tetrahedral solutes (γ); (iii) all solutes possess radius ratios relative to the solvent, R^*, that enable efficient atomic packing in the first coordination shell; (iv) face-sharing of adjacent clusters is preferred to minimize volume, but edge- and vertex-sharing may exist to reduce internal strains; (v) solutes with atomic radii within ±2% of one another are considered topologically equivalent; and (vi) no orientational order exists between clusters. The dense cluster-packing model is consistent with the full range of phenomenological guidelines established for metallic glasses.

1.4 Mechanical behavior of metallic glass

1.4.1 The mechanical properties of metallic glasses

Despite their very high strength, hardness and elastic limit, monolithic metallic glasses (MGs) rarely show macroscopically observable tensile ductility at room temperature owing to the severe plastic strain location in a narrow region called the shear band. The resultant catastrophic and instantaneous brittle failure extremely impedes their exploitation as structural engineering material. However, several research groups(Guo et al. 2007b, Jang and Greer 2010, Wu, Zhang and Mao 2009a, Greer and De Hosson 2011) recently reported that when the sample dimensions are brought into sub-micrometer or nanometer range, the strength, tensile plasticity and even the deformation mode can be remarkably changed, offering another promising way to utilize feature size as a design parameter in attaining superior mechanical properties for MGs.

In the recent work by Wu and Li et al (Wu et al. 2009), tensile tests were carried out on micrometer sized Co based amorphous wires. It was found that nonlinear deformation with appreciable elongation takes place during tensile testing. These investigators believed that the deviation from linear deformation after the apparent yield could be attributed to the formation of sub-nanometer voids agglomerated from flow defects. Furthermore, they reported that amorphous wires with smaller diameters exhibit a lower apparent yield stress, which might be caused by smaller STZ (shear

transformation zone) energy barriers due to faster cooling rates applied in thinner amorphous wires.

Meanwhile, the works of Zberg and coworkers(Zberg et al. 2009) demonstrated that Mg based glassy wires reveal significant amounts of homogeneous plastic deformation in tension before final necking of the fracture zone and inhomogeneous plastic deformation occur, which was explained by a combination of small diameter, high axial symmetry and high free volume content of the rapidly solidified metallic glassy wires. In fact, the Weibull analysis of tensile property reliability showed a surprisingly high Weill modulus of 20.58 at a characteristic strength of 817 MPa. The correlation of the Weibull statistics was better for size correction proportional to the surface area, indicating that surface defects are the more crucial defects. Therefore, the extended amount of homogenous plastic deformation can be assigned to the circular geometry and flawless surface quality of the specimens and the high Weibull modulus is related to the plastic behavior and necking in the tensile tests.

The above observations suggest that the sample size might strongly affect the deformation mechanism and thus the tensile mechanical properties of small-volume metallic glasses.

Using in-situ tensile straining tests in a transmission electron microscope, Guo et

al(Guo et al. 2007b) observed the entire sequence of deformation stages of several monolithic $Zr_{52.5}Cu_{17.9}Al_{10}Ni_{14.6}Ti_5$ metallic-glass samples with dimensions of the order of 100nm. Notably, they found qualitatively different behavior in small-volume metallic glasses, including significant uniform elongation with large tensile ductility in the range of 23-45% and extensive necking or stable shear, as illustrated Figure 1.3. Moreover, this large plasticity did not result from the branching/deflection of shear bands or the presence of nanocrystals, suggesting that monolithic glassy alloys can deform plastically like their crystalline counterparts, via inhomogeneous or homogeneous flow without catastrophic failure. An possible explanation of such sample size-effect matters is that nanometer sized samples may contain fewer flaws, which reduces the probability of localized shear bands forming and thus enables multiple atomic-level shear events to occur throughout the sample. In addition, catastrophic crack propagation cannot happen, as there is an associated critical length-scale for brittle failure that is much larger than the sample. In other words, sample-size effects can suppress catastrophic localization and failure in small-volume specimens.

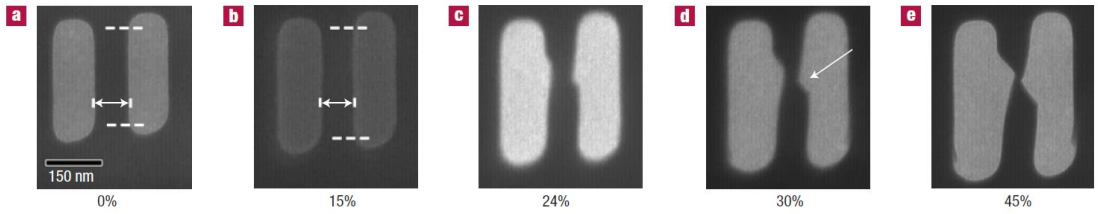

Figure 1.3 Sample at various stages of tensile elongation during the in situ TEM experiment (Guo, et al. 2007a). The straight gauge section is marked with dashed white lines (average strain rate: ~ $5\times10-4s^{-1}$) a, the virgin sample before testing. b -e, Up to a strain of 15%, sample was uniformly elongated, then non-uniform deformation occurs, with a significant elongation in the necked region indicated by the white arrow. The total tensile strain reached 45%.

More recently, Jiang and Greer (Greer and De Hosson 2011) examined the size-dependent mechanical properties of a $Zr_{35}Ti_{30}Co_6Be_{29}$ metallic glass under tension through transmission electronic microscopy. The in-situ tensile tests were carried out on fabricated in non-tapered, free standing specimens. It was found that the tensile yield strength increases by 50% upon reducing the sample size down to 500nm, below which it remains at a constant value of 2.25GPa. Additionally, when sample size approaches 100nm, a highly localized to homogeneous deformation mode change occurs without any change in the yield strength (see Figure 1.4). Interestingly, it was therefore demonstrated that strength and ability to carry plasticity are decoupled at the nanoscale, as indicated by the separate and distinct critical sizes for maximum strength and for the brittle-to-ductile transition. These phenomena may be understood by considering two competing process: crack-like shear-band propagation versus homogeneous flow and

the contribution of each process to the overall deformation at different sample sizes.

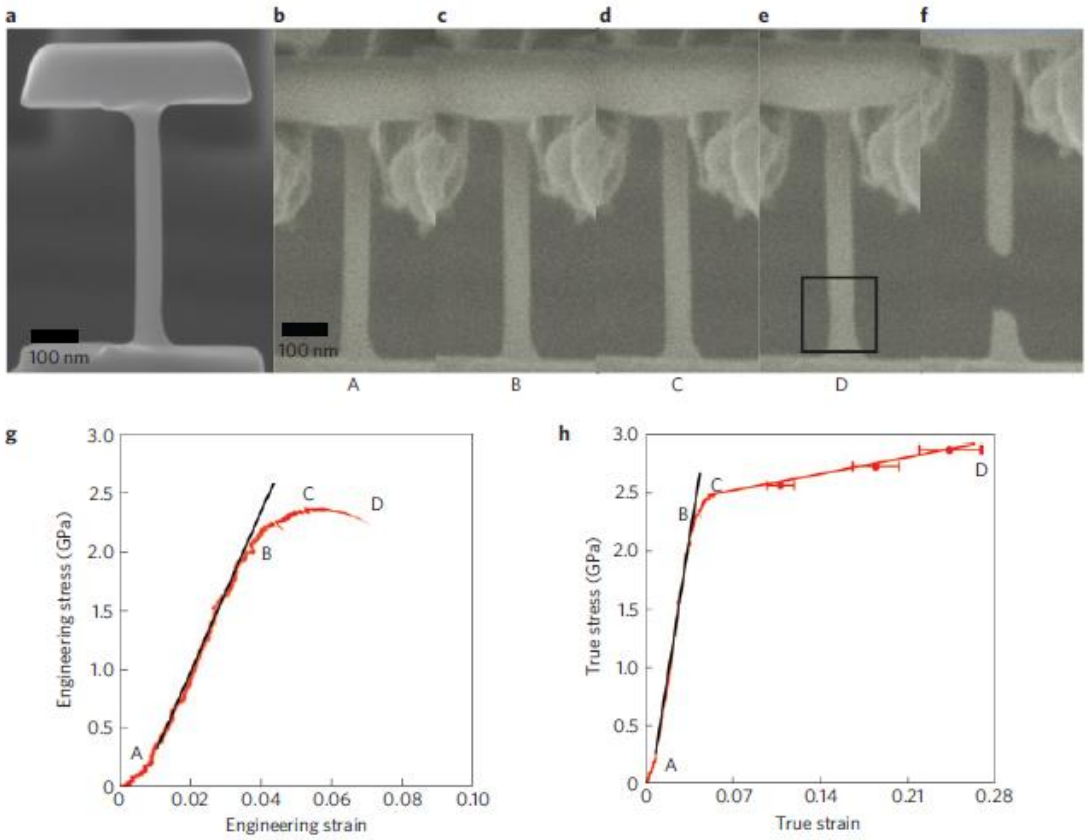

Figure 1.4 Monotonic nanotension results for the 100-nm-diameter specimen. a, SEM image of a typical as-fabricated 100-nm-diameter tensile sample.b–f, Images captured from a movie recorded during an in situ tension test at "E of 0 (b), 0.04 (c), 0.06 (d), 0.07 (e) and the final fracture (f). The square in e indicates the region where a neck is formed. The engineering (g) and true (h) stress–strain curves of the nanotension test. True stresses and strains after necking were obtained by directly measuring the diameter in the necked region. The error bars in h reflect the uncertainty in measuring pillar dimensions on the captured images of the movie. The value of strain in g and h has no units.

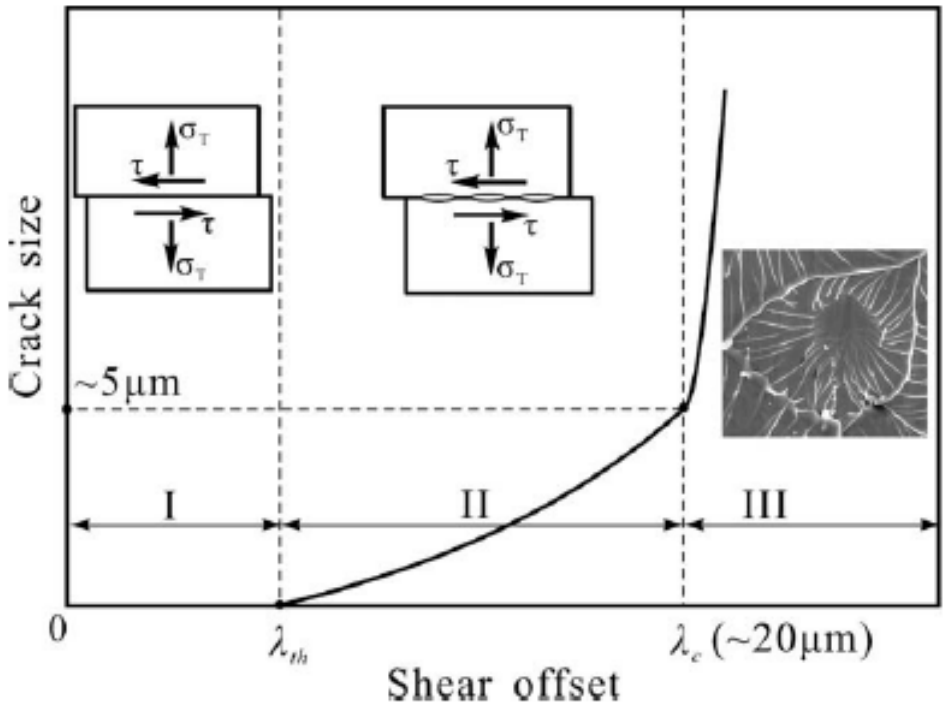

Figure 1.5 Illustration of the crack size as a function of shear offset, showing the three stages in the tensile fracture processes of the $Zr_{52.5}Cu_{17.9}Al_{10}Ni_{14.6}Ti_5$ metallic glass: region I, the multiplication of free volume; region II, the coalescence of free volume; region II, the coalescence of free volume and formation of void; region III, the final fast propagation of shear crack.(Wu, Zhang and Mao 2009)

In fact, the size-dependent shear fracture and plasticity have also been investigated by Wu et al(Wu et al. 2009a), who performed experiments in tension on a $Zr_{52.5}Cu_{17.9}Al_{10}Ni_{14.6}Ti_5$ metallic glass. These authors demonstrated that the tensile ductility depends strongly on the critical shear offset. Moreover, the tensile fracture process can be divided into three stages: multiplication and coalescence of the free

volume, formation of voids, and the final fast propagation of a shear crack (see Figure 1.5). Accordingly, the size effect on the tensile shear deformation processes of metallic glass can be well understood: with decreasing specimen size smaller than the equivalent critical shear offset, the shear deformation of metallic glass is changed from unstable to stable, which leads to a transition from global brittleness on the macroscale to large global plasticity or even necking on the microscale, as illustrated in Figure 1.6.

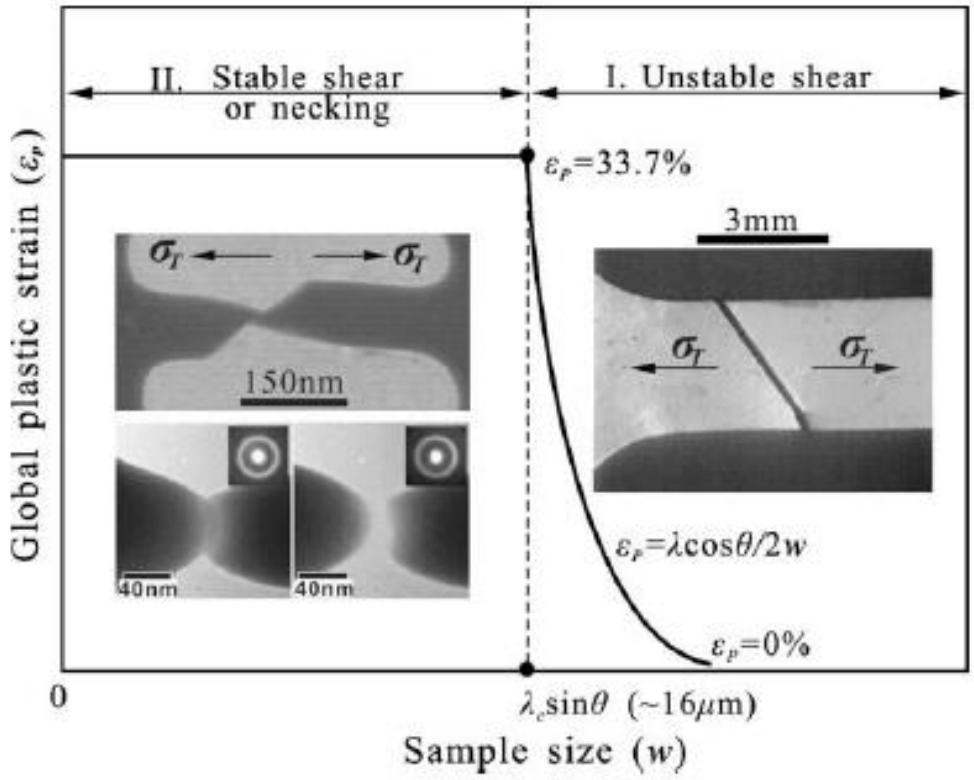

Figure 1.6 Illustration of the size effect on the tensile plasticity or brittleness of metallic glass: region I, the unstable shear region (inset is the optical image of tensile specimen of metallic glass with large dimension(Pampillo 1975)); region II, the stable shear region (insets are the typical stable shear and necking of the TEM in situ tensile specimen with a gauge dimension of ~100 nm×100 nm×250 nm(Guo et al. 2007a)).

1.4.2 Deformation mechanism

1.4.2.1 Free volume theory

Free volume model, which was developed by Turnbull and Spaepen(Turnbull 1961, Spaepen 1977a)., views plastic deformation as a series of discrete atomic jumps in the glass, similar as diffusion, these jumps are obviously favored near sites of loose packed region which can more readily accommodate inelastic deformation. Some activation energy of atom jump motion ΔG^m must be supplied. If there is no force applied, the number of atom jumps across the energy barrier caused by the thermal fluctuations is equal in both directions at room temperature. When an external force is applied to the system, the atomic jumps are biased in the direction of the force and the number of forward jumps larger than the number of backward ones, which enables the macroscopic flow.

The steady-state deformation in metallic glasses is a competition between the free volume created by the stress-driven process and diffusive annihilation. The energy necessary to squeeze an atom with volume v^* into a smaller hole of volume can be approximated by the elastic distortion energy required to squeeze a sphere with volume v^* into a spherical hole with volume v in matrix of the same material. At low temperatures, at which the diffusion process of such activation dilatation caused by the plastic deformation may be very slow, the shear regions can sustain a large amount of shear induced excess free volume. This leads to lowering the deformation resistance,

and thus shear-softening.

The general flow equation is described as

$$\dot{\gamma} = 2\nu\Delta f \exp\left(-\frac{\alpha v^*}{v_f}\right) \exp\left(-\frac{\Delta G^m}{kT}\right) \sin\left(-\frac{\tau\Omega}{kT}\right) \quad (1.2)$$

where Δf is the volume fraction, f is the frequency of atomic vibration (~Debye frequency), k is the Boltzmann constant, T is the temperature, α is a geometrical factor between 1 and 0.5, Ω is the atomic volume and v_f is the average free volume of an atom.

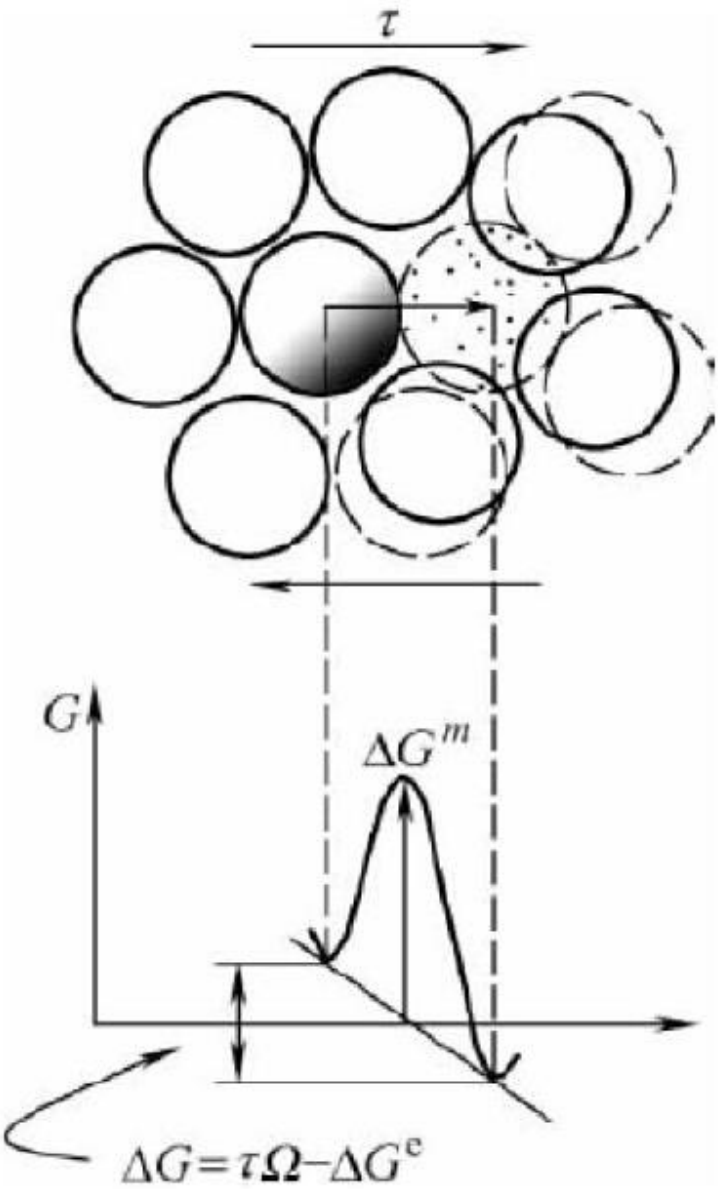

Figure 1.7 A pictorial representation of the free volume flow process

The free volume theory provides simple and clear explanations of the strain softening and thereby heterogeneous deformation behavior of metallic glasses. The theory widely cited to study various mechanical behaviors of metallic glasses. However, they are unable to quantitatively describe the strength and ductility of BMGs.

1.4.2.2 Shear transformation zone model

The shear transformation zone (STZ) originally proposed by Argon(Argon 1979a). It has been accepted as a flow unit, which underlies the deformation of metallic glasses. The STZ is essentially a local cluster of atoms that undergoes an inelastic shear distortion from one relatively low energy configuration to another low-energy configuration, crossing an activation barrier. Generally, thermally activated STZs initiate around free-volume sites under an applied shear stress because high elastic strain at free-volume sites energetically promotes STZ formation. This STZ activation involves a redistribution of free volume within the atomic cluster. This free volume redistribution is a transient process, which is believed to involve local, permanent changes to the excess free volume. The accumulation of excess free volume is believed to facilitate shear localization through local softening in the vicinity of previously deformed regions.

Derived from the energy landscape theory and Frenkel's work for the shear deformation of defect-free crystals, Johnson and Samwer proposed a cooperative shearing model (CSM) for STZs (Johnson and Samwer 2005a). The Johnson-Samwer model was originally introduced to illustrate the relationship between the temperature and yield strength in the form of $T^{2/3}$, it provides an effective interpretation of ductility and strength of BMGs. The CSM model gave us new quantitative insights into the atomic-scale mechanisms responsible for the mechanical properties of BMGs. This

model correlates the structure of metallic glasses with their energetics and thus allows one to interpret their deformation in combination with STZs. According to the CSM, the potential-energy barrier to a mechanical instability of a STZ is biased by an applied shear stress and approaches zero as a benchmark of occurrence of yielding. This statistically averaged barrier is dependent on a state variable, i.e., the volumes of STZs, in addition to traditional stress and strain. Following this model, energetic considerations and molecular dynamics simulations more recently conducted have quantitatively evaluated the volume of STZs, which are associated with the configuration entropy and deformability of metallic glasses(Yang, Wadsworth and Nieh 2007, Mayr 2006, Zink et al. 2006). The STZ size is somewhat coincident with the predicted size of MRO of 1-1.5 nm(Sheng et al. 2006, Miracle 2004), Although the significance of this should not be overestimated, this dimensional coincidence may imply a potential intrinsic correlation between STZs and the MRO clusters(Zhang and Greer 2006a). By linking the cooperative shear model with classical deformation thermo dynamics through the variable of the activation volume, the STZ volume is derived as a function of strain rate sensitivity and strength of metallic glasses, which are measurable by mechanical testing(Pan et al. 2008b). The measured STZ volumes of BMGs vary from 2.5 to 6.6 nm^3. According to the dense packing hard-sphere model of metallic glasses, the STZs are estimated to include about 200-700 atoms, consistent with large-scale MD simulations. Moreover, the STZ volumes show an interesting correlation with the ductility of metallic glasses. The ductile BMGs possess large STZ volume (Pan et al. 2008b), which is similar to the relationship between ductility and

dislocation cores in fcc metals, in which ductile metals have wide dislocation cores.

1.4.3 Shear band initiation and propagation

The above theories describe the plastic flow and deformation behavior of metallic glasses. But what is the consequence of the localized distortion of the surrounding material created by STZ? Under an applied stress, accommodation of shear strain in metallic glasses is believed to occur via atom rearrangements around free volume regions, unlike dislocation in crystalline counterpart. The strain-accommodating local rearrangement theory proposed by Argon(Argon 1979a) considers two modes of thermally-activated shear transformation. Delineating the boundary between homogeneous and inhomogeneous plastic flow, Argon(Argon 1979a) proposed that the transformation involves diffuse rearrangements with small shear strain in spherical regions of 5 atom diameters at temperatures of $0.6T_g < T < T_g$. Below $0.6T_g$ the transformation occurs in a narrow disk-shaped volume element called the “shear transformation zone”, in a manner similar to dislocation loop formation.

The fundamental unit of plasticity during inhomogeneous deformation of metallic glasses can be the shear transformation zone or the free-volume for local diffusive jumps. The STZ is a small cluster of closely-packed atoms that spontaneously and cooperatively rearrange to accommodate the applied shear strain.(Lund and Schuh 2004,

Spaepen 1977a, Argon 1979a) The STZ involves a localized cluster of atoms that undergo intense distortion from an initial to final equilibrium position through an intermediate activated state of high-energy and large-volume. The continued propagation of this applied shear strain occurs when one STZ creates a localized distortion of the surrounding material, which triggers the formation of large planar bands of STZs, or so-called “shear bands”. It should be noted that the STZ is not a defect in the glass structure, but rather a transient state whose operation is influenced by local atomic arrangements.

According to the free volume model developed by Turnbull and Spaepen(Turnbull 1961, Spaepen 1977a), plastic flow is triggered by jumps of atoms squeezed into neighboring positions of equal space. When the neighboring atomic site is of a smaller size, the diffusing atom will create free volume by making the jump. This can lead to work softening during plastic deformation due to a macroscopic decrease in viscosity. The generation of free volume during the shearing of small groups of atoms (Li et al. 2003, Donovan 1989, Liu et al. 2005) is assumed to be the reason for the formation of localized shear band, which causes a decrease in the viscosity of the glass. The formation of free volume weakens the specimen locally by decreasing the cross-sectional area, and subsequently induces local softening of the material until fracture occurs along the plane of the shear bands(Spaepen 1977a). Another explanation for the formation of shear bands is that local adiabatic heating makes the temperature exceed the glass transition temperature, thus decreasing the viscosity locally (Liu et al. 1998,

Leamy, Chen and Wang 1972, Chen et al. 1994). A vein-like pattern characteristically forms on the fracture surface of metallic glass. This pattern is the consequence of adiabatic heating in the shear band which causes softening of the BMGs(Pampillo and Reimschu.Ac 1974). The vein-like pattern shows that the material within a shear band behaves like a liquid layer of reduced viscosity due to local dilatation of the glass in regions of high tensile stress. It is likely that STZs lead to free volume creation and thermal softening jointly promotes the formation of shear bands in BMGs (Dai and Bai 2008, Li and Li 2006). Dai and Bai(Dai and Bai 2008) have shown that (1) instabilities governed by free volume creation become unstable leading to shear band formation if the compound volume creation rate exceeds the free volume diffusion rate; (2) instabilities governed by thermal softening become unstable provided $B > KP_0\tau_0/\rho C_v Q_0$, where B is a dimensionless number reflecting the competition between thermal softening, P_0, and strain hardening, τ_0 is shear stress, Q_0, K is the Taylor-Quinney coefficient (~0.9), ρ is density, and C_v is specific heat at constant volume; and (3) deformation with coupled thermal effects and free volume creation is jointly initiated, which accelerates the instability growth, but the compound free volume creation appears to govern the instability growth when B~1. Jiang and Dai(Jiang and Dai 2009) have shown that shear-banding instability is free volume by origin. They explain that totally different mechanisms are responsible for shear-banding instability due to free-volume softening and classical thermal softening. Shear-banding instability begins with strains responding elastically to applied stress until the yield point is reached, at which inelastic/plastic flow is activated in a locally free-volume perturbed region. A mismatch

in strain rate between the perturbed (shear band) and unperturbed (matrix) zone occurs and continues to become exacerbated, leading to a large strain in the perturbed zone and then shear band appears. Jiang and Dai (Jiang and Dai 2009) further explained that the dynamic plastic strain rate in the shear-band region causes instantaneous local temperature increase, which speeds up the net creation of free volume and facilitates shear-banding instability originated from local free-volume perturbation.

1.5 Research objectives and issues

Since the Bronze Age, the search for strong-and-ductile metals has been one of the central themes in all kinds of tool-making activities. After centuries of dedicated efforts, plasticity in crystalline metals has now been well understood; however, it still remains unclear in many fundamental aspects for amorphous metals, i.e. metallic-glasses. Since the first reported by Klement (W. Klement 1960) in 1960, bulk metallic glasses (BMGs) have attracted extensive interest because of their exclusive properties such as very high strength, hardness, elastic limit as well as good corrosion resistance(Byrne and Eldrup 2008, Cheng and Johnson 1987, Spaepen 1987, Dyre 2008, Greer 1993, Loffler 2003). However, their main drawback is their catastrophic brittle failure under uniaxial loading, initiating from severe plastic-strain localization in a narrow region called the shear band(Schuh, Hufnagel and Ramamurty 2007b). Shear band formation is generally recognized as a direct consequence of yielding or the onset of the plastic deformation. They instantaneously propagate through samples and cause fracture. So the full

understanding of the nature and behavior of the shear bands is of supreme important to the research of metallic glasses.

Several research groups have tried to figure that at what size metallic-glasses could become both strong and ductile without shear-banding. Different reports are inconsistent and controversial with both theoretical and experimental ways. From the theoretical approach, there are different theoretical estimations of the critical length scale. Li(Li and Li 2007) and Shi(Shi 2010) identified the critical length scales for nucleating a shear band is around 10-20 nm. On the other hand, several researchers reported the correlation between the reduced size and the deformation mode transition. However, these experimental results are also inconsistent. Volkert(Volkert, Donohue and Spaepen 2008) et al., who conducted a study on $Pd_{77}Si_{23}$ BMGs, showed that for pillars below ~400 nm plasticity is entirely homogeneous. Guo(Guo et al. 2007b) and Jang(Jang and Greer 2010) report that inhomogeneous to homogeneous deformation mode change occurs at 100nm diameter with their tension test. Meanwhile, an interesting finding by Chen(Chen, Pei and De Hosson 2010) is that a switch from highly inhomogeneous to fully homogeneous deformation is observed at an experimentally accessible size regime near 200 nm by micro-bending.

These inconsistencies caused by the test method itself from several aspects. Firstly, most of the experiments fabricated with focused ion beam (FIB). Because of the non-uniform stress distributions along the imperfectly tapered pillar down to submicrometer scale and the stress concentration induced by friction between the flat punch and pillar

top in the micro compression test with diameters. Shear bands may preferentially nucleate at the corner of sample and punch. On the other hand, surfaces strongly influence the strain localization behavior. At the same time, the compressive stress introduced by the surface could delay the nucleation of shear band in the sample at smaller scales.

Based on the reasons above, my research will focus on the critical length controlling homogeneous shear-band nucleation. In chapter 3, through a series of carefully designed spherical indentation tests, we are able to extract the shear-band nucleation lengths for a Zr-based MG at different indentation strain rates. In chapter 4, residual stresses were introduced in the sample through plastic bending. The effect of residual stress on the shear band nucleation was discussed. In chapter 5, as-cast sample and annealed sample with different temperature were studied. The effect of thermal history on the shear band nucleation was compared and discussed. In chapter 6, based on different types of MG, the relationship between the intrinsic physical properties and critical length controlling homogeneous shear-band nucleation was systematically studied. Finally in Chapter 7, the results of this thesis are summarized and the perspectives for future research are suggested.

1.6 Reference

Argon, A. S. (1979) Plastic-Deformation in Metallic Glasses. Acta Metallurgica, 27, 47-58.

Bernal, J. D. (1960) The structure of liquids. Scientific American, 203, 124.

Byrne, C. J. & M. Eldrup (2008) Materials science - Bulk metallic glasses. Science, 321, 502-503.

Chen, C. Q., Y. T. Pei & J. T. M. De Hosson (2010) Effects of size on the mechanical response of metallic glasses investigated through in situ TEM bending and compression experiments. Acta Materialia, 58, 189-200.

Chen, H., Y. He, G. J. Shiflet & S. J. Poon (1994) Deformation-Induced Nanocrystal Formation in Shear Bands of Amorphous-Alloys. Nature, 367, 541-543.

Chen, H. S. (1974) Thermodynamic Considerations on Formation and Stability of Metallic Glasses. Acta Metallurgica, 22, 1505-1511.

Chen, H. S. (1980) Glassy Metals. Reports on Progress in Physics, 43, 353-&.

Cheng, Y. T. & W. L. Johnson (1987) Disordered Materials - a Survey of Amorphous Solids. Science, 235, 997-1002.

Cohen, M. H. (1980) Citation Classic - Molecular-Transport in Liquids and Glasses. Current Contents/Physical Chemical & Earth Sciences, 10-10.

Conner, R. D., R. B. Dandliker & W. L. Johnson (1998) Mechanical properties of tungsten and steel fiber reinforced Zr41.25Ti13.75Cu12.5Ni10Be22.5 metallic glass matrix composites. Acta Materialia, 46, 6089-6102.

Dai, L. H. & Y. L. Bai (2008) Basic mechanical behaviors and mechanics of shear banding in BMGs. International Journal of Impact Engineering, 35, 704-716.

Donovan, P. E. (1989) A Yield Criterion for Pd40ni40p20 Metallic-Glass. Acta Metallurgica, 37, 445-456.

Dyre, J. (2008) Mysteries of the glass transition. Physics Today, 61, 15-15.

Fan, C., P. K. Liaw & C. T. Liu (2009) Atomistic model of amorphous materials. Intermetallics, 17, 86-87.

Finney, J. L. (1970) Random Packings and Structure of Simple Liquids .1. Geometry of Random Close Packing. Proceedings of the Royal Society of London Series a-Mathematical and Physical Sciences, 319, 479-&.

Greer, A. L. (1993) Materials Science - Confusion by Design. Nature, 366, 303-304.

Greer, J. R. & J. T. M. De Hosson (2011) Plasticity in small-sized metallic systems: Intrinsic versus extrinsic size effect. Progress in Materials Science, 56, 654-724.

Guo, H., P. F. Yan, Y. B. Wang, J. Tan, Z. F. Zhang, M. L.Sui & E. Ma (2007a) Tensile ductility and necking of metallic glass. Nature Mater., 6, 735-739.

Guo, H., P. F. Yan, Y. B. Wang, J. Tan, Z. F. Zhang, M. L. Sui & E. Ma (2007b) Tensile ductility and necking of metallic glass. Nature Materials, 6, 735-739.

Inoue, A. & A. Takeuchi (2002) Recent progress in bulk glassy alloys. Materials Transactions, 43, 1892-1906.

Jang, D. C. & J. R. Greer (2010) Transition from a strong-yet-brittle to a stronger-and-ductile state by size reduction of metallic glasses. Nature Materials, 9, 215-219.

Jiang, M. Q. & L. H. Dai (2009) On the origin of shear banding instability in metallic

glasses. Journal of the Mechanics and Physics of Solids, 57, 1267-1292.

Johnson, W. L. (1999) Bulk glass-forming metallic alloys: Science and technology. Mrs Bulletin, 24, 42-56.

Johnson, W. L. (2002) Bulk amorphous metal - An emerging engineering material. Jom-Journal of the Minerals Metals & Materials Society, 54, 40-43.

Johnson, W. L. & K. Samwer (2005) A universal criterion for plastic yielding of metallic glasses with a (T/T-g)(2/3) temperature dependence. Physical Review Letters, 95.

Leamy, H. J., H. S. Chen & T. T. Wang (1972) Plastic-Flow and Fracture of Metallic Glass. Metallurgical Transactions, 3, 699-&.

Li, J. X., G. B. Shan, K. W. Gao, L. J. Qiao & W. Y. Chu (2003) In situ SEM study of formation and growth of shear bands and microcracks in bulk metallic glasses. Materials Science and Engineering a-Structural Materials Properties Microstructure and Processing, 354, 337-343.

Li, Q. K. & M. Li (2006) Atomic scale characterization of shear bands in an amorphous metal. Applied Physics Letters, 88.

Li, Q. K. & M. Li (2007) Assessing the critical sizes for shear band formation in metallic glasses from molecular dynamics simulation. Applied Physics Letters, 91.

Liu, C. T., L. Heatherly, D. S. Easton, C. A. Carmichael, J. H. Schneibel, C. H. Chen, J. L. Wright, M. H. Yoo, J. A. Horton & A. Inoue (1998) Test environments and mechanical properties of Zr-base bulk amorphous alloys. Metallurgical and Materials Transactions a-Physical Metallurgy and Materials Science, 29, 1811-1820.

Liu, L. F., L. H. Dai, Y. Bai, B. C. Wei & J. Eckert (2005) Behavior of multiple shear bands in Zr-based bulk metallic glass. Materials Chemistry and Physics, 93, 174-177.

Loffler, J. F. (2003) Bulk metallic glasses (vol 11, pg 529, 2003). Intermetallics, 11, 979-979.

Lund, A. C. & C. A. Schuh (2004) The Mohr-Coulomb criterion from unit shear processes in metallic glass. Intermetallics, 12, 1159-1165.

Mayr, S. G. (2006) Activation energy of shear transformation zones: A key for understanding rheology of glasses and liquids. Physical Review Letters, 97.

Miracle, D. B. (2004) A structural model for metallic glasses. Nature Materials, 3, 697-702.

Miracle, D. B. & O. N. Senkov (2003a) A geometric model for atomic configurations in amorphous Al alloys. Journal of Non-Crystalline Solids, 319, 174-191.

Miracle, D. B. & O. N. Senkov (2003b) Topological criterion for metallic glass formation. Materials Science and Engineering a-Structural Materials Properties Microstructure and Processing, 347, 50-58.

Pampillo, C. A. (1975) Flow and fracture in amorphous alloys. Journal of Materials Science, 10, 1194-1227.

Pampillo, C. A. & Reimschu.Ac (1974) Fracture Topography of Metallic Glasses. Journal of Materials Science, 9, 718-724.

Pan, D., A. Inoue, T. Sakurai & M. W. Chen (2008) Experimental characterization of shear transformation zones for plastic flow of bulk metallic glasses. Proceedings of the National Academy of Sciences of the United States of America, 105,

14769-14772.

Schuh, C. A., T. C. Hufnagel & U. Ramamurty (2007) Mechanical behavior of amorphous alloys. Acta Mater., 55, 4067-4109.

Sheng, H. W., Y. Q. Cheng, P. L. Lee, S. D. Shastri & E. Ma (2008) Atomic packing in multicomponent aluminum-based metallic glasses. Acta Materialia, 56, 6264-6272.

Sheng, H. W., W. K. Luo, F. M. Alamgir, J. M. Bai & E. Ma (2006) Atomic packing and short-to-medium-range order in metallic glasses. Nature, 439, 419-425.

Shi, Y. F. (2010) Size-independent shear band formation in amorphous nanowires made from simulated casting. Applied Physics Letters, 96.

Spaepen, F. (1977) Microscopic Mechanism for Steady-State Inhomogeneous Flow in Metallic Glasses. Acta Metallurgica, 25, 407-415.

Spaepen, F. (1987) The Art and Science of Microstructural Control. Science, 235, 1010-1014.

Steif, P. S., F. Spaepen & J. W. Hutchinson (1982) Strain Localization in Amorphous Metals. Acta Metallurgica, 30, 447-455.

Turnbull, D. a. M. H. C. (1961) Free-Volume Model of Amorphous Phase - Glass Transition

Transition. Journal of Chemical Physics, 34, 120.

Volkert, C. A., A. Donohue & F. Spaepen (2008) Effect of sample size on deformation in amorphous metals. Journal of Applied Physics, 103.

W. Klement, R. H. W., P.O.L. Duwez (1960). Nature, 187, 869-870.

Willens, P. D. a. R. H. (1963) Rapid Quenching of Liquid Alloys. Transactions of the Metallurgical Society of Aime, 227, 362.

Wu, F. F., Z. F. Zhang & S. X. Mao (2009a) Size-dependent shear fracture and global tensile plasticity of metallic glasses. Acta Materialia, 57, 257-266.

Wu, F. F., Z. F. Zhang & S. X. Mao (2009) Size-dependent shear fracture and global tensile plasticity of metallic glasses. Acta Materialia 57, 257-266.

Wu, Y., H. X. Li, G. L. Chen, X. D. Hui, B. Y. Wang & Z. P. Lu (2009) Nonlinear tensile deformation behavior of small-sized metallic glasses. Scripta Materialia, 61, 564-567.

Yang, B., M. L. Morrison, P. K. Liaw, R. A. Buchanan, G. Y. Wang, C. T. Liu & M. Denda (2005) Dynamic evolution of nanoscale shear bands in a bulk-metallic glass. Applied Physics Letters, 86.

Yang, B., J. Wadsworth & T. G. Nieh (2007) Thermal activation in Au-based bulk metallic glass characterized by high-temperature nanoindentation. Applied Physics Letters, 90.

Ye, J. C., J. Lu, C. T. Liu, Q. Wang & Y. Yang (2010) Atomistic free-volume zones and inelastic deformation of metallic glasses. Nature Materials, 9, 619-623.

Zberg, B., E. R. Arata, P. J. Uggowitzer & J. F. Loffler (2009) Tensile properties of glassy MgZnCa wires and reliability analysis using Weibull statistics. Acta Materialia, 57, 3223-3231.

Zhang, Y. & A. L. Greer (2006) Thickness of shear bands in metallic glasses. Applied Physics Letters, 89.

Zink, M., K. Samwer, W. L. Johnson & S. G. Mayr (2006) Plastic deformation of

metallic glasses: Size of shear transformation zones from molecular dynamics simulations. Physical Review B, 73.

2 Research methodology

Nanoindentation has become the standard technique used for nanomechanical characterization of materials. A nanoindentation test is performed by applying and removing a load to a sample in a controlled manner with a geometrically well-defined probe. During the nanoindentation, a force is applied by the transducer and the resulting displacement is observed to produce a traditional force versus displacement curve. Nanoindentation measures the force and displacement of the nanoindentation probe with a unique patented three-plate capacitive transducer design. This transducer design provides an unsurpassed noise floor and ultra-low working force.

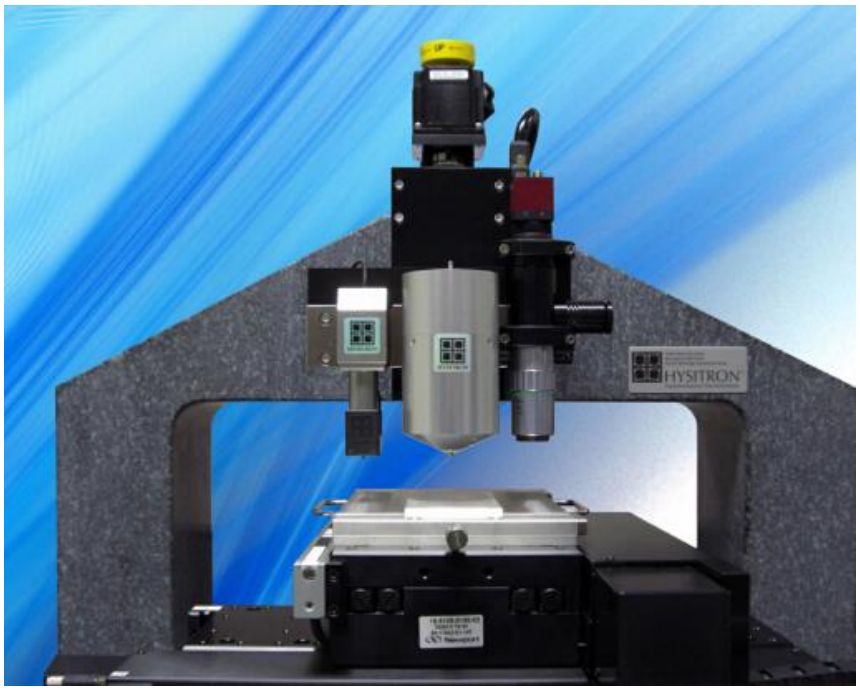

Figure 2.1 TriboIndenter (Hysitron, Inc., Minneapolis, MN)

The tightly controlled construction and calibration standards used for the capacitive transducer in combination with the precisely machined, rigid nanoindentation probes produce quantifiable, reliable measurement on any material. The mechanical properties of the sample obtained from the analysis of the measured force versus displacement curve (particularly the unloading segment). Values typically obtained from nanoindentation testing are reduced modulus and hardness. However other information such as fracture toughness, stiffness, and delamination force and film thickness can also be obtained. With the help of various types of indenter, different mechanical properties can be obtained from the nanoindentation data. We can perform different testing mode with designed indenter on metallic glass: flat-ended indenter for compression tests; wedge-like cylindrical indenter for bending experiments

Nanoindentation from Hysitron is designed for maximum versatility. Standard with all Hysitron nanoindentation systems and equipped with a standard maximum force up to 10 μN and a noise floor of less than 30 nN, quasistatic nanoindentation covers a large range of sample testing possibilities. Other specifications of the transducers in low-load and high-load systems are listed in Table 2.1

Table 2.1 Specifications of Z-axis of the transducer in nanoindentation system

	Low load System	High Load System
Maximum force	10 mN	10N
Load resolution	1 nN	100 nN
Load Noise floor	<30 nN	50 μN
Maximum displacement	5 μm	80 μm
Displacement resolution	0.02 nm	0.1 nm
Displacement noise floor	0.2 nm	1 nm
Thermal drift Data	< 0.05 nm/sec	< 1 nm/sec
Acquisition rate	up to 30 kHz	60 Points/sec

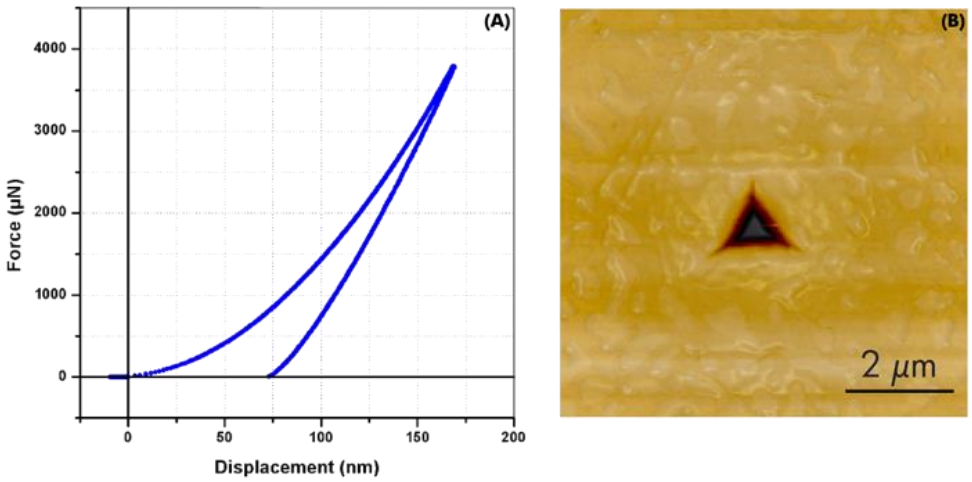

Figure 2.2 (A) Force versus displacement curve on fused quartz showing typical response of elastic-plastic material.(B) Resulting in-situ SPM image of quartz surface after nanoindentation showing residual indent impression.

To study the shear band nucleation behavior in different MGs, nanoindentation tests were performed on small polished disks. Indentation strain control mode was used. The maximum load was varied for different based metallic glass. For a systematic investigation, the following tip radii were used in the spherical indentation tests: 2μm, 5μm, 10μm, 20μm, 25μm, 30μm and 35μm. In order to keep a constant strain rate, $dP/dt/P$ was set to be a constant, where dP/dt is the indentation loading rate and P the indentation load. This leads to an exponential increase of P with the time. For simplicity, unloading was programed to follow a constant unloading rate. At least 10 indents were performed on each sample.

3 Shear Band Nucleation and Indentation Size Effect in Metallic Glass

3.1 Introduction

Hardness is an important material attribute that has long been used to characterize the mechanical strength of materials (Tabor 2000). Physically, hardness of materials is derived not only from an atomic bonding strength but also from microstructural details, such as atomic plane orientation and defect concentration, which is directly probed by an indenter (Cheng and Cheng 2004, Nix and Gao 1998). For crystalline metals, their hardness is material dependent and also varies with an indentation size, viz., as the indentation size decreases, the hardness of crystalline metals usually increases (Nix and Gao 1998, Swadener, George and Pharr 2002, Begley and Hutchinson 1998). This phenomenon is known as the 'indentation size effect' (ISE) and has been investigated extensively over the past decades (Cheng and Cheng 2004, Nix and Gao 1998, Swadener et al. 2002, Begley and Hutchinson 1998).

In principle, the origin of ISE in crystalline metals can be simply explained as the interplay between a material internal length scale L_{int}, such as dislocation size or spacing(Evans and Hutchinson 2009) that can be related to the material local yielding, and an external length scale L_{ext} that can be related to the applied indentation stress field, such as indentation depth or indenter tip radius. From a theoretical viewpoint, ISE arises

when L_{ext} approaches L_{int} and vanishes when $L_{ext} >> L_{int}$. Therefore, it is expected that a material would not exhibit an ISE behavior for its internal length scale being much smaller than the external length scale derived from an indentation stress field.

Metallic glasses (MGs) are one such kind of materials that does not show any internal structural length scales merely above a few nanometers (Chen 2008, Wagner et al. 2011, Ye et al. 2010b, Liu et al. 2011, Zeng et al. 2014, Yang et al. 2012). Being amorphous, MGs are lack of long-range translational symmetry and, hence, there are no crystalline-like defects in them. This view has been invoked often to explain why MGs usually appear much stronger than their crystalline counterparts(Chen 2008, Yang et al. 2010a, Wu, Li and Schuh 2007, Johnson and Samwer 2005b, Ashby and Greer 2006). Therefore, it was once believed that the strength of MGs should be size independent unless the Weibull statistics came into play in small-scale mechanical testing (Lee et al. 2010, Schuster et al. 2008, Packard et al. 2010a, Ye et al. 2010c). In general, a Weibull size effect may appear due to a material inhomogeneity introduced during alloy casting (Lee et al. 2010). According to the prior work (Chen 2008, Wagner et al. 2011, Ye et al. 2010b, Liu et al. 2011, Zeng et al. 2014, Yang et al. 2012), the length scales characterizing the mechanical inhomogeneity in MGs could range from 1 to 10 nm. In such a case, one might expect size-independent hardness if the characteristic size of an indentation stress field applied to a MG goes beyond ~10 nm. However, contrary to this thinking, it was recently reported by different groups that a significant size effect could be observed in different MGs at the submicron scale or

even above (Jang et al. 2011, Choi et al. 2012, Yang et al. 2010a, Lee et al. 2010, Jang and Greer 2010, Tian et al. 2012, Wang et al. 2012). Some of them proposed that this unexpected size effect could be traced back to the activation of the fundamental flow units in MGs, such as shear transformation zones (STZs) (Jang et al. 2011, Choi et al. 2012). However, this proposal needs further clarification because the size of these 'flow units' is very mall (~1-2 nm) (Pan et al. 2008a, Yang et al. 2012) as compared to the external length scales (~100 -1000 nm) over which the ISE behavior was witnessed (Jang et al. 2011, Choi et al. 2012).

Here, we propose an alternative mechanism to quantitatively explain the ISE behavior of MGs. This mechanism is based on the notion that yielding in MGs is caused by the clustering of liquid-like sites or STZs, which subsequently result in shear-band nucleation. In such a case, here comes a length scale, L_{SB}, that is derived from the critical size of shear-band nuclei in MG; therefore, an ISE behavior arises if the applied indentation stress field could possess an external length scale $L_{ext} \sim L_{SB}$. In what follows, we will first develop a theoretical model which directly incorporates L_{SB} into the otherwise size-independent yielding criterion for MGs, such as the well-established Drucker-Prager yielding criterion (Sun, Jiang and Dai 2010). This is followed by a series of indentation experiments particularly designed for justifying our modeling and the ISE behavior in a Zr-based MG. Afterwards, we will show that, through the indentation size effect, L_{SB} can be extracted for different indentation strain rates. Finally, we will discuss the origin of shear-band nucleation based on our combined

theoretical/experimental work.

3.2 Theories and Modeling

3.2.1 The Proposed Mechanism of Size Controlled Yielding

Let us begin our theoretical analysis by assuming that the overall yielding strength of MGs is directly related to a critical shear-band nucleation length L_{SB}. Before reaching this critical length, a stressed MG may also undergo rather localized structural rearrangements which are manifested to be the typical local shear transformation (ST) events (Argon 1979b, Huo et al. 2013, Ye et al. 2010b, Liu, Yang and Liu 2013); however, the longstanding notion is that, only after these local liquid-like sites undergoing ST events coalesce into a critical size, does their surrounding elastic 'cage' break down, thereby leading to overall yielding and inhomogeneous plastic flow in MGs (Schuh, Hufnagel and Ramamurty 2007a, Yang and Liu 2012, Shimizu, Ogata and Li 2006, Greer, Cheng and Ma 2013). Should this scenario of size-controlled yielding hold, one may use a spherical indentation approach to probe the process of shear band nucleation in MGs, as described below.

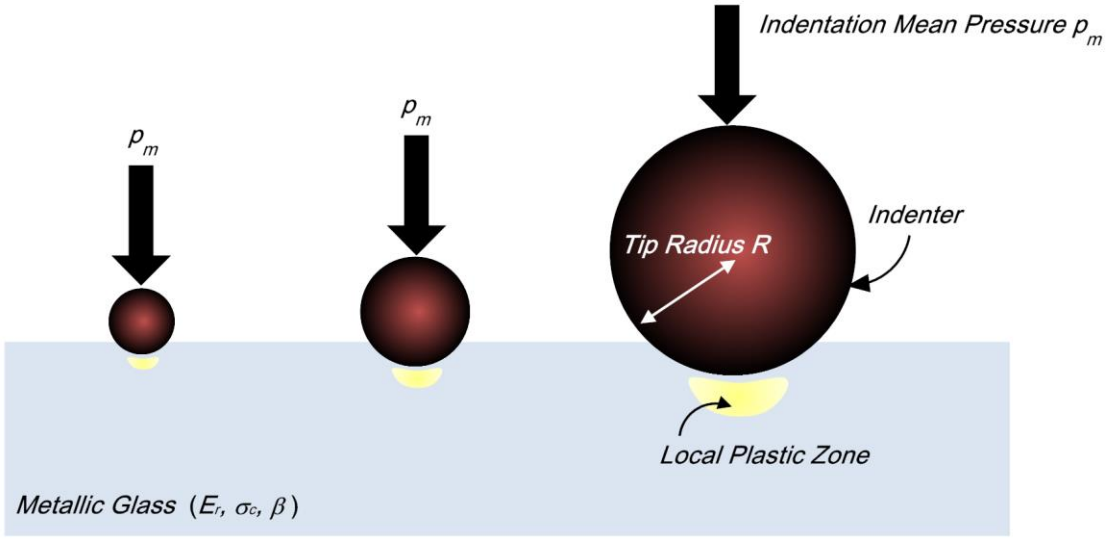

Figure 3.1 The schematic illustration of the tip radius effect on the size of the local plastic zone formed underneath the spherical indenter.

As illustrated in Fig. 3.1, in a spherical indentation test, the maximum shear stress occurs at a distance below the tip-surface contact due to the finite tip radius of the spherical indenter. Owing to the stress gradient of the indentation stress field, it could be envisaged that the localized ST events produce a local plastic zone (LPZ), the size of which expands outwards with the indentation load. Before this local plastic zone extends to the surface, it is engulfed by an elastic 'cage'. Therefore, if unloading occurs, the loading/unloading curves would overlap giving rise to an apparent elastic deformation behavior (Huo et al. 2013, Yang et al. 2010b, Ye et al. 2010b, Packard, Witmer and Schuh 2008). Overall yielding then takes place once the size of the local plastic zone, D_{LPZ}, reaches the critical length, L_{SB}, which triggers the break-down of the elastic matrix and thus results in shear instability. In a simple word, local yielding in MGs is stress controlled according to the classic micromechanical models (Schuh, Lund

and Nieh 2004, Argon 1979b, Spaepen 1977b), while overall yielding is herein treated to be size controlled.

From the dimensional consideration, D_{LPZ} scales with the tip radius, R, of the spherical indenter for a given indentation mean pressure p_m. In that regard, a size effect arises if different sized indenters are used to deform the same MG. For large sized indenters, the overall and local yielding points tend to overlap with each other because D_{LPZ} could be already sufficient to cause shear instability at the moment of local yielding. In this size regime, the strength or hardness of MGs can be effectively attributed to the activation of local plasticity events, as in the classic models such as free-volume (Spaepen 1977b) and shear transformation zone model (Argon 1979b), and the recent models based on structural heterogeneity (Liu et al. 2013, Huo et al. 2013). However, for small-sized indenters, overall yielding could be much delayed if $D_{LPZ} < L_{SB}$ at the onset of local yielding. For the latter case, subcritical growth of the local plastic zone is needed to trigger shear instability. As a result, the hardness may appear greater as the indenter tip radius becomes smaller.

3.2.2 Dimensional Analysis and Theoretical Modeling

In line with the above thinking, the critical load, P_c, leading to the overall yielding in MGs under spherical indentation can be expressed as:

$$P_c = f\left(L_{SB}, R, E_r, \sigma_c, \beta\right) \tag{3.1}$$

where f is a continuous function; E_r is the reduced modulus; σ_c is the classic and scale-independent yield strength as commonly defined in the literature (Johnson and Samwer 2005b, Schuster et al. 2008, Sun et al. 2010) and β is the dimensionless pressure sensitivity that defines the pressure dependency of yielding in MGs (Sun et al. 2010). Note that σ_c and β are two phenomenological parameters that are inherently rate and temperature dependent. Their functional forms could be derived according to the classic yielding models, such as the cooperative shear model (CSM), as demonstrated in Ref.(Johnson and Samwer 2005b).

Following the Buckingham theorem (Barenblatt 2009), Eq. (3.1) can be simplified to the dimensionless form:

$$\frac{p_c}{E_r} = \Pi\left(\frac{L_{SB}}{R}, \frac{\sigma_c}{E_r}, \beta\right) \tag{3.2}$$

where Π is a dimensionless function whose form is yet to be determined, and p_c is the indentation mean pressure or hardness corresponding to P_c. By assuming that the local yielding process follows the modified CSM criterion (Johnson and Samwer 2005b) or the Drucker-Prager yielding criterion, as derived by Sun et al. (Sun et al. 2010), the functional form of Π could be fitted out for typical Zr-based MGs using the finite element (FE) simulations. The details are described in **Appendix A** and omitted here

for brevity. With the extensive FE simulations, we finally obtain the following functional form for Eq. (3.2):

$$p_c = p_0 + C_0 E_r \left(\frac{L_{SB}}{R} \right)^{C_1} \tag{3.3}$$

where p_0 is the scale-free hardness or the mean pressure at the overall yielding point; C_0 and C_1 are two terms derived from the simulation results. Note that these three terms are all functions of σ_c, E_r and β, however, once the power law function as in (3) was adopted, the values of C_0 and C_1 were found to be insensitive to the choice of the independent variables (σ_c, E_r, β). According to our simulations, $C_0 = 0.5$ and $C_1 = 1.45$; therefore, Eq. (3) can be also written as $p_c = p_0 + 0.5E_r \left(L_{SB} / R \right)^{1.45}$. Evidently, $p_c \sim p_0$ for $R >> L_{SB}$ while p_c increases with the decreasing R when $R \sim L_{SB}$.

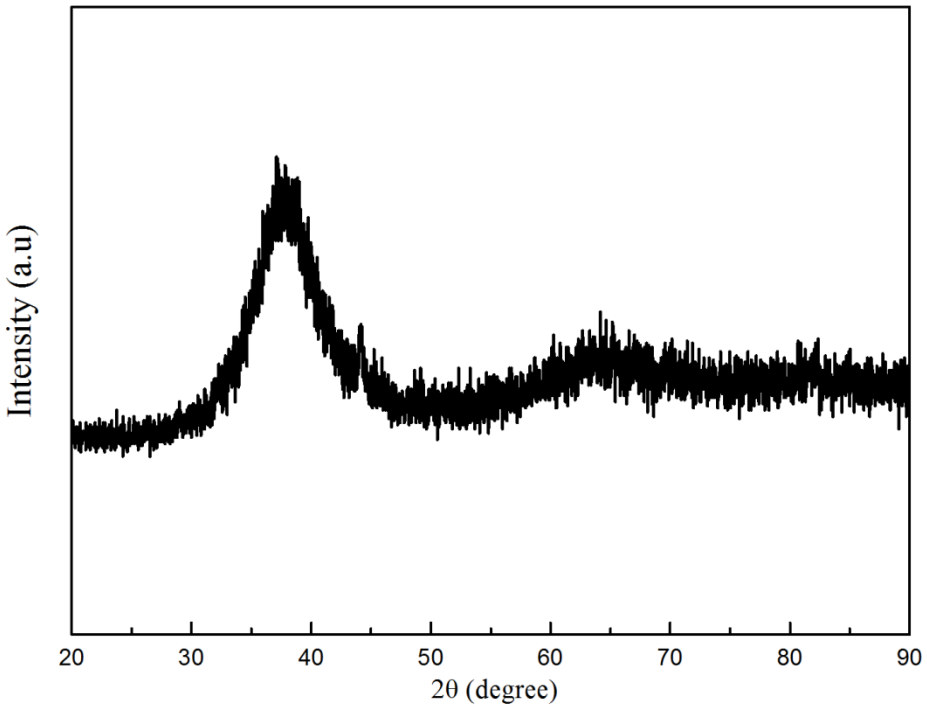

Figure 3.2 X-ray diffraction pattern of the bulk metallic glass $Zr_{52.5}Cu_{17.9}Ni_{14.6}Al_{10}Ti_5$

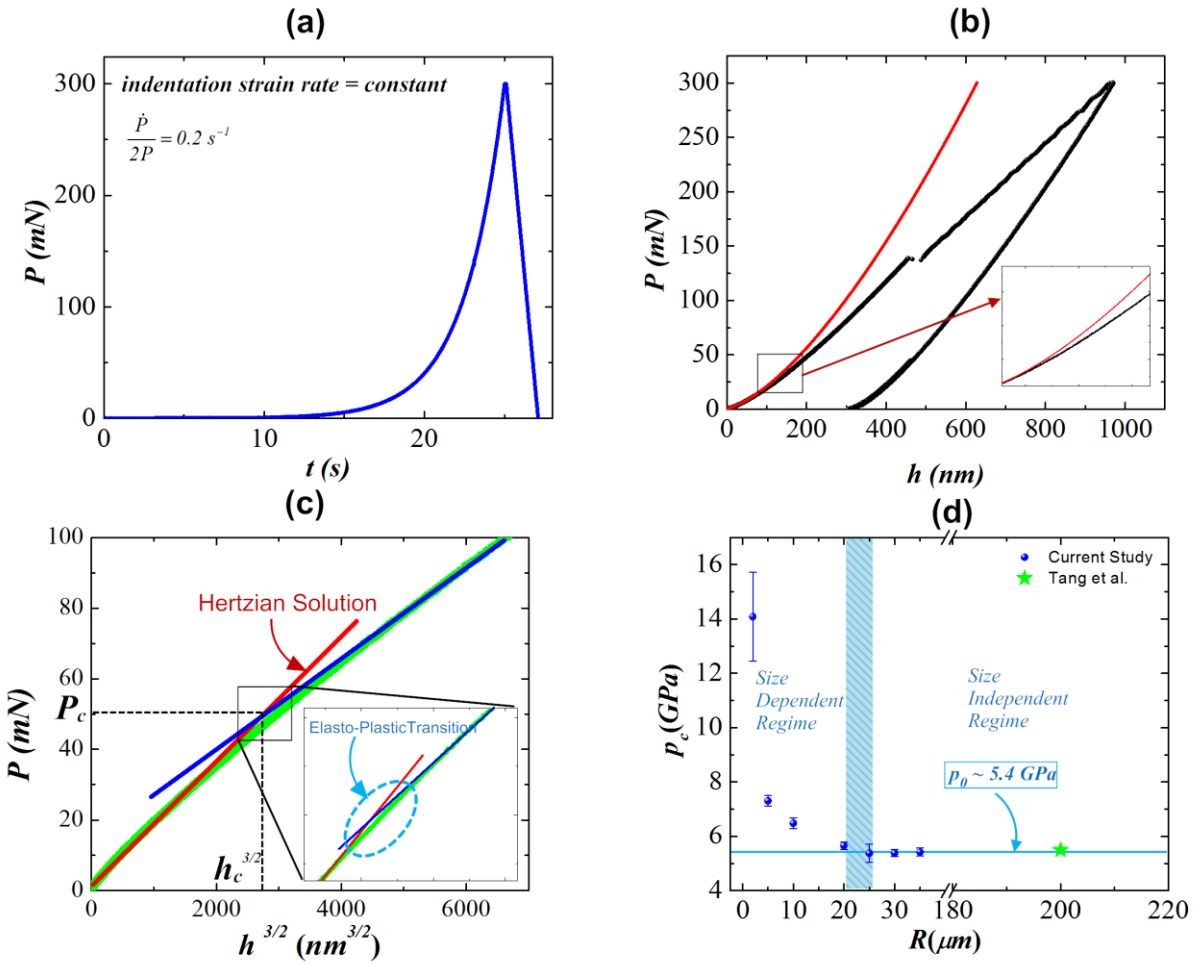

Figure 3.3 (a) The programmed indentation load function for a constant strain-rate indentation test, (b) the typical indentation *P*-*h* curve (the black curve) in comparison with the Hertzian theory (the red curve) (inset = the enlarged view of the departure of the *P*-*h* curve from the Hertzian curve), (c) the typical P-$h^{3/2}$ curve used to measure the critical indentation load P_c (inset = the enlarged view of the elasto-plastic transition manifested by the switch from the Herztian to the non-Hertzian deformation regime), and (d) the hardness data measured as a function of the indenter tip radius at the given indentation strain rate= 0.2 s^{-1} confirming the ISE behavior of the Zr-based MG. Note that the data point corresponding to R = 200 μm is taken from Ref.(Tang, Li and Zeng 2004).

3.3 Experiments

To verify the above theory, we chose a Zr-based MG as the model material, which has the chemical composition of $Zr_{52.5}Cu_{17.9}Ni_{14.6}Al_{10}Ti_5$ (Vit105) (in atomic %). Before the indentation experiment, the amorphous structure of this MG was confirmed by X-ray diffraction (as shown in Figure3.2) and the sample surface was mechanically polished to a mirror finish. The spherical nanoindentation experiments were subsequently carried out at strain control on the Hysitron™ Nanoindentation System (Hysitron Inc, Minneapolis, MN, USA). For a systematic investigation, the following tip radii were used in the spherical indentation tests: 2μm, 5μm, 10μm, 20μm, 25μm, 30μm and 35μm. Note that the above tip radii of the spherical indenters were obtained after tip shape calibration (please see **Appendix B** for details). In order to keep a constant strain rate, $dP/dt/P$ was set to be a constant, where dP/dt is the indentation loading rate and P the indentation load. This leads to an exponential increase of P with the time, t, in the loading segment, as shown in Fig. 3.3(a). For simplicity, unloading was programed to follow a constant unloading rate. In our experiments, three indentation strains were used, i.e. $\dot{\varepsilon} = \frac{1}{2P}\frac{dP}{dt}$ = 0.2 s^{-1}, 2 s^{-1} and 20 s^{-1}.

3.4 Results and Discussions

3.4.1 Indentation Load-Displacement Curve

Figure 3.3(b) shows a typical load-displacement (*P-h*) curve obtained from the as-cast sample for $\dot{\varepsilon}$ = 0.2s^{-1} and R = 20μm. According to the Hertzian theory, $P = (4E_rR^{1/2}/3)h^{3/2}$ for elastic indentation. Therefore, we can extract E_r by fitting the initial linear portion of the P-$h^{3/2}$ curve, as shown in Fig. 3.3(c), to the Hertzian curve. In principle, one may define the overall yielding point at the departure of the *P-h* curve from the Hertzian theory. However, directly matching the *P-h* curve with the Hertzian theory could lead to ambiguity in locating the overall yielding point. As shown by the inset of Fig. 3.3(b), the apparent departure point may look shifting towards a low value if the plots are magnified. To avoid this ambiguity, we fit the high-load portion of the P-$h^{3/2}$ curve starting from the same indentation load and then back extrapolate it to intercept the Hertzian fit. The interception defines the turning point which signifies the elasto-plastic transition on the P-$h^{3/2}$ curve. The critical yielding load P_c is then defined at the turning point, as shown in Fig. 3.3(c). In this way, all critical yielding load P_c can be obtained irrespective of how detailed the departure point would be inspected. In this study, we trying to addressing the gradually transition of deformation behavior which is from elastic regime to a regime dominated by multiple shear banding. The load-displacement curve for different indenter sizes are shown on Fig. 3.4 and we can found that the departure from the Hertzian prediction to the distributed plasticity by multiple shear bands is well below the pop-in event. In previous studies(Liu et al. 2009, Packard

et al. 2010b), before the emergence of first pop-in (or displacement burst/load drop), the load- displace curve already shows the gradually departure from elastic region from compression and micro compression test. Also in simulated nanoindentation(Packard et al. 2010b), they found that the load-displacement curve initially follows the elastic curve exactly, but at a certain depth begins to noticeably depart from the elastic curve as plastic flow sets in while no pop-in events examined in the curve. So the scenario may as follows: Physically, yielding in a MG is initiated via a local ‘de-caging’ process, this can be interpreted as the breakdown of the local elastic confinement that encapsulate the individual ‘flow unit’. At a critical load, the local ‘de-caging’ effect spreads out with the flow units percolating though the elastic matrix, causing the deviation of P-h curve from the Hertzian solution by multiple shear banding. In such a case, the pop-in event is only an after-effect of this percolation process. The pop-in event and the onset of departure from Hertzian solution indeed correspond to different stages of the structural evolution process in a MG. In Cheng’s work (Cheng and Ma 2011b) , he also mentioned that the local high stress does not necessarily lead to shear banding, the activated STZ, while local stress close to intrinsic strength, may not form a shear band if no viable plan is ready, but may still cause a pop-in in nanoindentation.

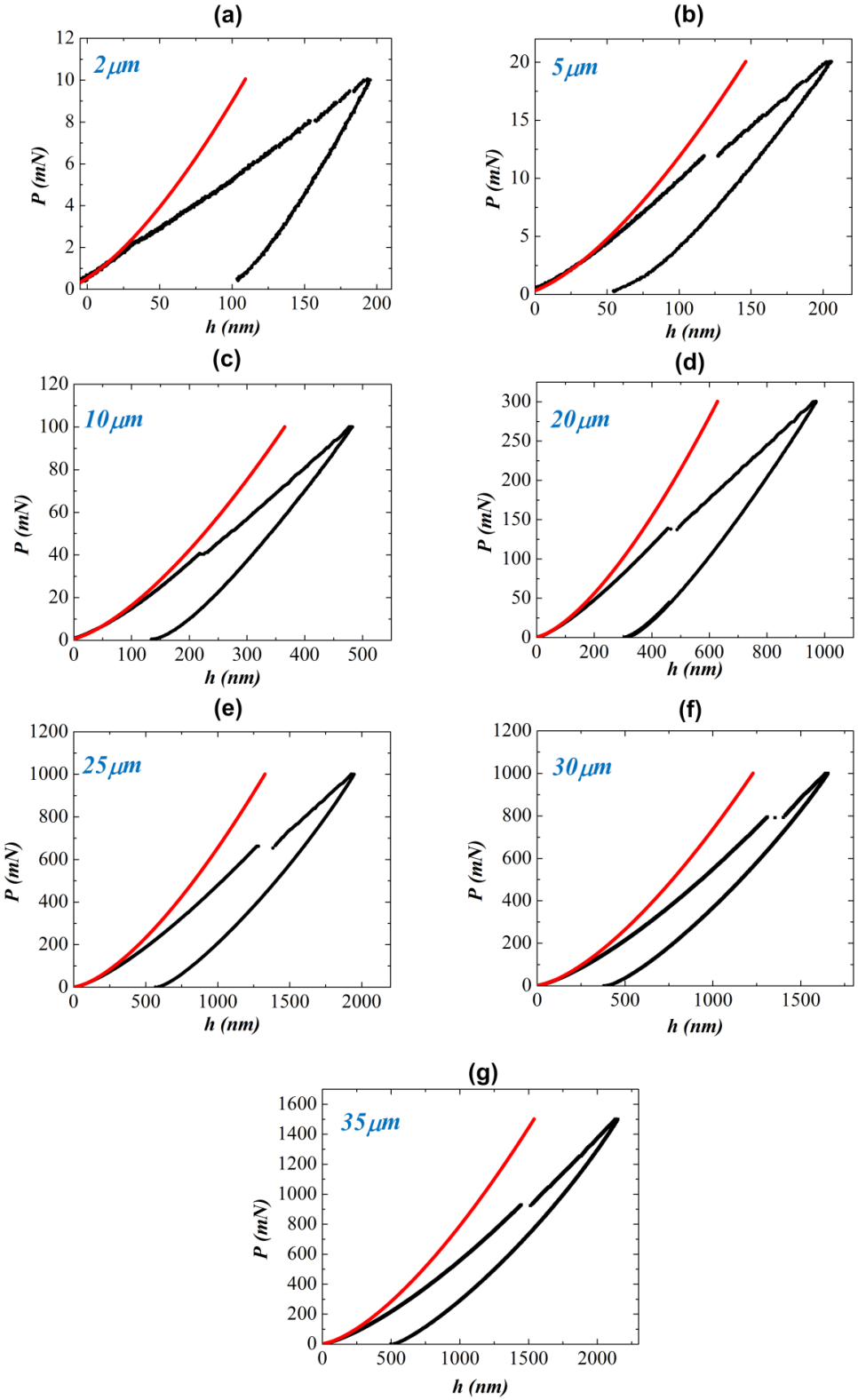

Figure 3.4 The typical indentation P-h curve (the black curve) in comparison with the Hertzian theory (the red curve) for different indenter size

3.4.2 Indentation Size Effect and Shear-Band Nucleation Length

Following the above methods, the reduced modulus E_r of the Zr-based MG was extracted, which shows an average value of 100 GPa, independent of the tip radius and consistent with the measurement via the classic Berkovich nanoindentation. On the other hand, the critical mean pressure, p_c, or hardness can be obtained at the critical load P_c via the equation $p_c = \left(\frac{6P_c E_r^2}{\pi^3 R^2} \right)^{\frac{1}{3}}$. Note that at least 10 indentation tests were carried out at the random sites on the MG surface for each tip radius. This ensures the repeatability of our experimental data. As shown in Fig. 3.3(d), the measured p_c exhibits a sharp ISE behavior for R < 20 μm, which is similar to what was reported in the previous work (Jang et al. 2011, Choi et al. 2012). However, as R is increased to be greater than 20 μm, p_c remains at a constant value of ~5.4GPa, which is very close to the mean pressure previously measured by Tang et al. using the spherical indenter of R = 200 μm (Tang et al. 2004).

With the data shown in Fig. 3.3(d), our theoretical model can be verified. According to Fig. 3.3(d), p_0 can be taken as 5.4 GPa for Vit105 [Fig. 3.3(d)]. Since Equation (3.3) predicts that p_c-p_0 should scale with 1/R to the power of 1.45, we can now compare the experimental data to this scaling relation. As seen in Fig. 3.5(a), it is evident that the trend of the experimental data is captured very well by the theoretical model. Furthermore, the critical length L_{SB} can be extracted by fitting the experimental

data to the theory. With E_r ~ 100 GPa, we obtain L_{SB} = 536 ± 34 nm for the indentation strain rate of 0.2 s^{-1}. Following the same procedure, we can extract L_{SB} for the other two indentation strain rates. Interestingly, as shown in Fig. 3.5(b), there is a very small but detectable increase in L_{SB} with the indentation strain rates. The resulting rate sensitivity, defined as $m = d\ ln(L_{SB})/d\ ln(\dot{\varepsilon})$, is ~ 0.01.

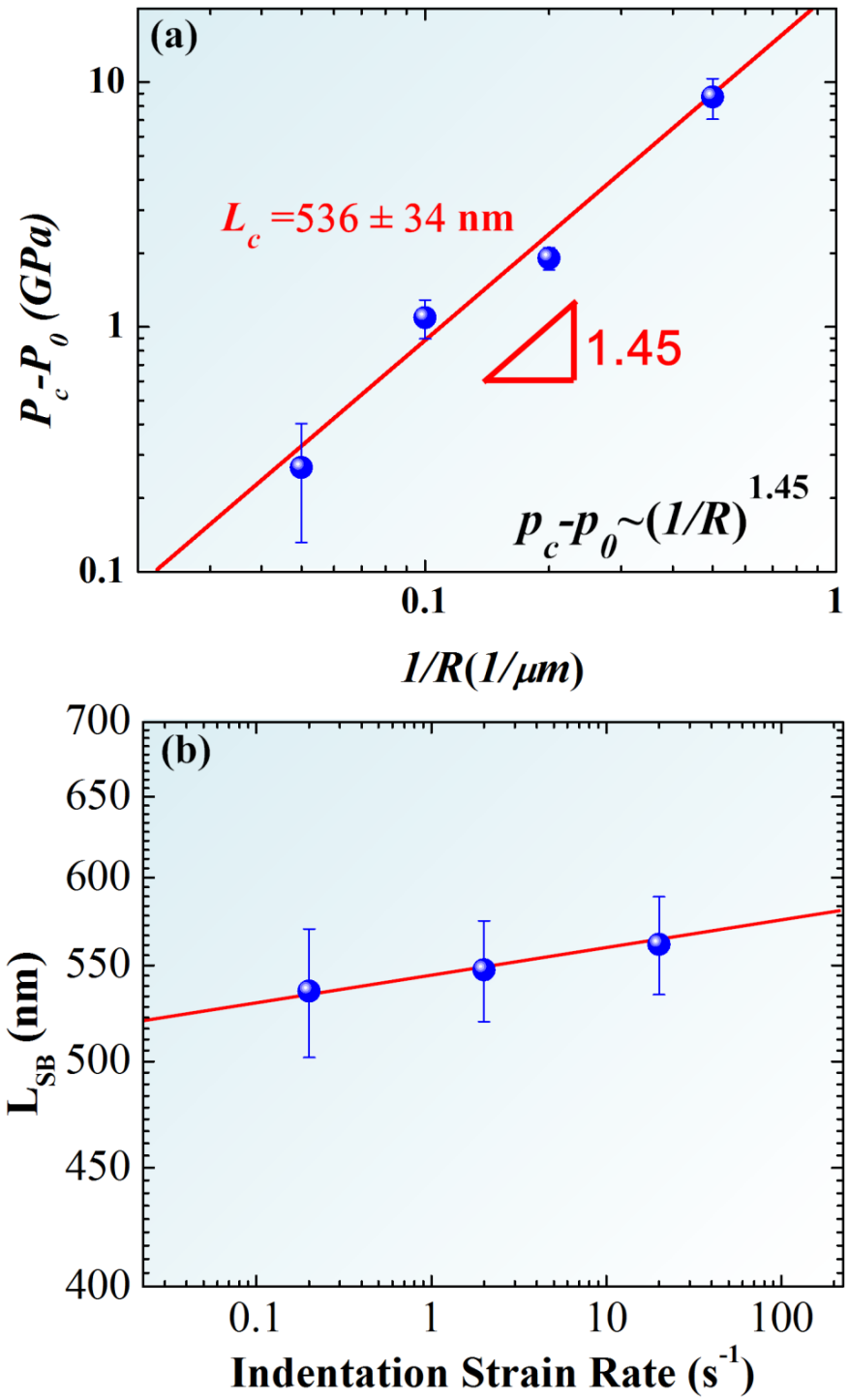

Figure 3.5 (a) The comparison of the experimental data of p_c-p_0 versus 1/R with the theoretical predicted scaling ration, and (b) the variation of the extracted L_{SB} with the indentation strain rates.

Compared to the previous experimental studies (Jang and Greer 2010, Guo et al. 2007b, Chen et al. 2010, Tian et al. 2012, Volkert et al. 2008, Ye et al. 2012, Yavari et al. 2010, Ye et al. 2009b), particularly the nano-scale uniaxial tension, in which the critical shear-band nucleation length was estimated to be ~100 nm for Zr-based MGs, our extracted shear-band nucleation length seems relatively high (~500 nm). The discrepancy could be explained as follows. As pointed out by Shimizu et el. (Shimizu et al. 2006) and Cheng et al. (Cheng and Ma 2011a), shear bands tend to nucleate from surface 'defects' of a MG sample in a uniaxial test. This is analogous to the scenario of heterogeneous nucleation and contrasts the sub-surface shear-band nucleation within a gradient indentation stress field. The latter case is close to the scenario of homogeneous nucleation and therefore, it is reasonable for the ISE-derived shear-band nucleation length to be longer than the prior estimates from uniaxial tests.

To further look into this issue, Fig. 3.6 summarizes the recently obtained shear-band nucleation lengths though different experimental methods, including micro- and nano-compression, micro-bending and nano-tension. As seen in Fig. 3.6, the estimated shear band nucleation length, L_{SB}, appears to be shorter under tension while longer under compression. As suggested by Liu et al. (Liu et al. 2012), Chen et al. (Chen, Pei and De Hosson 2012) and Ye et al. (Ye et al. 2012), external confinements, such as hydrostatic pressure or those encountered during compressive loading, could slow down the STZ dynamics, thereby delaying the process of shear-band nucleation (Ye et

al. 2012). In that regard, the presence of hydrostatic pressure in the indentation stress field may further increase the shear-band nucleation length.

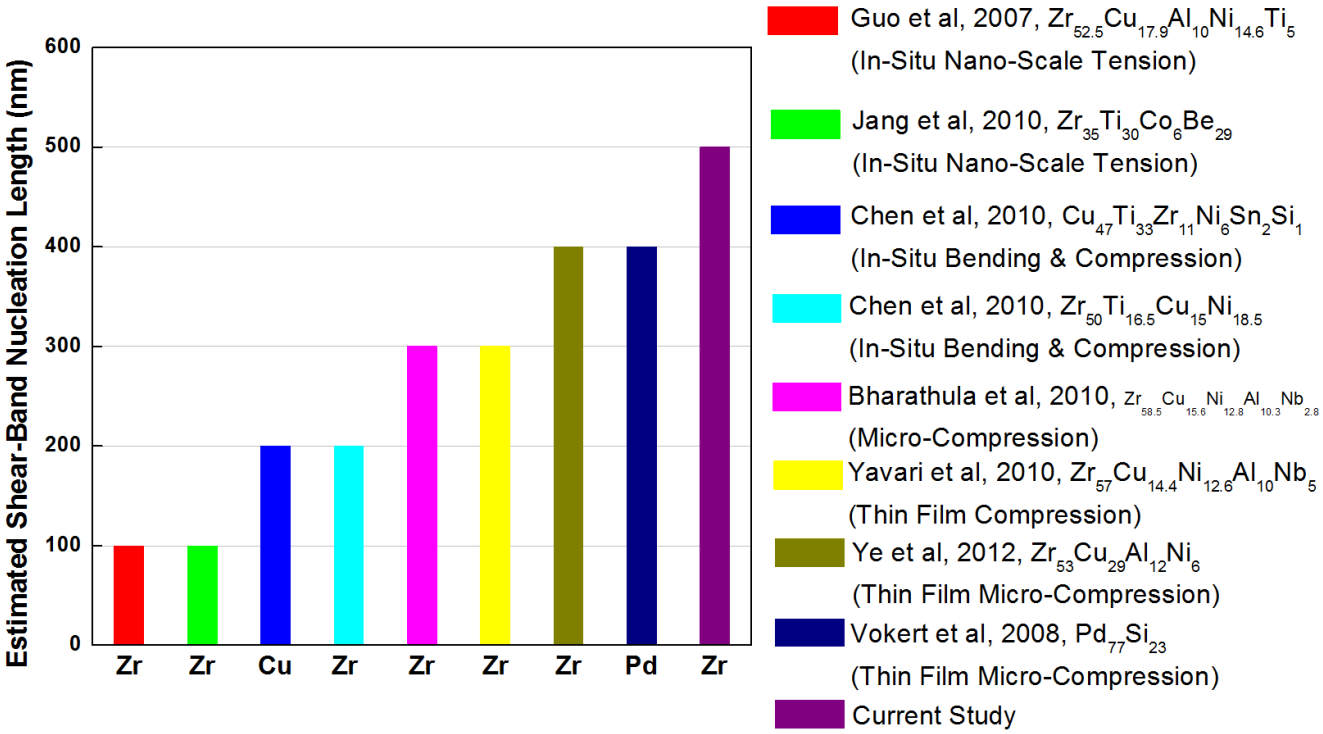

Figure 3.6 Comparison of the shear-band nucleation length obtained from the current study with those estimated previously for the variety of MGs from different experiments. Note that the experimental data are taken from the work of Guo et al (Guo et al. 2007b), Jang et al (Jang and Greer 2010), Chen et al (Chen et al. 2010), Bharathula et al (Bharathula 2010), Yavari et al (Yavari et al. 2010), Ye et al (Ye et al. 2012) and Volkert et al (Volkert et al. 2008).

3.4.3 The Theoretical Estimate of Shear-Band Nucleation Length

In the MG literature, there are few theoretical models available for the prediction of the shear-band nucleation length for MGs. For example, Schuh et al. (Schuh et al. 2004) predicted a shear-band nucleation length on the order of 100 nm by comparing the frequency of a critical shear-band embryo with that of a STZ. In a similar way, Nieh et al. (Nieh and Wadsworth 2008) however estimated a nucleation length of ~10 nm. On the other hand, according to the MD simulations, Shimizu et al. (Shimizu et al. 2006) developed a shear-band nucleation model by assuming that shear instability occurs once the local temperature in the process zone ahead of a shear-band embryo reaches the glass transition temperature (Cheng and Ma 2011a). Their prediction of the shear-band nucleation length ranges from ~10 to ~100 nm depending on the thermo-mechanical properties of the material. Note that the theoretical base of Shimizu's model is the thermo-softening induced shear-band nucleation, which, however, contradicts many experimental studies showing that there is only limited temperature rise during shear-band nucleation and propagation in MGs, particularly for small samples (Greer et al. 2013, Ye et al. 2009a, Nieh et al. 2012, Cheng et al. 2009, Miracle et al. 2011). In general, the previous theoretical predictions of L_{SB} (10-100 nm) agree qualitatively with the experimental findings, as shown in Fig. 3.6. However, further efforts are still needed to explain our experimental data, particularly, the rate dependence of L_{SB} as shown in Fig. 3.5(b). In the following section, we will turn to a general mechanistic model which could be used to rationalize our experimental finding.

3.4.4 The General Shear-Band Nucleation Model

Regardless of the atomic-scale softening mechanism, the process of shear-band nucleation can be described as following. As a shear-band embryo grows in size, mechanical softening occurs to the bonding strength of the atoms which are just being 'absorbed' into its growing front. Mechanistically, the subcritical growth of the shear-band embryo is sustainable only when the local external stress transmitted from the far-field stress can be balanced by its internal resistance. As the local external stress keeps increasing, the residual strength left in the embryo however becomes 'worn' out with further shearing or sliding. When the internal strength becomes incapable of balancing the increasing external stress, the shear-band embryo turns into a runaway defect and, thus, shear instability occurs. In principle, the above-mentioned mechanism of 'shear-softening-induced-instability' applies not only to shear banding in MGs but also to a similar defect nucleation process in many other types of materials, such as earthquake nucleation in the earth's crust.

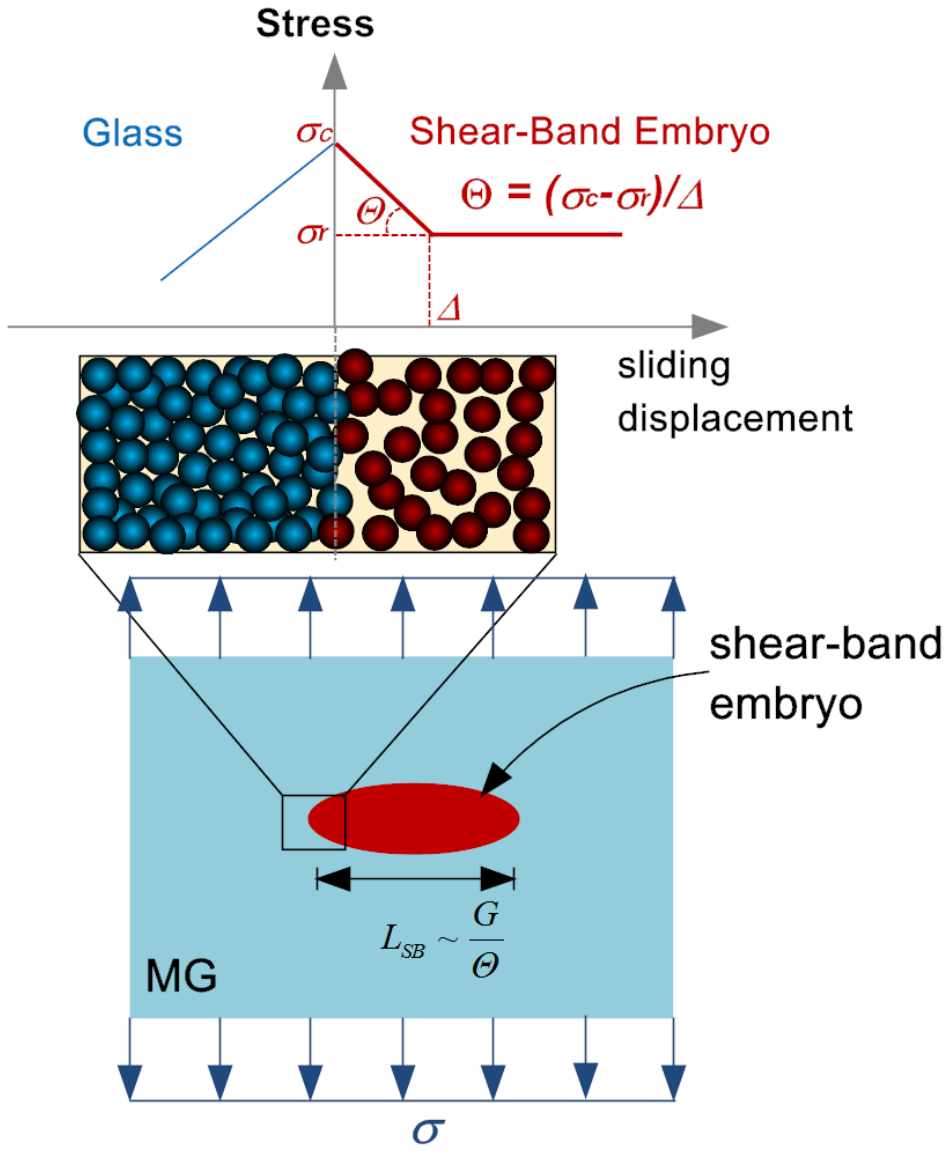

Figure 3.7 The schematic of the subcritical growth behavior of a shear-band embryo in a MG.

Based on the above considerations, Uenishi and Rice(Uenishi and Rice 2003) developed a theoretical model to account for such a process of shear softening induced instability. According to these authors (Uenishi and Rice 2003), the critical length of the shear-band embryo depends mainly on two factors. One is the elastic modulus of the surrounding media that confines the subcritical growth of the embryo, and the other is the softening rate that characterizes the strength loss in the shear-banding embryonic

zone. At the present time, we are not aware of any studies to characterize the softening behavior of shear-band embryos. Therefore, for the sake of simplicity, we simply treat the material softening in the shear-band embryo to be a linear softening process, which is characterized by the local yield stress σ_c and the linear softening rate Θ, as shown in Fig. 3.7. Furthermore, in line with the molecular dynamics (MD) simulation results shown later, we also assume a steady-state residual strength σ_r that remains after the initial softening within the embryonic zone. For the linear softening law as shown in Fig.3.7, the critical shear-band nucleation length can be derived as(Uenishi and Rice 2003):

$$L_{SB} = \alpha \frac{G}{\Theta} \tag{3.5}$$

where α is a dimensionless factor roughly equal to ~1.16 and G is the shear modulus of the MG. Since $\Theta = (\sigma_c - \sigma_r)/\Delta$, where Δ is the critical shear displacement at which the initial softening process is completed, Eq.(3.5) can be re-cast into the following form:

$$L_{SB} = \alpha t_{SB} \frac{G}{(\sigma_c - \sigma_r)/\varepsilon_c} = \alpha t_{SB} \frac{G}{W} \tag{3.6}$$

in which t_{SB} is the shear-band thickness (10-20 nm), ε_c is the critical shear strain (=Δ/t_{SB}) and W is the linear softening rate measured in terms of the strength loss per unit shear

strain (= (σ_c - σ_r)/ε_c). Taking L_{SB} ~ 500 nm, α ~ 1, t_{SB} ~ 20 nm and G ~ 30 GPa, the linear softening rate W can be then estimated to be ~1.2 GPa per unit strain for the Zr-based MG under investigation.

3.4.5 The Rate Dependence of Shear Softening

According to Eq. (3.6), any change in G, t_{SB} or W could result in the variation in L_{SB}. For our experiments, G remains unaltered while t_{SB} should be a constant according to Ref.(Zhang and Greer 2006b). In such a case, we are left with no choice but the shear softening rate W to explain the rate dependence of L_{SB}. According to Fig. 3.5(b), it can be inferred that a rise in L_{SB} must correspond to a drop in W with an increasing shear rate. To verify this, we turn to molecular dynamics (MD) simulations and theoretical modeling. Before getting into the details, it should be emphasized that, given the assumptions made in deriving Eq.(3.5) and (3.6), the following MD simulations and theoretical modeling are only meant for checking the validity of the trend shown by our experimental data.

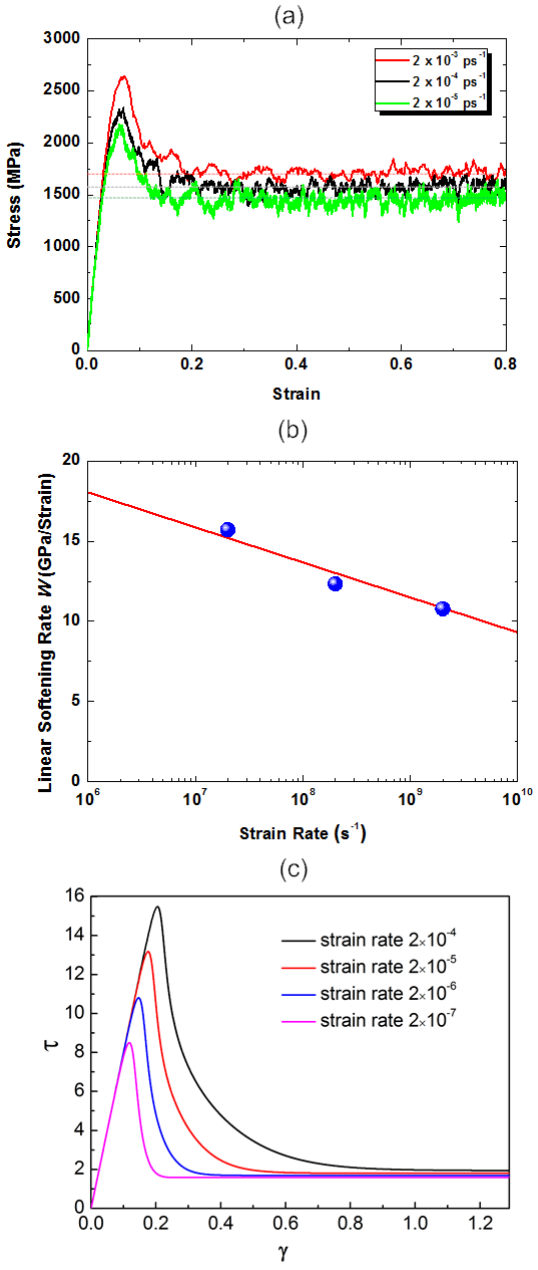

Figure 3.8 (a) The compressive stress-strain curves obtained from the MD simulation of a $Zr_{50}Cu_{50}$ MG for the different strain rates (the dashed lines indicate the level of the steady-state residual strength remaining after the initial fast softening), (b) the linear softening rate *W* derived from (a) and (c) the shear stress-strain curves obtained from the classic free-volume model for the different strain rates.

To carry out the MD simulations, we chose a model system of $Cu_{50}Zr_{50}$ MG which contains 50000 atoms built upon the realistic embedded-atom method potential (Mendelev et al. 2009) and has the dimensions of ~95.6 nm × ~95.6 nm × ~95.6 nm. To prepare the MG, the system was virtually equilibrated at the temperature T = 2000 K for 100 ps and then quenched to 100 K at the cooling rate of 10^{11} K s^{-1}. To simulate the compressive behavior of the MG, periodic boundary conditions were applied to all three sample dimensions and compressive loading was then applied using the Nose-Hoover chain method (Mundy et al. 2007, Tuckerman and Martyna 1999) under the NPT condition. The simulation results are expected to shed light on the possible rate effect on the stress-induced softening behavior of MGs.

Figure 3.8(a) displays the compressive stress-strain curves obtained respectively for the strain rates of 2 x 10^{-5} ps^{-1}, 2 x 10^{-4} ps^{-1} and 2 x 10^{-3} ps^{-1}. To facilitate the comparison, the baselines shown in Fig. 3.7(a) indicate the level of the steady-state flow stress, σ_r, at the corresponding strain rate. Evidently, σ_r increases with the increasing strain rate. According to the definition of W, we can thus compute W for the three strain rates, as indicated in Fig. 3.8(a). As shown in Fig. 3.8(b), W reduces as the strain rate increases, which agrees with what our experimental data imply. To further check if the trend revealed in Fig. 3.8(b) is generic to various kinds of MGs, we also performed a numerical simulation of the shear softening behavior in MGs using the classic free-volume model (please see **Appendix C** for details). From Fig. 3.8(c), it can be seen that the critical strain, at which the residual strength reduces to the steady state value,

increases significantly with the increasing strain rate, indicative of a more sluggish shear softening at a higher rate than at a lower rate. Again, this rate-dependent shear softening behavior is in line with our experimental data.

3.5 Implication

Before conclusion, let us discuss briefly one important implication of our current work. Recently, Tian et al. (Tian et al. 2012) proposed that the elastic limit of MG would approach an ideal value of ~8% when one could manage to reduce the size of a MG specimen without causing heterogeneous shear-band nucleation. Indeed, if one takes $p_c \sim 3\sigma_y$ (Ye et al. 2012), where σ_y represents the yield strength of a MG, it can be inferred from our experiments [Fig. 3.3(d)] that the elastic limit of our MG sample simply increases from ~2% to ~5%, which is very close to what Tian et al. previously reported(Tian et al. 2012). Furthermore, should the concept of ideal elastic limit still hold (Tian et al. 2012), one can infer that there is still space for us to further increase the hardness of the MG by using a smaller indenter. Nevertheless, with further reduction in the tip radius, one may enter the size regime where structural heterogeneity and Weibull statistics plays an important role. In that case, it becomes possible that the size effect law proposed in the current work may need revision by taking into account the effect of structural heterogeneity in MGs.

3.6 Conclusions

To conclude, we develop a theoretical model based on the notion of size-controlled shear-band nucleation to account for the indentation size effect in MGs. Through carefully designed experiments, this model prediction is justified on the Zr-based MG. By fitting the experimental data to the theory, we are able to extract the shear-band nucleation length from the trend of indentation size effect for different indentation strain rates. Our results show that shear band nucleation in the Zr-based MG exhibits slight rate dependence, which can be rationalized by the rate-affected shear softening behavior in MGs. Finally, it is worth pointing out that the experimental/theoretical framework herein established is rather general and should be applicable to other MG alloys or even other types of glassy materials, as long as an appropriate constitutive relation is available for describing the local yielding of the glassy material.

3.7 Appendix A

To fit out the functional form of Eq.(2), we need to simulate the growth of the local plastic zone with the applied indentation load *P*, as shown in Fig.1. Generally, the size of the local plastic zone D_{LPZ} can be expressed as:

$$D_{LPZ} = g\left(P, R, E_r, \sigma_0, \beta\right) \tag{A1}$$

where E_r is the reduced modulus, σ_0 and β define the following pressure-dependent Drucker-Prager (DP) yield criterion:

$$\sigma_e = \sigma_0 - \beta\sigma_m \tag{A2}$$

in which σ_e is the effective stress and σ_m is the mean or hydrostatic stress.

Converting (A1) to the dimensionless form gives:

$$\frac{D_{LPZ}}{R} = \Psi\left(\frac{p_m}{E_r}, \frac{\sigma_0}{E_r}, \beta\right) \tag{A3}$$

where $p_m = P/\pi a^2$ is the indentation mean pressure and *a* is the contact diameter which can be expressed in terms of *P*, *R*, and E_r.

Table S1 lists the tensile (σ_t) and compressive (σ_c) strengths measured for various Zr-based MGs. According to the DP model [Eq.(A2)], $\sigma_0 = \frac{2}{\sqrt{3}}\frac{\sigma_t\sigma_c}{\sigma_t + \sigma_c}$ and $\beta = \sqrt{3}\frac{\sigma_c - \sigma_t}{\sigma_t + \sigma_c}$. Therefore, according to the available experimental data listed in Table S1, it is seen that the dimensionless factor β would range from 0.01 to 0.1 while σ_0/E_r should be around 0.01 if E_r~100 GPa. As such, the values of the dimensionless factors β and σ_0/E_r were selected for the FE simulations in such a way that the available experimental data are covered.

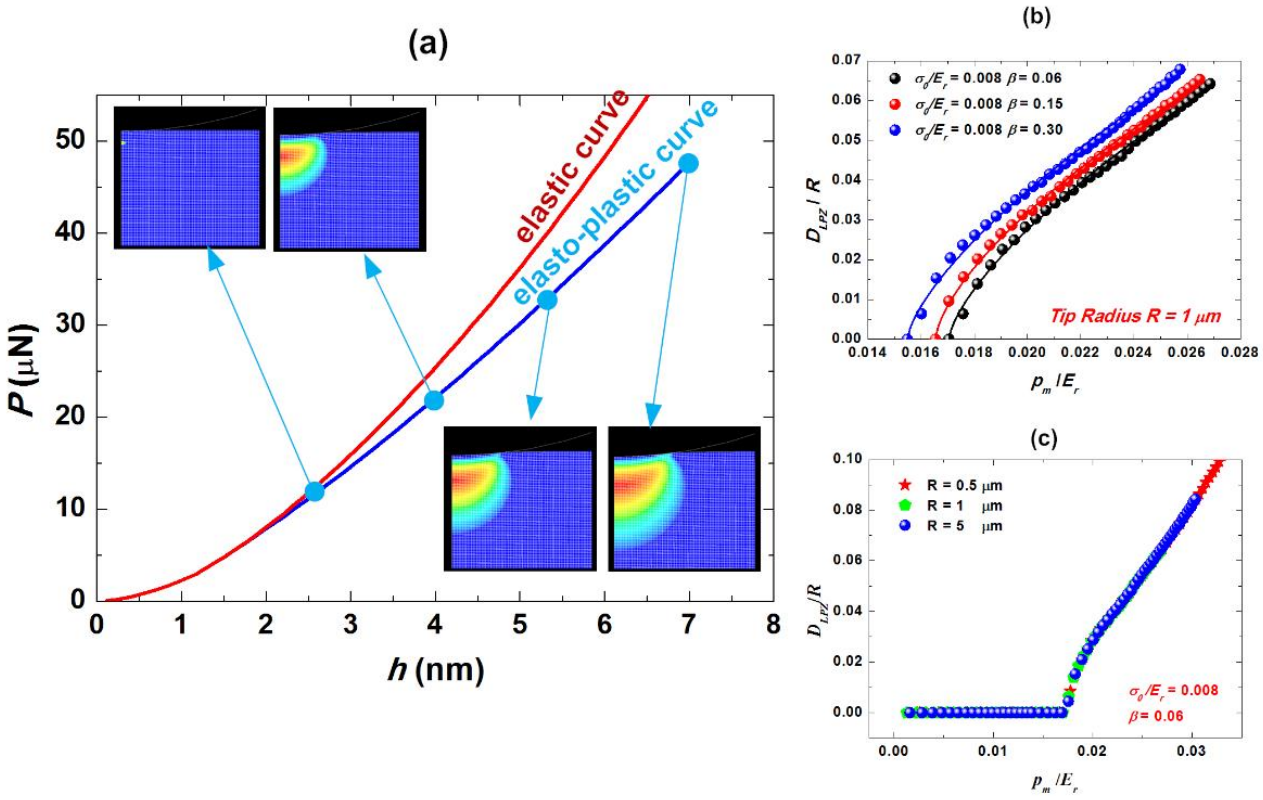

Figure A1. (a) The comparison of the typical elastic and elasto-plastic load-displacement curves obtained from the finite element (FE) simulations (insets: the simulated local plastic zones at the different indentation loads), (b) the typical curves of D_{LPZ}/R versus p_m/E_r at the different values of β and σ_0 for R = 1 μm, and (c) the typical curves of D_{LPZ}/R versus p_m/E_r at different R's for σ_0/E_r = 0.008 and β = 0.06.

Figure A1(a) displays two typical load (P) – displacement (h) curves obtained respectively from the simulated elastic and elasto-plastic indentations. On the same plot also shown are the series of the simulated local plastic zones under the spherical indenter at the different loads. Note that the deformation behavior of each single element was monitored during the FE simulation and the number of locally yielded

elements was counted at any stress levels for the different combination of the material parameters. To simplify our analysis, the size of the local plastic zone is defined as the diameter of the sphere that has the same volume as the real local plastic zone. To explore the dependence of the local plastic zone size, D_{LPZ} on β, σ_0/E_r and R, β is varied from 0.01 to 0.3 and σ_0/E_r from 0.006 to 0.012 for R = 0.5 μm, 1 μm and 5 μm.

For the purpose of clarity, only part of the simulation results is shown in Fig. A1(b) and (c). After compiling all the simulation data, we found that the following functional form fits the simulated zone size D_{LPZ} very well:

$$\frac{D_{LPZ}}{R} = A\left(\frac{p_m - p_0}{E_r}\right)^B \tag{A4}$$

where p_0 is the critical indentation mean pressure whose value depends on both σ_0/E_r and β, while A = 1.55 and B = 0.69 are the other two fitting parameters whose values are insensitive to the choice of σ_0 and β for $D_{LPZ}/R < 0.1$. Rearranging (A4) gives:

$$p_m = p_0 + E_r\left(\frac{D_{LPZ}}{AR}\right)^{\frac{1}{B}} \tag{A5}$$

Taking A=1.55, B=0.69, $L_{SB} = D_{LPZ}$ and $p_c = p_m$, we then obtain:

$$p_c = p_0 + 0.5E_r\left(\frac{L_{SB}}{R}\right)^{1.45} \tag{A6}$$

3.8 Appendix B

The nominal tip radii of the currently used spherical indenters, as provided by the manufacturer, are 2 μm, 5 μm, 10 μm, 20 μm, 40 μm, 60 μm and 80 μm. Before the indentation tests, the indenter tip shapes were all calibrated according to the following procedure. Firstly the reduced modulus of the Zr-based MG was determined by the classic Oliver-Pharr based nanoindentation method, which was 100 ± 8 GPa. After that, we fit out the real tip radii of the spherical indenters by equating the reduced modulus, as predicted by the Hertzian theory, to the measured one from the classic nanoindentation test. The experimental results showed that the real tip radii of the spherical indenters were consistent with the nominal ones for the small indenters while much smaller than the nominal ones for the big indenters.

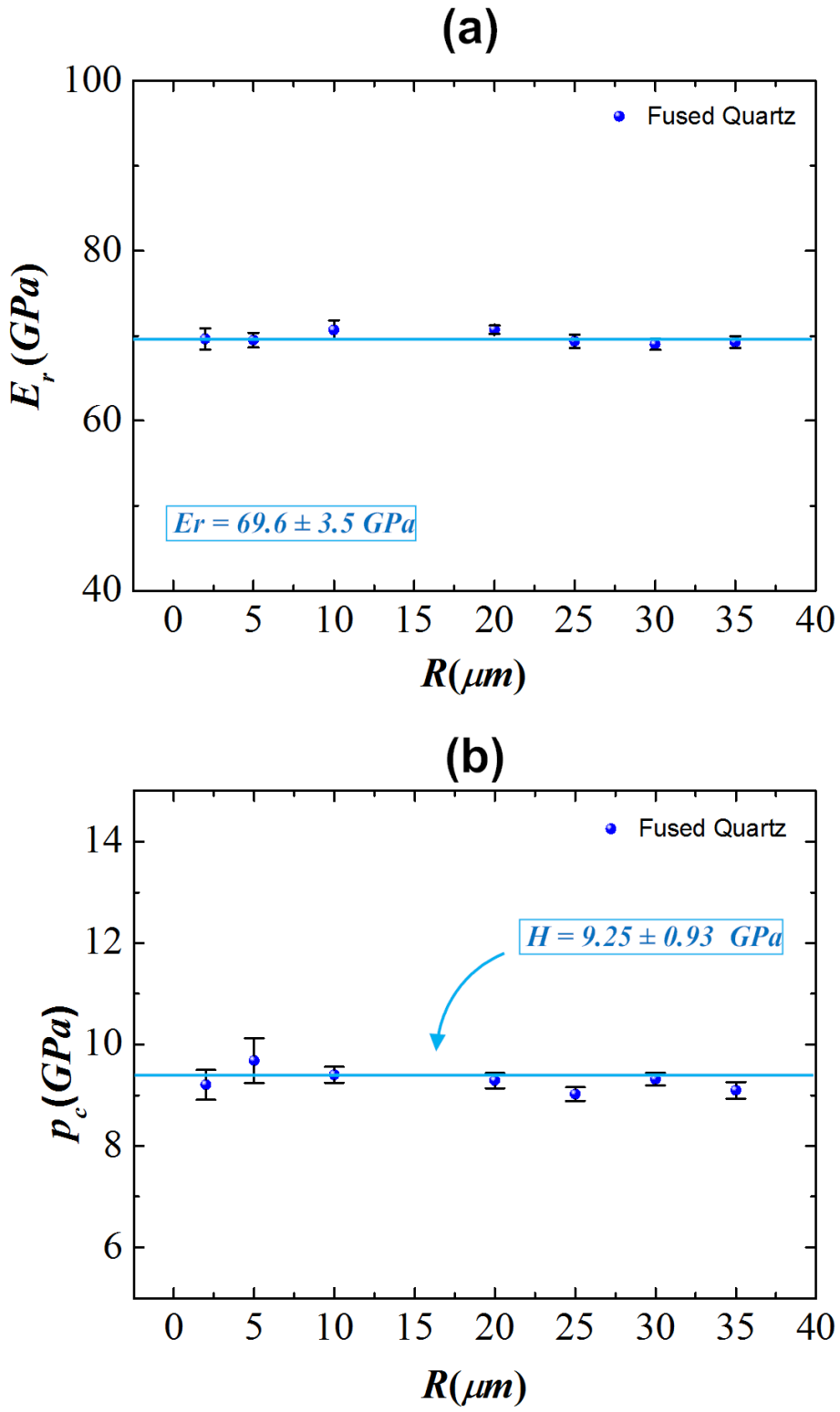

Figure A2 (a) The measured reduced modulus E_r and (b) the critical mean pressure or hardness p_c of fused quartz remaining constant for the different indenter tip radii after tip shape calibration.

To double check the validity of the above method, we also performed a series of spherical indentation tests on fused quartz with the calibrated spherical indenters. As shown in Fig. A2 (a), with the corrected tip radius, the reduced modulus of the fused quartz was measured to be a constant of 69.6 ± 3.5 GPa, which is in excellent agreement with the standard value and independent of the indenter tip radius. Furthermore, we also measured the critical mean pressure or hardness p_c of the fused quartz using our approach. In contrast to the Zr-based MG, the experimental results show that the hardness of the fused quartz keeps nearly to a constant of 9.25 ± 0.93 GPa [Fig. A2(b)], which implies that yielding of the fused quartz appears size insensitive with regard to the indenter tips we used.

3.9 Appendix C

According to the classic free-volume theory(Steif et al. 1982), the flow equations for MGs can be written as:

$$\dot{\bar{\upsilon}}_f = \upsilon^* v \exp\left[-\frac{\alpha\upsilon^*}{\bar{\upsilon}_f}\right]\exp\left[-\frac{\Delta G^m}{kT}\right]\left\{\frac{2\alpha kT}{\bar{\upsilon}_f \bar{S}}\left(\cosh\frac{\bar{\tau}\Omega}{2kT}-1\right)-\frac{1}{n_D}\right\} \tag{A7}$$

$$\frac{\dot{\bar{\tau}}}{\bar{G}} + 2v\exp\left[-\frac{\alpha\upsilon^*}{\bar{\upsilon}_f \bar{S}}\right]\exp\left[-\frac{\Delta G^m}{kT}\right]\sinh\left(\frac{\bar{\tau}\Omega}{2kT}\right) = \dot{\gamma} \tag{A8}$$

Where $\bar{\upsilon}_f$ is the average free volume per atom, α is the geometrical factor of the order of 1, υ^* is the critical volume, v is the frequency of atom vibration, ΔG^m is the activation energy for atom jump, $\bar{G}$ is the shear modulus, $\bar{\tau}$ is the shear stress, k is the Boltzmann constant, Ω is the atomic volume, $\dot{\gamma}$ is the external strain rate.

Introducing the following dimensionless variables:

$$\upsilon_f = \bar{\upsilon}_f / \alpha\upsilon^* \qquad \tau = \bar{\tau}\Omega / 2kT$$

$$t = R\bar{t} \qquad G = \bar{G}\Omega / 2kT$$

where

$$R = v\exp\left[-\frac{\Delta G^m}{kT}\right]$$

Equations of (A7) and (A8) then become:

$$\alpha\upsilon'_f = \exp(-1/\upsilon_f)\left[\frac{\cosh\tau - 1}{G\beta\upsilon_f} - \frac{1}{n_D}\right] \tag{A9}$$

$$\frac{\tau'}{G} + 2\exp(-1/\upsilon_f)\sinh\tau = \gamma' \tag{A10}$$

To obtain Fig. 6(c), the following values were used for solving Eqs. (A9) and (A10): v_f=0.04, τ=0 and α=1; β=1; G=80; γ'=2×10^{-4}, 2×10^{-5}, 2×10^{-6}, 2×10^{-7}, 2×10^{-4}.

3.10 Reference

Argon, A. S. (1979) Plastic deformation in metallic glasses. *Acta Metallurgica,* 27**,** 47-58.

Ashby, M. F. & A. L. Greer (2006) Metallic glasses as structural materials. *Scripta Mater.,* 54**,** 321-326.

Barenblatt, G. I. 2009. *Scaling, Self-similarity, and Intermediate Asymptotics: Dimensional Analysis and Intermediate Asymptotics* Cambridge, New York, Melbourne, Madrid, Cape Town, Singapore, Sao Paulo, Delhi: Cambridge University Press.

Begley, M. R. & J. W. Hutchinson (1998) The mechanics of size-dependent indentation. *Journal of the Mechanics and Physics of Solids,* 46**,** 2049-2068.

Bharathula, A. A.-L., Seok-Woo AU - Wright, Wendelin J. AU - Flores, Katharine M. (2010) Compression testing of metallic glass at small length scales: Effects on deformation mode and stability. *Acta Materialia* 58.

Chen, C. Q., Y. T. Pei & J. T. M. De Hosson (2010) Effects of size on the mechanical response of metallic glasses investigated through in situ TEM bending and compression experiments. *Acta Materialia,* 58**,** 189-200.

Chen, C. Q., Y. T. Pei & J. T. M. De Hosson (2012) Apparently homogeneous but intrinsically intermittent flow of taper-free metallic glass nanopillars. *Scripta Materialia,* 67**,** 947-950.

Chen, M. (2008) Mechanical Behavior of Metallic Glasses: Microscopic Understanding of Strength and Ductility. *Annual Review of Materials Research,* 38**,** 445-469.

Cheng, Y.-T. & C.-M. Cheng (2004) Scaling, dimensional analysis, and indentation

measurements. *Materials Science and Engineering: R: Reports,* 44**,** 91-149.

Cheng, Y. Q., Z. Han, Y. Li & E. Ma (2009) Cold versus hot shear banding in bulk metallic glass. *Physical Review B,* 80**,** 6.

Cheng, Y. Q. & E. Ma (2011) Intrinsic shear strength of metallic glass. *Acta Mater.,* 59**,** 1800-1807.

Choi, I.-C., Y. Zhao, Y.-J. Kim, B.-G. Yoo, J.-Y. Suh, U. Ramamurty & J.-i. Jang (2012) Indentation size effect and shear transformation zone size in a bulk metallic glass in two different structural states. *Acta Materialia,* 60**,** 6862-6868.

Evans, A. G. & J. W. Hutchinson (2009) A critical assessment of theories of strain gradient plasticity. *Acta Materialia,* 57**,** 1675-1688.

Greer, A. L., Y. Q. Cheng & E. Ma (2013) Shear bands in metallic glasses. *Materials Science and Engineering: R: Reports,* 74**,** 71-132.

Guo, H., P. F. Yan, Y. B. Wang, J. Tan, Z. F. Zhang, M. L. Sui & E. Ma (2007) Tensile ductility and necking of metallic glass. *Nature Materials,* 6**,** 735-739.

Huo, L. S., J. F. Zeng, W. H. Wang, C. T. Liu & Y. Yang (2013) The dependence of shear modulus on dynamic relaxation and evolution of local structural heterogeneity in a metallic glass. *Acta Materialia,* 61**,** 4329-4338.

Jang, D. C. & J. R. Greer (2010) Transition from a strong-yet-brittle to a stronger-and-ductile state by size reduction of metallic glasses. *Nature Materials,* 9**,** 215-219.

Jang, J.-i., B.-G. Yoo, Y.-J. Kim, J.-H. Oh, I.-C. Choi & H. Bei (2011) Indentation size effect in bulk metallic glass. *Scripta Materialia,* 64**,** 753-756.

Johnson, W. L. & K. Samwer (2005) A Universal Criterion for Plastic Yielding of

Metallic Glasses with a (T/Tg)2/3 Temperature Dependence. *Phys. Rev. Lett.*, 95**,** 195501.

Lee, C. J., Y. H. Lai, J. C. Huang, X. H. Du, L. Wang & T. G. Nieh (2010) Strength variation and cast defect distribution in metallic glasses. *Scripta Materialia,* 63**,** 105-108.

Liu, M. C., J. C. Huang, K. W. Chen, J. F. Lin, W. D. Li, Y. F. Gao & T. G. Nieh (2012) Is the compression of tapered micro- and nanopillar samples a legitimate technique for the identification of deformation mode change in metallic glasses? *Scripta Materialia,* 66**,** 817-820.

Liu, Y. H., D. Wang, K. Nakajima, W. Zhang, A. Hirata, T. Nishi, A. Inoue & M. W. Chen (2011) Characterization of Nanoscale Mechanical Heterogeneity in a Metallic Glass by Dynamic Force Microscopy. *Physical Review Letters,* 106**,** 125504.

Liu, Z., Y. Yang & C. Liu (2013) Yielding and shear banding of metallic glasses. *Acta Materialia,* 61**,** 5928-5936.

Mendelev, M. I., M. J. Kramer, R. T. Ott, D. J. Sordelet, D. Yagodin & P. Popel (2009) Development of suitable interatomic potentials for simulation of liquid and amorphous Cu-Zr alloys. *Philosophical Magazine,* 89**,** 967-987.

Miracle, D. B., A. Concustell, Y. Zhang, A. R. Yavari & A. L. Greer (2011) Shear bands in metallic glasses: Size effects on thermal profiles. *Acta Mater.,* 59**,** 2831-2840.

Mundy, C. J., S. Balasubramanian, K. Bagchi, M. E. Tuckerman, G. J. Martyna & M. L. Klein. 2007. Nonequilibrium Molecular Dynamics. In *Reviews in Computational Chemistry,* 291-397. John Wiley & Sons, Inc.

Nieh, T. G. & J. Wadsworth (2008) Bypassing shear band nucleation and ductilization of an amorphous-crystalline nanolaminate in tension. *Intermetallics,* 16**,** 1156-1159.

Nieh, T. G., Y. Yang, J. Lu & C. T. Liu (2012) Effect of surface modifications on shear banding and plasticity in metallic glasses: An overview. *Progress in Natural Science: Materials International,* 22**,** 355-363.

Nix, W. D. & H. Gao (1998) Indentation size effects in crystalline materials: A law for strain gradient plasticity. *Journal of the Mechanics and Physics of Solids,* 46**,** 411-425.

Packard, C. E., O. Franke, E. R. Homer & C. A. Schuh (2010) Nanoscale strength distribution in amorphous versus crystalline metals. *J. Mater. Res.,* 25**,** 2251-2263.

Packard, C. E., L. M. Witmer & C. A. Schuh (2008) Hardening of a metallic glass during cyclic loading in the elastic range. *Applied Physics Letters,* 92**,** -.

Pan, D., A. Inoue, T. Sakurai & M. W. Chen (2008) Experimental characterization of shear transformation zones for plastic flow of bulk metallic glasses. *Proceedings of the National Academy of Sciences,* 105**,** 14769-14772.

Schuh, C. A., T. C. Hufnagel & U. Ramamurty (2007) Mechanical behavior of amorphous alloys. *Acta Materialia,* 55**,** 4067-4109.

Schuh, C. A., A. C. Lund & T. G. Nieh (2004) New regime of homogeneous flow in the deformation map of metallic glasses: elevated temperature nanoindentation experiments and mechanistic modeling. *Acta Materialia,* 52**,** 5879-5891.

Schuster, B. E., Q. Wei, T. C. Hufnagel & K. T. Ramesh (2008) Size-independent strength and deformation mode in compression of a Pd-based metallic glass.

Acta Materialia, 56**,** 5091-5100.

Shimizu, F., S. Ogata & J. Li (2006) Yield point of metallic glass. *Acta Mater.,* 54**,** 4293-4298.

Spaepen, F. (1977) A microscopic mechanism for steady state inhomogeneous flow in metallic glasses *Acta Metallurgica,* 25**,** 407-415.

Sun, L., M. Q. Jiang & L. H. Dai (2010) Intrinsic correlation between dilatation and pressure sensitivity of plastic flow in metallic glasses. *Scripta Mater.,* 63**,** 945-948.

Swadener, J. G., E. P. George & G. M. Pharr (2002) The correlation of the indentation size effect measured with indenters of various shapes. *Journal of the Mechanics and Physics of Solids,* 50**,** 681-694.

Tabor, D. 2000. *The hardness of metals*. Oxford university press.

Tang, C., Y. Li & K. Zeng (2004) Characterization of mechanical properties of a Zr-based metallic glass by indentation techniques. *Materials Science and Engineering: A,* 384**,** 215-223.

Tian, L., Y.-Q. Cheng, Z.-W. Shan, J. Li, C.-C. Wang, X.-D. Han, J. Sun & E. Ma (2012) Approaching the ideal elastic limit of metallic glasses. *Nat Commun,* 3**,** 609.

Tuckerman, M. E. & G. J. Martyna (1999) Understanding Modern Molecular Dynamics: Techniques and Applications. *The Journal of Physical Chemistry B,* 104**,** 159-178.

Uenishi, K. & J. R. Rice (2003) Universal nucleation length for slip weakening rupture instability under nonuniform fault loading. *J. Geophys. Res.,* 108**,** 2042.

Volkert, C. A., A. Donohue & F. Spaepen (2008) Effect of sample size on deformation in amorphous metals. *Journal of Applied Physics,* 103.

Wagner, H., D. Bedorf, S. Küchemann, M. Schwabe, B. Zhang, W. Arnold & K. Samwer (2011) Local elastic properties of a metallic glass. *Nat Mater,* 10**,** 439-442.

Wang, C.-C., J. Ding, Y. Q. Cheng, J.-C. Wang, L. Tian, J. Sun, Z. W. Shan, J. Li & E. Ma (2012) Sample size matters for $Al_{88}Fe_7Gd_5$ metallic glass: Smaller is stronger. *Acta Mater.,* 60**,** 5370-5379.

Wu, W. F., Y. Li & C. A. Schuh (2007) Strength, plasticity and brittleness of bulk metallic glasses under compression: statistical and geometric effects. *Philosophical Magazine,* 88**,** 71-89.

Yang, Y. & C. Liu (2012) Size effect on stability of shear-band propagation in bulk metallic glasses: an overview. *Journal of Materials Science,* 47**,** 55-67.

Yang, Y., J. C. Ye, J. Lu, Y. F. Gao & P. K. Liaw (2010a) Metallic glasses: Gaining plasticity for microsystems. *JOM-US,* 62**,** 93-98.

Yang, Y., J. C. Ye, J. Lu, Q. Wang & P. K. Liaw (2010b) Revelation of the effect of structural heterogeneity on microplasticity in bulk metallic-glasses. *J. Mater. Res.,* 25**,** 563-575.

Yang, Y., J. F. Zeng, A. Volland, J. J. Blandin, S. Gravier & C. T. Liu (2012) Fractal growth of the dense-packing phase in annealed metallic glass imaged by high-resolution atomic force microscopy. *Acta Materialia,* 60**,** 5260-5272.

Yavari, A. R., K. Georgarakis, W. J. Botta, A. Inoue & G. Vaughan (2010) Homogenization of plastic deformation in metallic glass foils less than one micrometer thick. *Phy. Rev. B,* 82**,** 172202.

Ye, J., J. Chu, Y. Chen, Q. Wang & Y. Yang (2012) Hardness, yield strength, and plastic flow in thin film metallic-glass. *Journal of Applied Physics,* 112**,** 053516-053516-9.

Ye, J., J. Lu, Y. Yang & P. Liaw (2009a) Study of the intrinsic ductile to brittle transition mechanism of metallic glasses. *Acta Materialia,* 57**,** 6037-6046.

Ye, J. C., J. Lu, C. T. Liu, Q. Wang & Y. Yang (2010a) Atomistic free-volume zones and inelastic deformation of metallic glasses. *Nat Mater,* 9**,** 619-623.

Ye, J. C., J. Lu, Y. Yang & P. K. Liaw (2009b) Effects of sample geometry on deformation modes of bulk metallic glasses at the nano/micrometer scale. *Journal of Materials Research,* 24**,** 3465-3468.

Ye, J. C., J. Lu, Y. Yang & P. K. Liaw (2010b) Extraction of bulk metallic glass yield strengths using tapered micropillars in micro-compression experiments. *Intermetallics,* 18**,** 385-393.

Zeng, J. F., J. P. Chu, Y. C. Chen, A. Volland, J. J. Blandin, S. Gravier & Y. Yang (2014) On the use of atomic force microscopy for structural mapping of metallic-glass thin films. *Intermetallics,* 44**,** 121-127.

Zhang, Y. & A. L. Greer (2006) Thickness of shear bands in metallic glasses. *Applied Physics Letters,* 89**,** 071907.

4 Residual Stress Effect on Nucleation of Shear-Band Instability

4.1 Introduction

Since the first report by Klement(W. Klement 1960) in 1960, bulk metallic glasses (BMGs) have attracted extensive interest because of their exclusive properties such as very high strength, hardness, elastic limit as well as good corrosion resistance (Byrne and Eldrup 2008, Cheng and Johnson 1987, Spaepen 1987, Dyre 2008, Greer 1993, Loffler 2003). However, their main drawback is their catastrophic brittle failure under uniaxial loading, initiating from severe plastic-strain localization in a narrow region called shear band (Schuh, Hufnagel and Ramamurty 2007). Shear band formation is generally recognized as a direct consequence of yielding or the onset of the plastic deformation. They instantaneously propagate through sample and cause fracture, thereby leading to limited ductility under uniaxial loadings or even under bending for some cases. In recent years, numerous studies were proposed to the stabilization of shear band propagation. Some of them were focused on incorporating second phases into BMG matrix (Kim et al. 2005), which show much better plasticity. Also BMGs show increased plasticity in bending and in compression after shot-peening (Zhang, Wang and Greer 2006, Wang et al. 2011). In Wang's work (Wang et al. 2011), the

hardness of BMG sample is affected by the present of residual stress. In other's work (Scudino et al. 2011), surface treatment effectively enhanced the tensile plastic deformability of BMGs due to the existence of residual stress, which confined the propagation of shear band. In this chapter, we use nanoindentation with spherical indenter to study the effect of residual stress on the nucleation of shear band instability.

4.2 Experiment

For this study, we chose a Zr-based bulk metallic glass as the model material, which has the chemical composition $Zr_{47}Cu_{46}Al_7$ (in atomic %). The structure of the BMG samples was examined by X-ray diffractometry (XRD, Co radiation) before and after the plastic bending. The XRD patterns, as shown in Fig. 4.1, only display a broad diffraction maximum without any detectable sharp Bragg peaks, indicative of an overall amorphous structure even after the plastic deformation.

We designed a plastic bending test which enables us to easily apply a severe plastic deformation in BMGs. After the plastic bending, the local mechanical properties were first measured on the Hysitron™ NanoIndenter system (Hysitron Inc, Minneapolis, MN) with a Berkovich diamond tip. Then the spherical nanoindentation experiments were subsequently carried out at strain control. For a systematic investigation, the following tip radii were used in the spherical indentation tests: 2μm, 5μm, 10μm and 20μm. In order to keep a constant strain rate, $dP/dt/P$ was set to be a constant, where dP/dt is the

indentation loading rate and P the indentation load. This leads to an exponential increase of P with the time, t, in the loading segment. For simplicity, unloading was programed to follow a constant unloading rate.

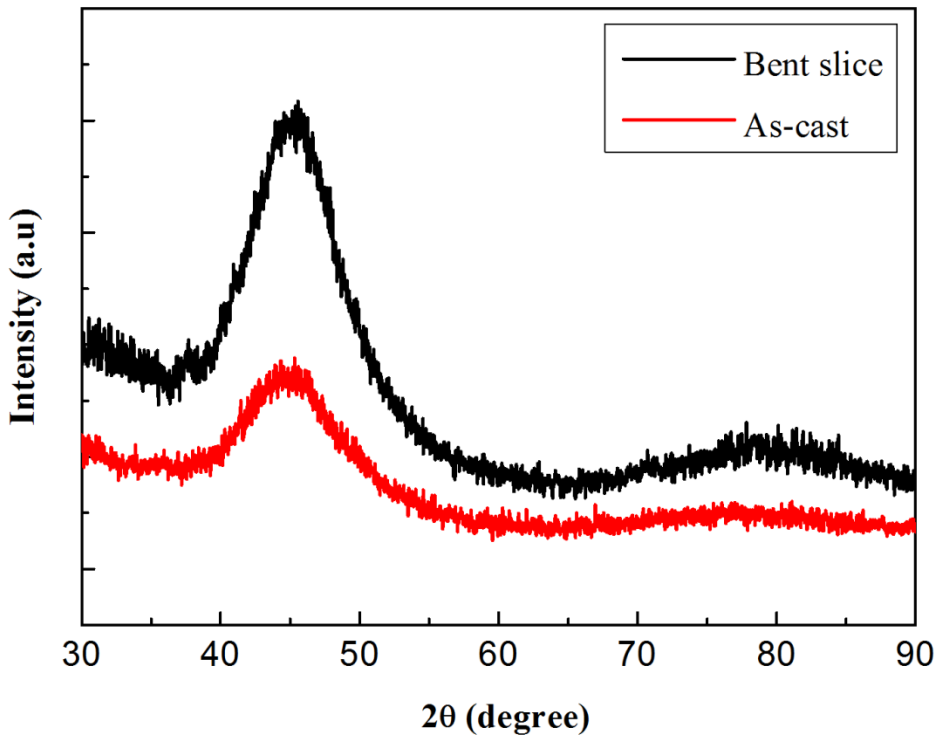

Figure 4.1 X-ray diffraction pattern of the bent slice and as-cast sample

4.3 Results and discussion

For the bending experiments, two bending samples (or slices) with the dimension of 10mm×3mm×0.42mm were prepared through the sectioning from a same BMG plate. Before bending, the top surfaces (10mm×3mm) of the slices were mechanically polished down to 10nm. Once one end fixed, the slices were subsequently bent at the

free end around the mandrels with different diameters, as shown in Fig 4.2. This experimental set-up can readily lead to a severe plastic deformation of the slices which is different from the conventional three- or four-point bending experiments.

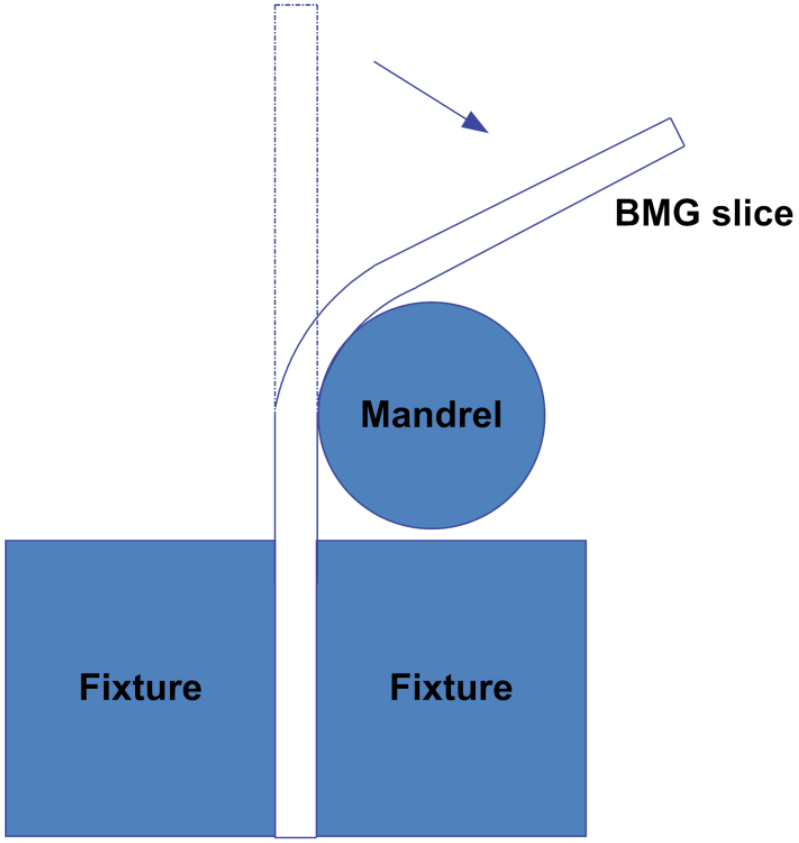

Figure 4.2 The sketch of the experimental set-up

To systematically study the residual stress effect, the two BMG slices were plastically bent to different curvatures without fracture. Next we measured the local mechanical properties with a Berkovich diamond tip. To ensure data reproducibility, the tests were set 30μm apart between indentation marks. Since the standard Oliver-Pharr method is no longer applicable for the indentations made in the region near the both-side edges(Oliver and Pharr 1992), the Joslin-Oliver method (Jakes et al. 2009)

was employed here for data analysis. Unlike the method of Oliver-Pharr(Oliver and Pharr 1992), which is based on three implicit assumptions: the sample has rigid support, it fills a half-space and it is homogeneous, the Joslin-Oliver method can remove the artifacts induced by edge effect.

Based on the Joslin-Oliver method(Jakes et al. 2009), the local hardness and Young's Modulus (the Poisson's ratio used for calculating the Young's modulus is 0.365) of the both BMG bent slices were measured by nanoindentation. The local hardness remains more or less at a constant of ~ 6 GPa for sample 1 while shows slightly increase from compression to tension site for sample 2. In contrast, there is no significant change in the measured local Young's Modulus. Regardless of the surface plastic strain, their values fluctuate around the average of 110 GPa.

In order to extract the residual stress for both bending sample, we firstly measured the shear offsets of each shear band on both tension and compression side and defined the maximum plastic strain with the following equation.

$$\varepsilon = \frac{\sum_{i=1}^{N_{so}} \Delta S_i \cos\theta}{S} \tag{4.1}$$

Where, ΔS_i is the length of i-th shear offset, N_{SO} is the number of shear offset, θ is tilt

angle of shear offset, *S* is the arc length of neutral axis. If we use the average length of shear offset, the Eq.4.1 can be further simplified. Because N_{SO}/S is equal to the shear offset density (ρ), the simplified plastic strain is $\varepsilon = \overline{\Delta s}\rho cos\theta$ and $\overline{\Delta s}$ is the average length of shear offset. Based on the above definition, we calculated both the maximum tension and compression plastic strain of two different samples. Then, according to Ye et al.(J. C. Ye, J. P. Chu et al. 2012) , the residual stresses on the compression sides were extracted, and all of them are listed in Table. 4.1.

Table 4.1 The maximum plastic strain on both tension and compression side of the two samples, and residual stress on compression side of all two samples

	ε_T	ε_C	σ_y(GPa)	σ_0(GPa)	σ_r(GPa)	
					DP model	MC model
Sample 01	0.02	0.02	2.0	2.0	--	--
Sample 02	0.05	0.03	2.1	1.9	0.174	0.156

Note: the subscripts T and C of plastic strain donate tension and compression.

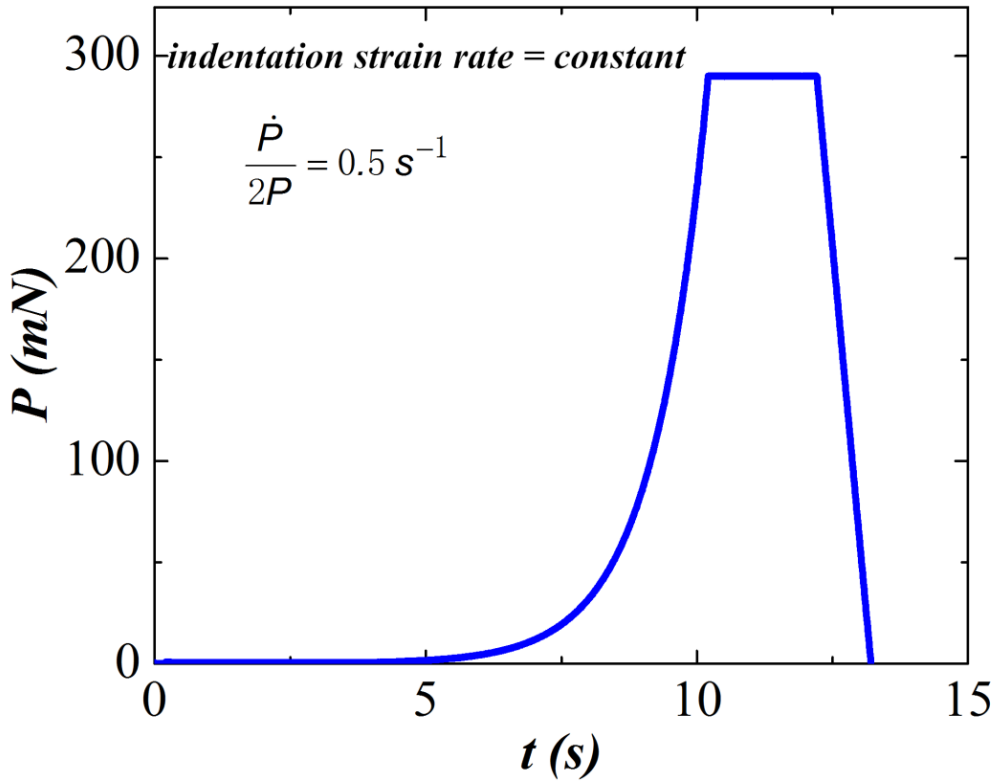

Figure 4.3 The programmed indentation load function for a constant strain-rate indentation test

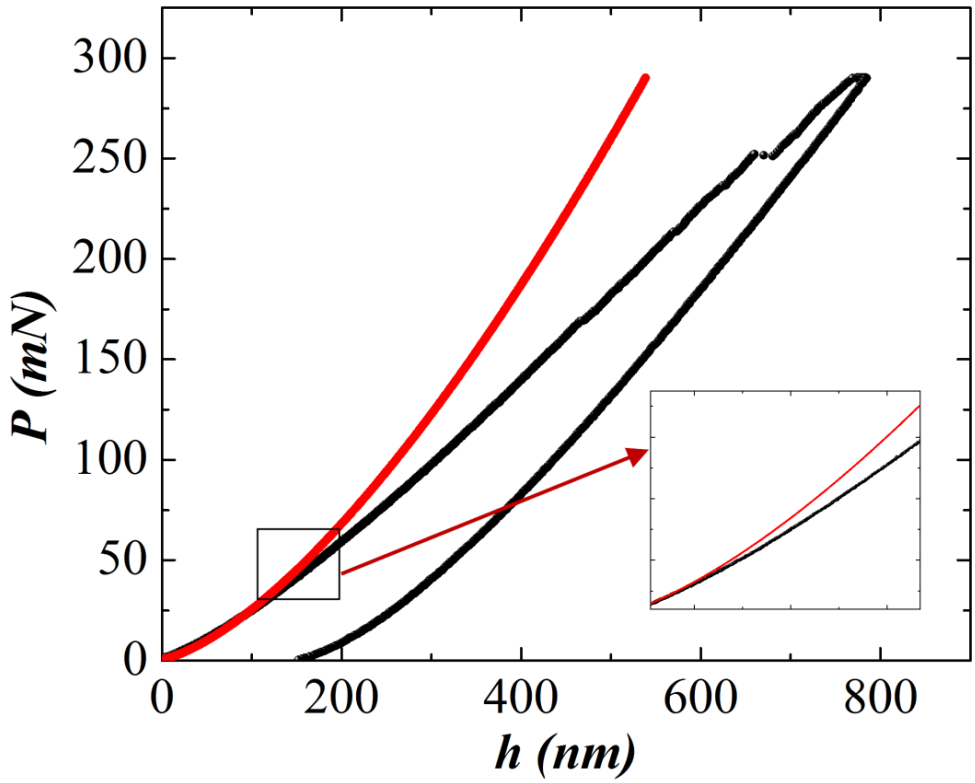

Figure 4.4 The typical indentation *P*-*h* curve (the black curve) in comparison with the Hertzian theory (the red curve) (inset = the enlarged view of the departure of the *P*-*h* curve from the Hertzian curve)

As shown in Fig 4.3, a load function with constant strain rate was employed. Figure 4.4 shows a typical load-displacement (*P*-*h*) curve of the sample 01 obtained at $\dot{\varepsilon} = 0.5s^{-1}$ and $R = 20\mu m$. According to the Hertzian theory, $P = (4E_rR^{1/2}/3)h^{3/2}$ for elastic indentation, where E_r denotes the reduced elastic modulus. In order to measure E_r reliably, same as the method in chapter 3, the experimental *P*-*h* curve was first converted to the *P*-$h^{3/2}$ curve and, subsequently, the linear portion of the latter was

utilized to fit out E_r via linear regression, as shown in Fig. 4.6. In this way, we can obtain E_r from the linear fitting with a high correlation coefficient. Afterwards, the real modulus, E, of the MG can be readily extracted from E_r by assuming a Poisson's ratio of ~0.365.

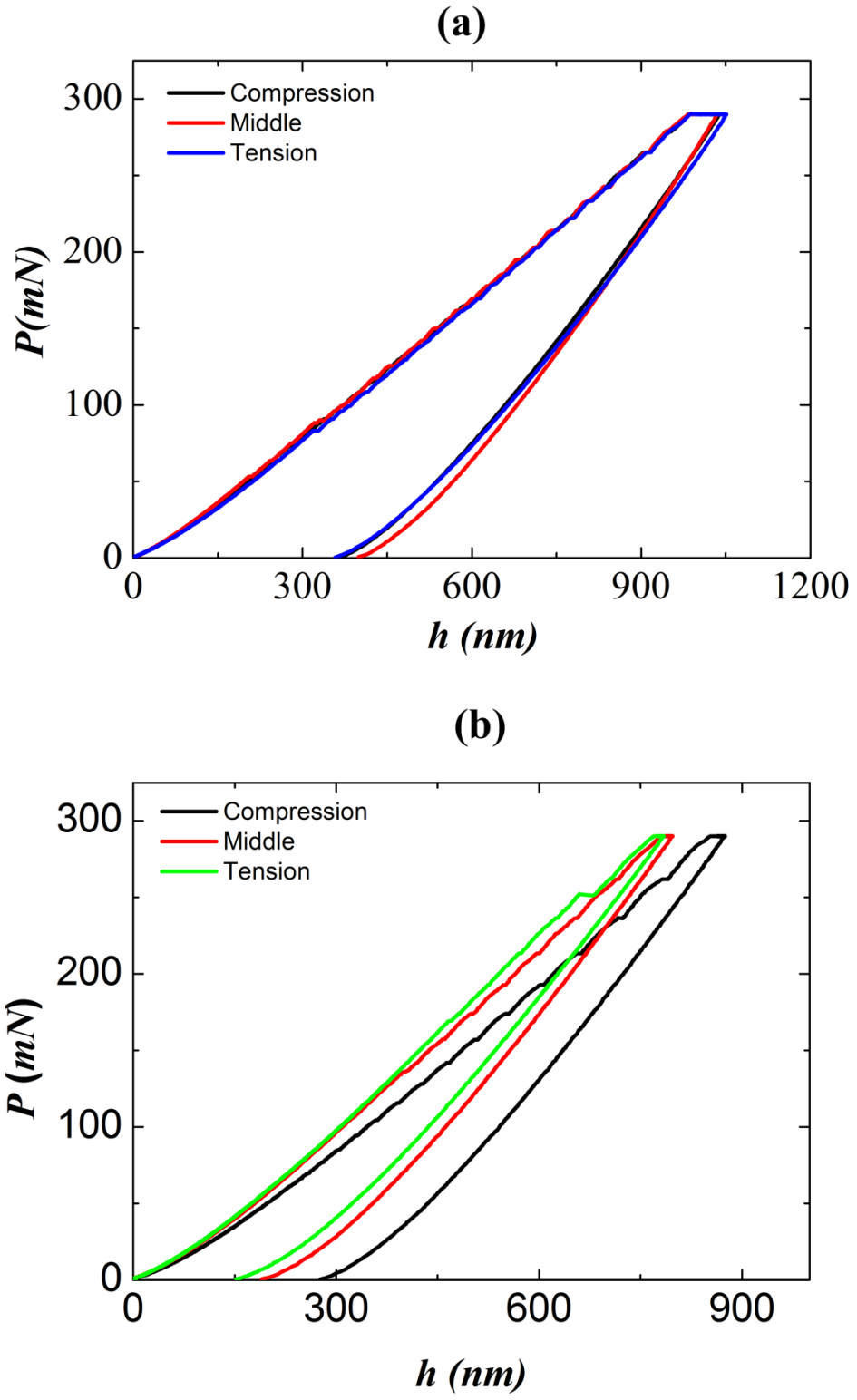

Figure 4.5 (a) The load-displacement (*P*-*h*) curve at $\dot{\varepsilon}$ = 0.5s^{-1} and *R* = 20μm on different site of sample 01(b) and sample 02

Figure 4.5 display the typical load displacement curves obtained from indenting the sample 01 at $\dot{\varepsilon}$ = 0.5s^{-1} and R = 20μm. From Fig. 4.5 (a), it is evident that all loading curves of sample 01 overlap for compression, middle and tension site. In contrast, the loading curves deviate significantly for different site of sample 02 which are shown in Fig. 4.5 (b). Afterwards, we compare the experimental *P-h* curve and the elastic Hertzian solution. Physically, yielding in a MG is initiated via a local 'de-caging' process. This can be interpreted as the break-down of the local elastic confinement that encapsulates the individual 'flow units' and thus **local yielding** amenable to the cooperative shear modeling. At a critical load, the local 'de-caging' effect spreads out with the flow units percolating through the elastic 'matrix'. Once a shear-band embryo can reach the critical nucleation length at yielding, resulting the **global yielding**. Here, it is worth emphasizing that the pop-in event is not corresponding to the activation of flow units.

The local elastic confinement firstly breakdown and the flow units start to percolate through local confinement. Once the critical length of the shear band reached, the whole system will undergo global yielding. Since our system has the displacement resolution of ~1 nm and force resolution of ~1μN, here the local yielding event is impossible to capture. Also the selection of the starting point of the global yielding will be an arbitrary process. So in our data analysis, as shown in Fig.4.6, we fit two parts of the curve, elastic and plastic process, respectively. The meeting point P_c represents the load at which a mature shear band is nucleated, corresponding to the global yielding of

metallic glasses in spherical indentation.

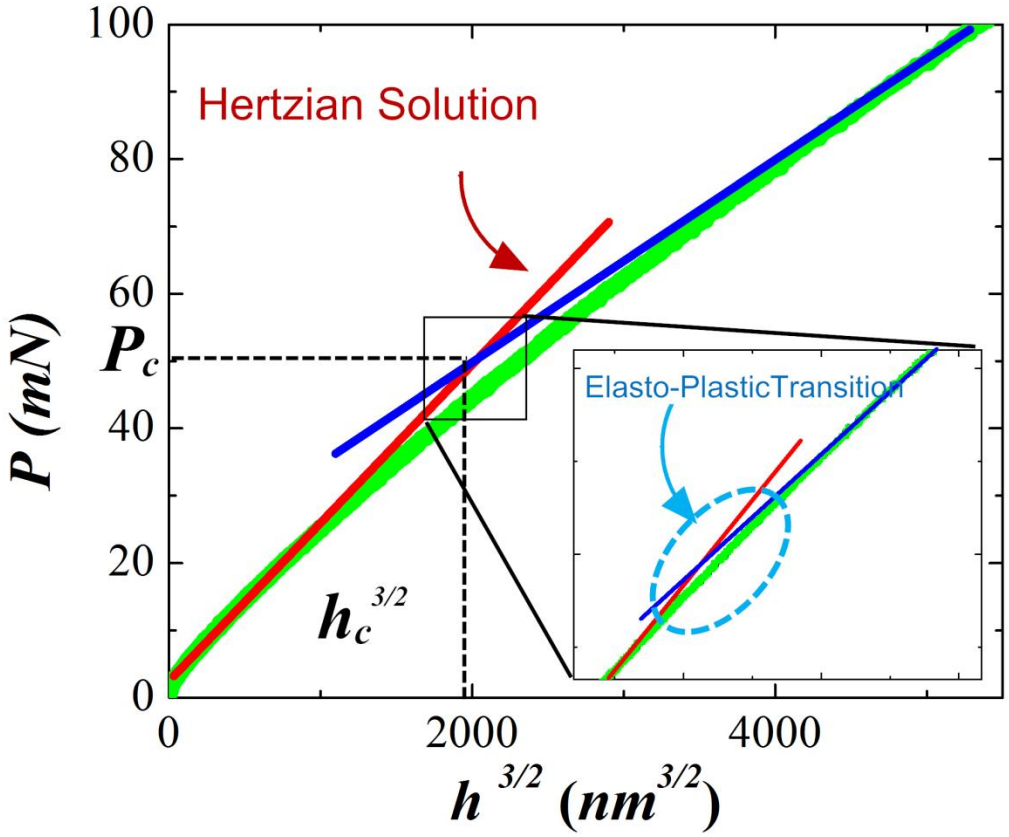

Figure 4.6 The linear fitting of the elastic portion (red curve) and the global plastic portion (blue curve) of the P-$h^{3/2}$ curve.

According to the Hertzian theory, the maximum pressure under the indenter is given by

$$p_c = \left(\frac{6PE_r^2}{\pi^3 R^2} \right)^{\frac{1}{3}} \tag{4.2}$$

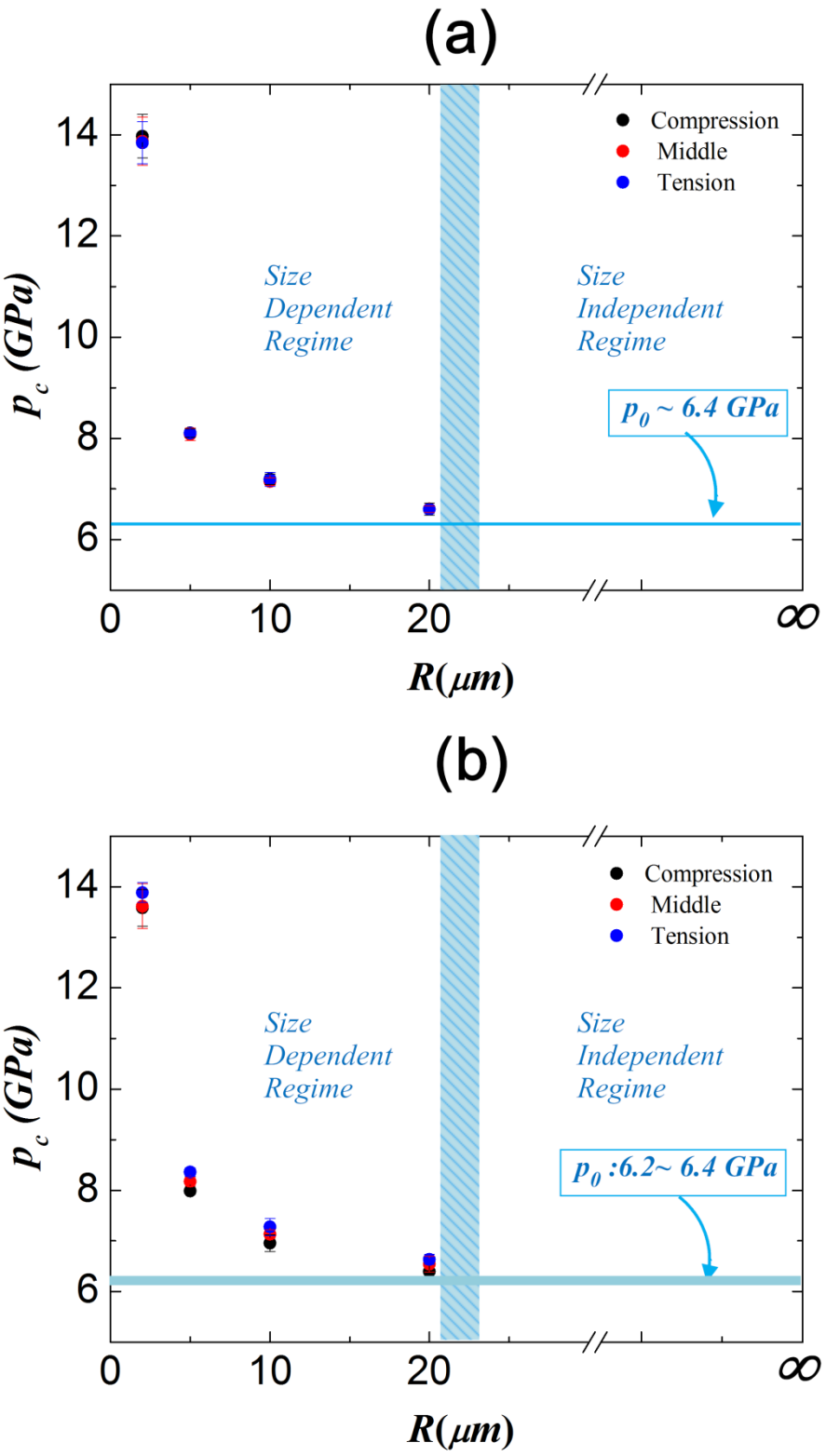

Figure 4.7 The strength size effect of the mean pressure in the different tip radius of compression, middle and tension site for (a) sample 01 and (b) sample 02

For each sample, we conducted around 10 nanoindentation tests on the sample surface of the compression, middle and tensile sites. Regardless of the different sample and sites, the measured E is around 110 GPa which is roughly same with the result from the Berkovich result. As shown in Fig. 4.7, the measured p_c exhibits a sharp strength size effect on both the samples with different residual stress, which increased dramatically with the decrease of the tip radius. In Chapter 3, it is obviously shows that the p_c remains at a constant value as the increased R which is equal to the hardness results from the classic Berkovich nanoindentation. So we can use hardness as p_0 which is the size-independent mean pressure.

According to $p_c = p_0 + C_0 E_r \left(\frac{L_{SB}}{R} \right)^{C_1}$ in Chapter 3 which predicts that *pc-p0* should scale with 1/R to the power of 1.45, we can now compare the experimental data to this scaling relation. As seen in Fig. 4.8, it can be seen that the prediction captures the experimental data very well for both sample 1 and 2. Furthermore, the shear band nucleation length L_{SB} can be extracted by fitting the experimental data to the theory. For sample 1, we obtain L_{SB} = 493$\pm$13 nm which is roughly the same for different sites. But the critical lengths are found to vary small but detectable increase from the compression to tension site. It indicates that compressive residual stress tends to slightly increase the nucleation size for shear band instability.

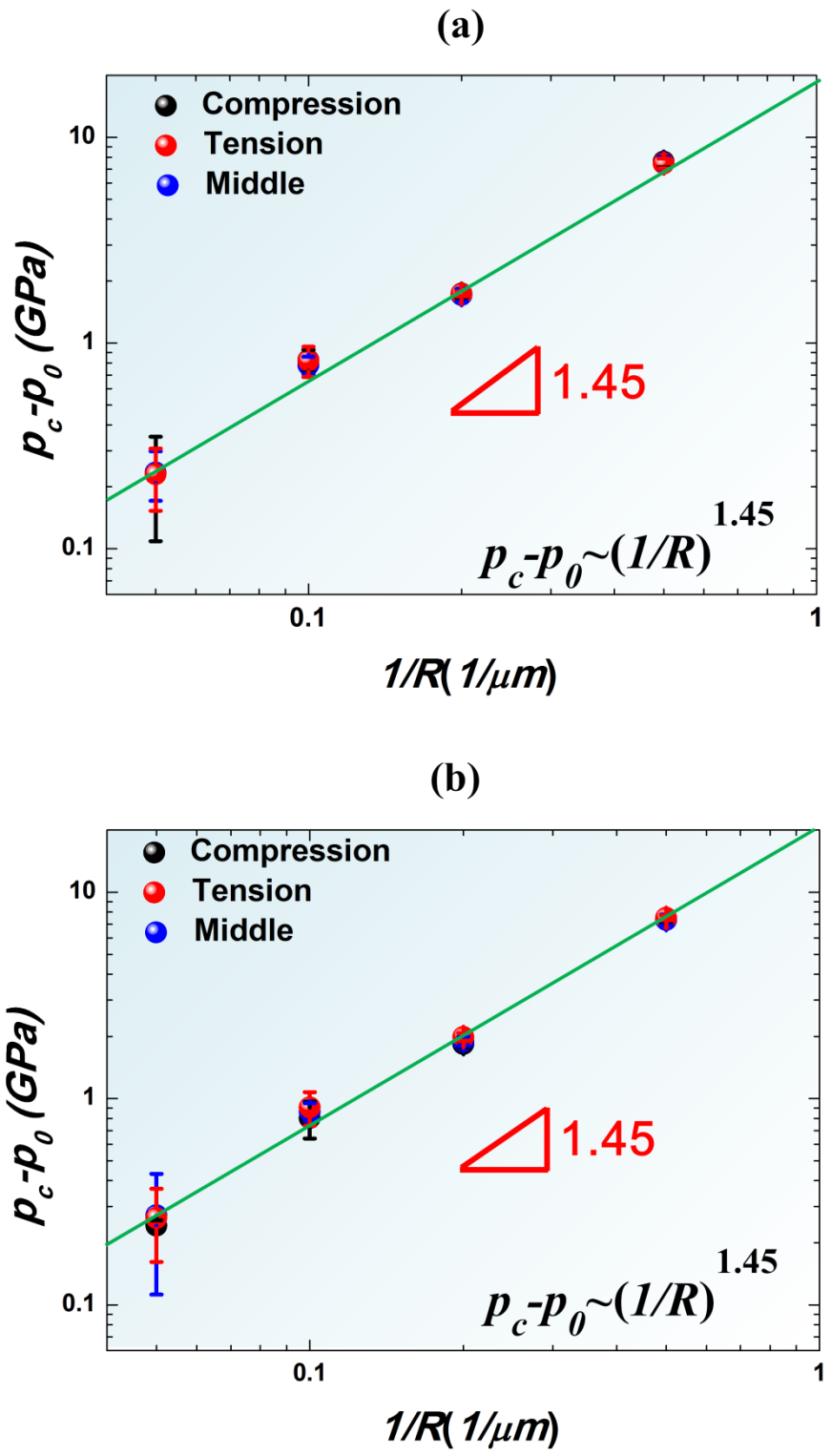

Figure 4.8 The comparison of the experimental data of p_c-p_0 of (a) sample 1 and (b) sample 2 versus 1/R with the theoretical predicted scaling ration.

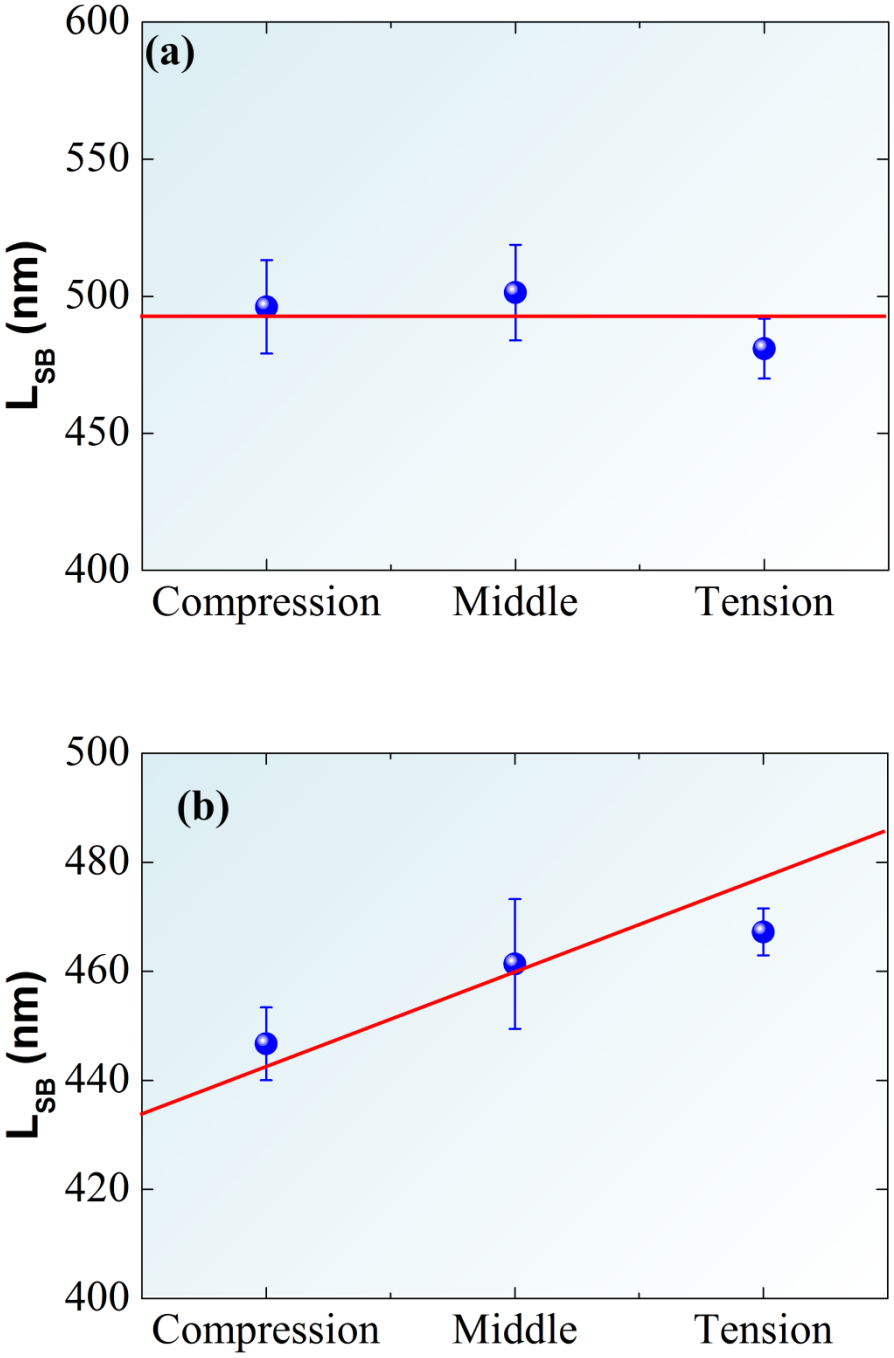

Figure 4.9 The variation of the extracted L_{SB} for (a) sample 1 and (b) sample 2 with the different residual stress state.

Based on the mechanism of shear-softening induced shear banding in MGs, Uenishi and Rice(Uenishi and Rice 2003) proposed a theoretical model for the shear softening induced instability. According to these authors (Uenishi and Rice 2003), the critical length of the shear-band embryo depends mainly on the elastic modulus of the elastic confinement and the that characterizes the strength loss in the shear-banding embryonic zone. Same as Chapter 3, for the sake of simplicity, there are some assumptions: (a) the material softening in the shear-band embryo to be a linear softening process, which is characterized by the local yield stress σ_c and the linear softening rate Θ; (b) we assume a steady-state residual strength σ_r that remains after the initial softening within the embryonic zone. So the critical shear-band nucleation length can be derived as:

$$L_{SB} = \alpha \frac{G}{\Theta} = \alpha t_{SB} \frac{G}{(\sigma_c - \sigma_r)/\varepsilon_c} = \alpha t_{SB} \frac{G}{W} \tag{4.3}$$

where α is a dimensionless factor roughly equal to ~1.16 and G is the shear modulus of the MG. Since $\Theta = (\sigma_c - \sigma_r)/\Delta$, where Δ is the critical shear displacement at which the initial softening process is completed, t_{SB} is the shear-band thickness (10-20 nm), ε_c is the critical shear strain (=Δ/t_{SB}) and W is the linear softening rate measured in terms of the strength loss per unit shear strain (= (σ_c - σ_r)/ε_c). Taking α ~ 1, t_{SB} ~ 20 nm and G ~ 37 GPa, the linear softening rate W can be then extracted in Table 4.2.

Table 4.2 The critical length and softening rate for sample 2

Sample 02	Compression	Middle	Tension
L_{SB} (nm)	~447	~461	~467
W (GPa/Strain)	~1.66	~1.60	~1.58

In previous studies, Scudino et al.(Scudino et al. 2011) found that imprinting can improve the plasticity of BMGs. They pressed a parallel-ridged template into the surfaces of Zr-based BMG specimen. The imprinting leads to a marked inhomogeneity: softening under the imprinted troughs and hardening between them, associated with plastic flow and with, respectively, tensile and compressive residual stresses. The imprinting leads to more diffuse yielding and distinctly improved ductility of up to 0.9%. Scudino et al. attributed the improved ductility to the easy initiation of shear bands in the soft regions and the blocking of potentially catastrophic shear-band propagation by the hard regions. Also from the work of Wang (Wang et al. 2011), compressive surface stresses can be induced by shot-peening in metallic glasses. They found that compressive residual stresses at surfaces constrain plastic deformation. From the theoretical model proposed by Uenish and Rice, we can be attributed the increase of the critical length to the following two factors: the increment of the elastic confinement and the decrease of the softening rate of the shear band embryo. From Table 4.2, we can found that the present of the compressive residual stress reduced the softening rate of the shear band embryo while the softening rate increased with the

presence of the tensile residual stress. The results confirm our speculation. At the meantime, the present of the compressive residual stress plays the same role of the increase of the elastic matrix for the growth of the shear band embryo. Therefore, the critical length for shear band nucleation under compressive residual stress will be increase due to the increased elastic confinement and the decrease of the shear softening rate.

4.4 Conclusion

In summary, through the nanoindentation study, we can extract the mechanical properties from the compressive to tensile site, it is shown that the elastic modulus of the material keeps at a constant while its hardness drops more significantly in the compression region than that in the tension region. Also, the experiment results confirm the theoretical model based on the notion of size-controlled shear-band nucleation. We are able to extract the shear-band nucleation length from the trend of indentation size effect for varies residual stress. Our results show that shear band nucleation in the Zr-based MG is influenced by the presence of compressive or tension residual stress, which can be rationalized by the different elastic confinement and shear softening rate in MGs. It indicates that compressive residual stress tends to slightly increase the nucleation size for shear band instability.

4.5 Reference

Byrne, C. J. & M. Eldrup (2008) Materials science - Bulk metallic glasses. *Science,* 321**,** 502-503.

Cheng, Y. T. & W. L. Johnson (1987) Disordered Materials - a Survey of Amorphous Solids. *Science,* 235**,** 997-1002.

Dyre, J. (2008) Mysteries of the glass transition. *Physics Today,* 61**,** 15-15.

Greer, A. L. (1993) Materials Science - Confusion by Design. *Nature,* 366**,** 303-304.

Jakes, J. E., C. R. Frihart, J. F. Beecher, R. J. Moon, P. J. Resto, Z. H. Melgarejo, O. M. Suarez, H. Baumgart, A. A. Elmustafa & D. S. Stone (2009) Nanoindentation near the edge. *Journal of Materials Research,* 24**,** 1016-1031.

Kim, Y. C., E. Fleury, J. C. Lee & D. H. Kim (2005) Origin of the simultaneous improvement of strength and plasticity in Ti-based bulk metallic glass matrix composites. *Journal of Materials Research,* 20**,** 2474-2479.

Loffler, J. F. (2003) Bulk metallic glasses (vol 11, pg 529, 2003). *Intermetallics,* 11**,** 979-979.

Oliver, W. C. & G. M. Pharr (1992) An Improved Technique for Determining Hardness and Elastic-Modulus Using Load and Displacement Sensing Indentation Experiments. *Journal of Materials Research,* 7**,** 1564-1583.

Schuh, C. A., T. C. Hufnagel & U. Ramamurty (2007) Mechanical behavior of amorphous alloys. *Acta Mater.,* 55**,** 4067-4109.

Scudino, S., B. Jerliu, S. Pauly, K. B. Surreddi, U. Kuhn & J. Eckert (2011) Ductile bulk metallic glasses produced through designed heterogeneities. *Scripta Materialia,* 65**,** 815-818.

Spaepen, F. (1987) The Art and Science of Microstructural Control. *Science,* 235**,** 1010-1014.

Uenishi, K. & J. R. Rice (2003) Universal nucleation length for slip weakening rupture

instability under nonuniform fault loading. *J. Geophys. Res.*, 108**,** 2042.

W. Klement, R. H. W., P.O.L. Duwez (1960). *Nature,* 187**,** 869-870.

Wang, L., H. Bei, Y. F. Gao, Z. P. Lu & T. G. Nieh (2011) Effect of residual stresses on the hardness of bulk metallic glasses. *Acta Materialia,* 59**,** 2858-2864.

Zhang, Y., W. H. Wang & A. L. Greer (2006) Making metallic glasses plastic by control of residual stress. *Nature Materials,* 5**,** 857-860.

5 Thermal Effect on Nucleation of Shear-Band Instability

5.1 Introduction

Metallic glasses (MGs) have exclusive properties such as high strength, high elastic limit and good corrosion resistance (Byrne and Eldrup 2008, Cheng and Johnson 1987, Spaepen 1987, Dyre 2008, Greer 1993, Loffler 2003). Unlike crystalline metals, of which the physical/mechanical properties can be derived from the interplay between their microstructures and crystalline defects, such as dislocations, MGs do not possess any 'microstructures' of long-range translational periodicity. Due to this structural amorphousness, it was a common notion, although being criticized recently(Egami 2011), that one has to nucleate or activate a flow 'defect', such as free-volume(Spaepen 1977) or shear transformation zone(Argon 1979), in order to trigger a plastic flow in MGs, which is similar to the case of defect nucleation/growth in an elastic solid. Once the surrounding elastic confinement break down, the flow 'defect' percolates through the elastic confinement. The shear-band embryo reaches the critical nucleation length at yielding, resulting the formation of shear band. Metallic glasses undergo plastic deformation by the nucleation and propagation of shear bands. Some studies made mechanical treatments studies on MGs, such as loading at stresses well below those for the onset of instantaneous yielding. Lee et al.(Lee et al. 2008) showed that pre-loading makes remarkable increases in compressive plasticity, from essentially 0 in as-cast samples to 5.2% in pre-loaded samples. It seems that the loading induces structural

rejuvenation in the samples, which is the opposite of the structural relaxation induced by thermal annealing. In contrast to the rejuvenation noted for pre-loading, Packard et al.(Packard et al. 2010) measured the yield load after applying loading and unloading cycles (as for the static loading, in the nominally elastic regime), which shows a clear hardening effect. Packard proposed that the metallic glass might thus reach highly compact states inaccessible by thermal annealing. These studies suggest the effect of the mechanical annealing on the initiation of shear bands; it remains to be studied whether or not shear-band propagation would be affected by annealing or thermal history. With carefully designed nanoindentation test, we study the thermal historic effect on the formation of shear band.

5.2 Experiment

A typical Zr-based BMG with the nominal composition of $Zr_{52.5}Ti_5Cu_{17.9}Ni_{14.6}Al_{10}$ (Vit105) was selected as the model material. The as-cast specimens were annealed at 653K for 61h and 256h, respectively. Then the samples were taken out from the furnace and cooled in air down to room temperature. The glassy ribbon was prepared by rapid quenching method with a cooling rate of 10^5 K/ s. The structure of the BMG samples was examined by X-ray diffractometry (XRD, Co radiation) before testing as shown in Figure 5.1. The XRD patterns only display a broad diffraction maximum without any detectable sharp Bragg peaks, indicative of an overall amorphous structure.

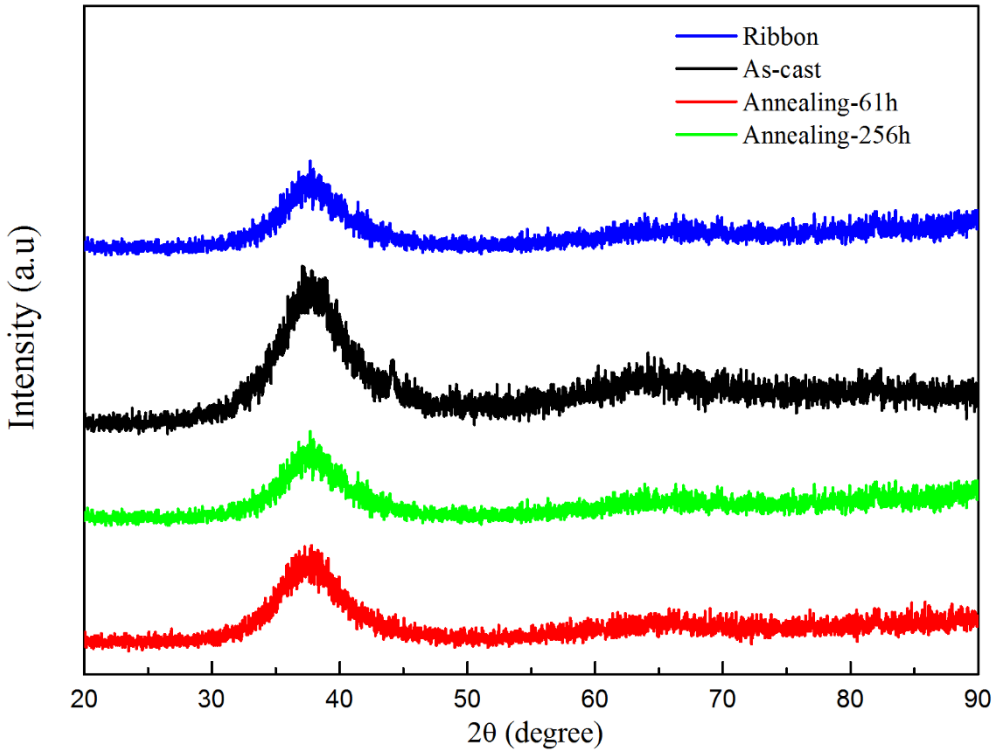

Figure 5.1 X-ray diffraction pattern of the samples with different thermal history

The local mechanical properties were first measured on the Hysitron™ NanoIndenter system (Hysitron Inc, Minneapolis, MN) with a Berkovich diamond tip. Then the spherical nanoindentation experiments were subsequently carried out at strain control on the Hysitron™ Nanoindentation System. For a systematic investigation, the following tip radii were used in the spherical indentation tests: 2μm, 5μm, 10μm and 20μm. In order to keep a constant strain rate, $dP/dt/P$ was fixed to be $0.2s^{-1}$, where dP/dt is the indentation loading rate and P the indentation load. This leads to an exponential increase of P with the time, t, in the loading segment. For simplicity, unloading was programed to follow a constant unloading rate.

5.3 Results and Discussion

The hardness and modulus (the Poisson's ratio used for calculating the Young's modulus is 0.365) of the four samples were first measured with a Berkovich diamond tip. To ensure data reproducibility, adjacent indentation marks were set 30μm apart. With the method of Oliver-Pharr(Oliver and Pharr 1992), the most widely used method for extraction of hardness and modulus by Berkovich nanoindentation. The measured hardness values for the four MG samples, including ribbon, as-cast, annealing after 61h and 256h, are 5.5GPa, 5.7GPa, 6.0GPa and 6.4GPa respectively, which show the dependence of thermal history. Accordingly, the hardness rises with increase of annealing time, while the ribbon one lower than the other three, demonstrating that denser structure has a higher hardness. Meanwhile, the measured Young's modulus of the ribbon and as-cast samples are ~92 and ~102GPa. With the increasing annealing time, the Young's modulus increase substantially from ~107 to ~112GPa. This trend is consistent with the previous finding(Lewandowski, Wang and Greer 2005). Annealing a metallic glass can trigger structural relaxation and affect elastic behavior. Although it is difficult to characterize the structural change precisely, irreversible relaxation is often associated with the changes of the topological short range order. Also the results show an increase in density with a corresponding increase in elastic modulus. Furthermore, due to both the inter-atomic spacing decreases and the topological changes, the anelastic internal rearrangement is more difficult.

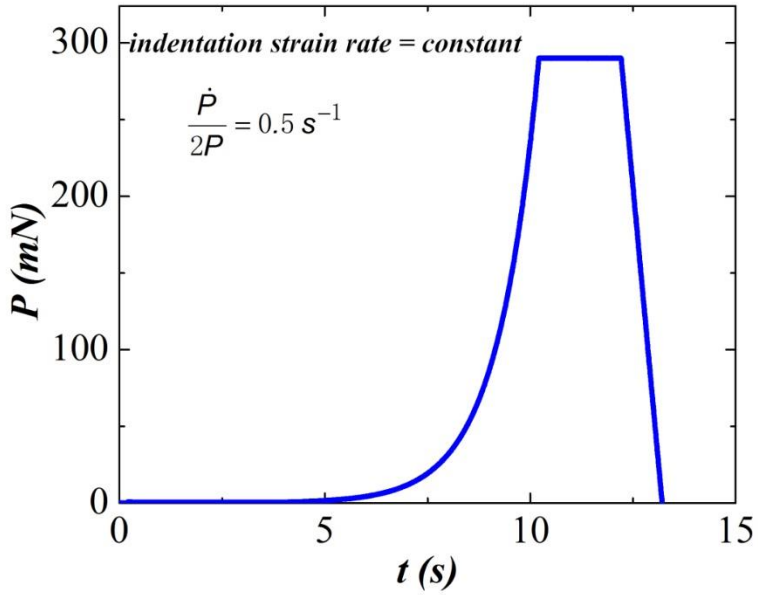

Figure 5.2 The programmed indentation load function for a constant strain-rate indentation test

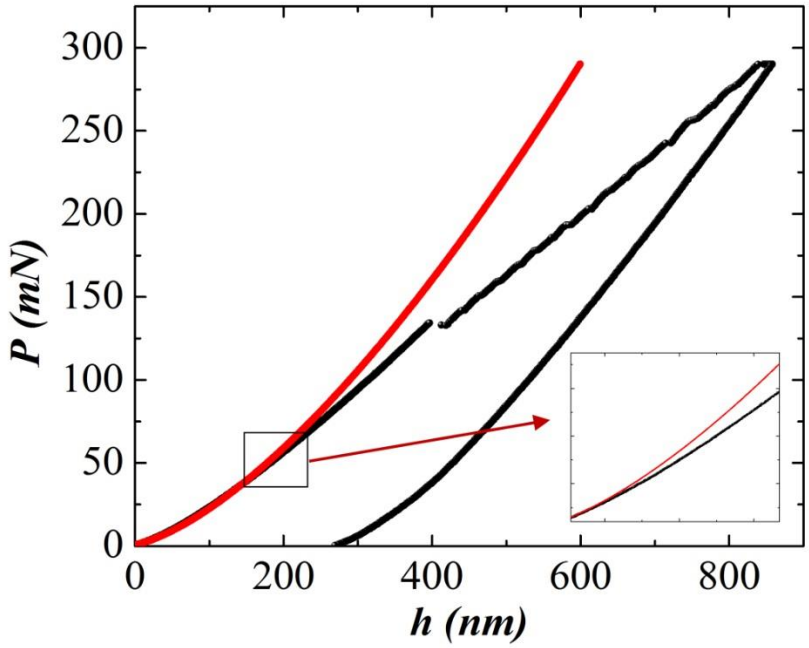

Figure 5.3 The typical indentation *P-h* curve (the black curve) in comparison with the Hertzian theory (the red curve) (inset = the enlarged view of the departure of the *P-h* curve from the Hertzian curve)

As shown in Fig 5.2, a load function with constant strain rate was employed. Figure 5.3 shows a typical load-displacement (*P*-*h*) curve of the specimen annealed for 256h, which is obtained at $\dot{\varepsilon} = 0.5s^{-1}$ and $R = 20\mu m$. According to the Hertzian theory, $P = (4E_rR^{1/2}/3)h^{3/2}$ for elastic indentation, where E_r denotes the reduced elastic modulus. In order to measure E_r reliably, same as the method in chapter 3, the experimental *P*-*h* curve was first converted to the $P\text{-}h^{3/2}$ curve and, subsequently, the linear portion of the latter was utilized to fit out E_r via linear regression, as shown in Fig. 5.4. In this way, we can obtain E_r from the linear fitting with a high correlation coefficient. Afterwards, the real modulus, *E*, of the MG can be readily extracted from E_r by assuming a Poisson's ratio of ~0.365.

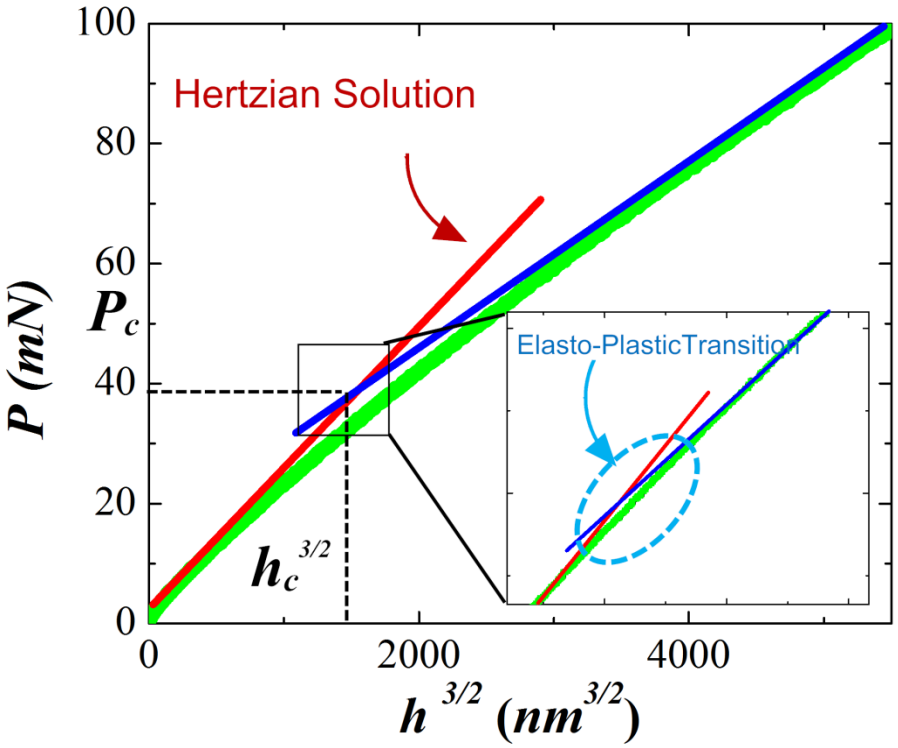

Figure 5.4 The linear fitting of the elastic portion (red curve) and the global plastic portion (blue curve) of the P-$h^{3/2}$ curve.

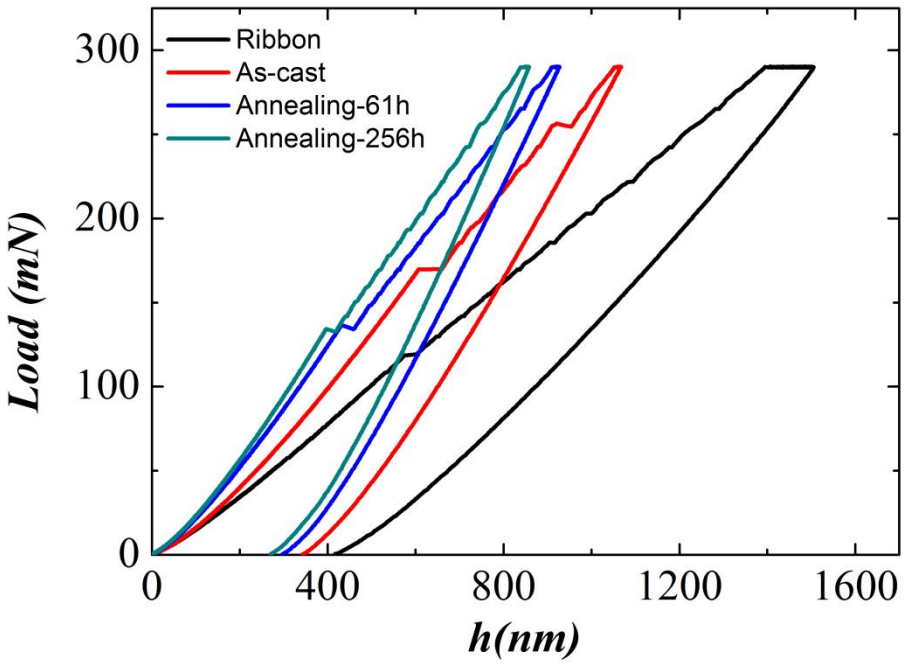

Figure 5.5 The load-displacement (*P-h*) curve at $\dot{\varepsilon}$ = 0.5s^{-1} and *R* = 20μm for the samples with various thermal history.

Figure 5.5 displays the typical load-displacement curves obtained from indenting the four samples at $\dot{\varepsilon}$ = 0.5s^{-1} and *R* = 20μm. obviously, the loading curves deviate significantly for different thermal history. The experimental finding clearly demonstrates that varying thermal history can affect the material's mechanical behavior measured from the nanoindentation. Afterwards, we compare the experimental *P-h* curve and the elastic Hertzian solution. Here, the selection of the starting point of the global yielding will be an arbitrary process. So in our data analysis, as shown in Fig.5.4, we fit two parts of the curve, elastic and plastic process, respectively. The meeting point P_c represents the load at which a mature shear band is nucleated, corresponding to the global yielding of metallic glasses in spherical indentation.

According to the Hertzian theory, the maximum pressure under the indenter is given by

$$p_c = \left(\frac{6PE_r^2}{\pi^3 R^2} \right)^{\frac{1}{3}} \tag{5.1}$$

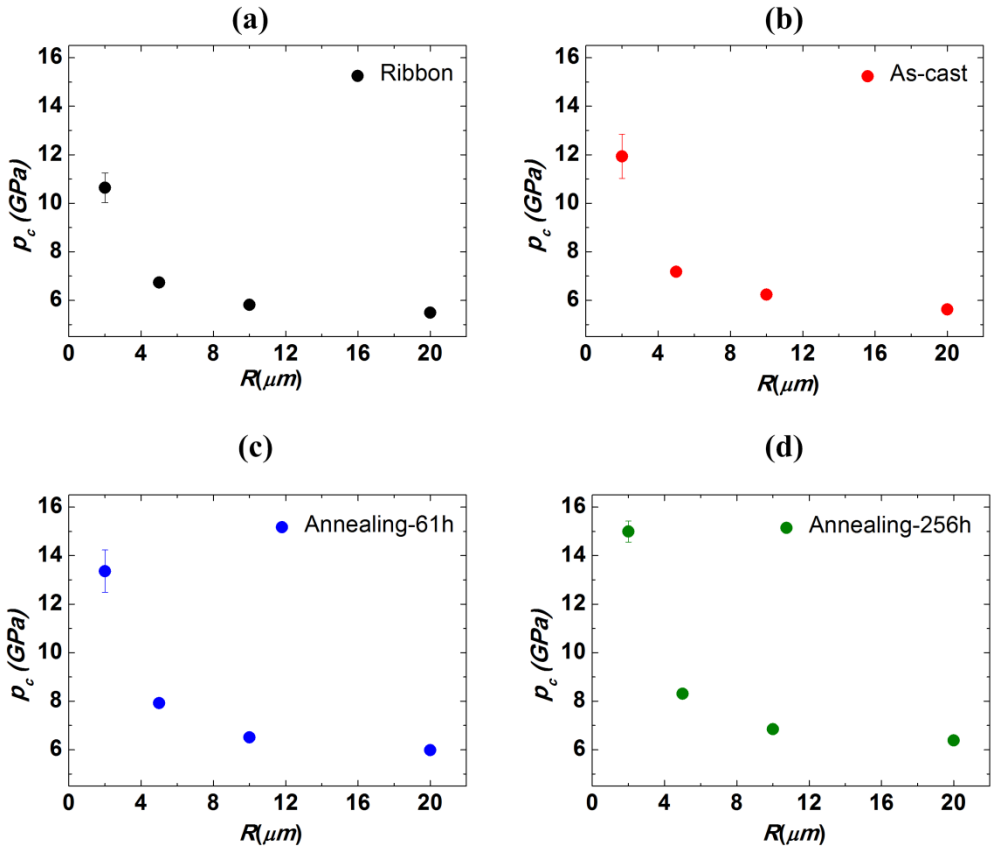

Figure 5.6 The strength size effect of the mean pressure in the different tip radius for different specimen

Figure 5.6 shows the p_c at different tip radius. For each sample, we conducted

around 10 nanoindentation tests on the sample surface. Regardless of different sample and thermal history, the measured E is roughly the same with the results from the Berkovich indentation. As shown in Fig. 5.6, the measured p_c exhibits a sharp strength size effect on both the samples with different thermal history, which increased dramatically with the decrease of the tip radius. In Chapter 3, it is obviously shows that the p_c remains at a constant value as the increased R which is equal to the hardness results from the classic Berkovich nanoindentation. So we can use hardness as p_0 which is size-independent mean pressure. According to $p_c = p_0 + C_0 E_r \left(\frac{L_{SB}}{R} \right)^{C_1}$ in Chapter 3, which predicts that *pc-p0* should scale with $1/R$ to the power of 1.45, we can now compare the experimental data to this scaling relation. As seen in Fig. 5.7, it can be seen that the prediction captures the experimental data very well for both samples. Furthermore, the shear band nucleation length L_{SB} can be extracted by fitting the experimental data to the theory. Fig. 5.8 shows a comparison of the L_{SB}, as a function of the Young's modulus E. It can be seen that L_{SB} decreases with E, which indicates the thermal history influences the nucleation size for shear band instability.

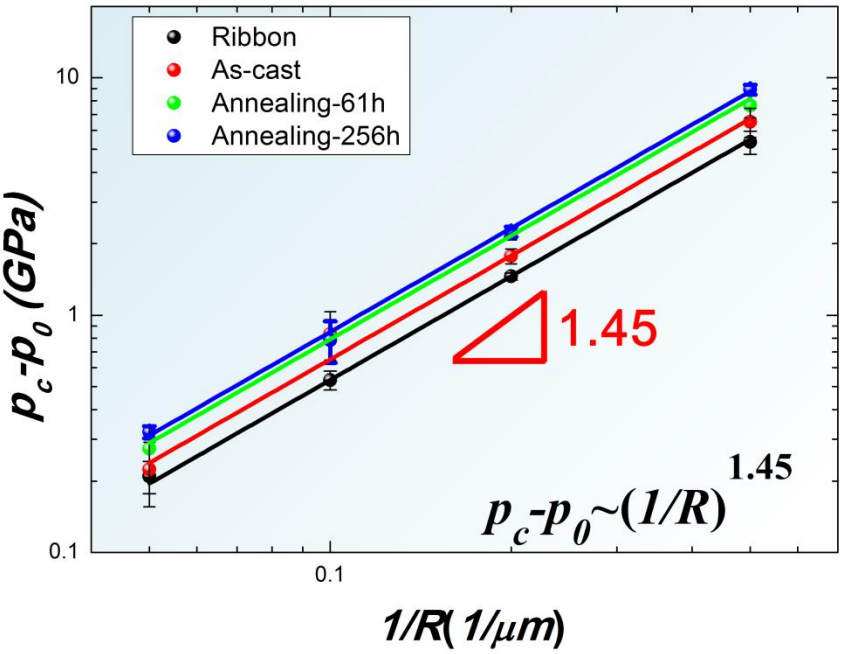

Figure 5.7 The comparison of the experimental data of *pc-p0* of different specimens versus 1/*R* with the theoretical predicted scaling ration

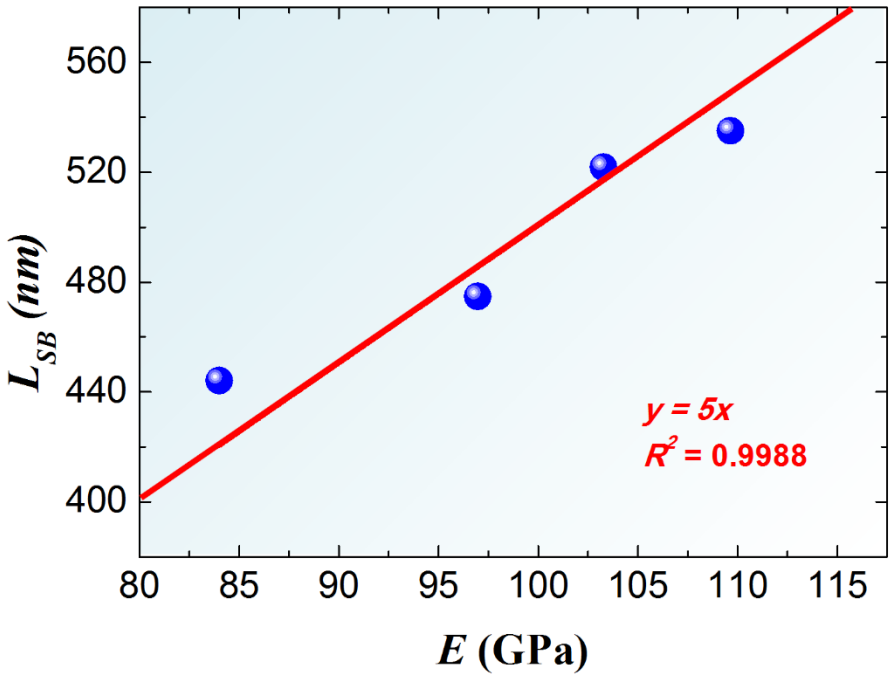

Figure 5.8 The variation of the extracted L_{SB} for four samples.

In the study of Lewandowski et al. (Lewandowski et al. 2005), it is shows that the plasticity or brittleness of metallic glass correlates with the ratio of the elastic shear modulus to bulk modulus. Annealing-induced embrittlement of metallic glasses was found, which linked to several property changes associated with structural relaxation. That is strong evidence that the embrittlement is most closely connected to the changes in elastic modulus. It has been shown that annealing-induced varies in modulus can be reversed by plastic deformation. Also Zhang(Zhang, Liu and Zhang 2006) found that fracture toughness of Pd-based thin-film metallic glass decreased with increasing annealing time. He suggests that this trend results from the gradual suppression of shear banding at the crack tip and the increase of Young's modulus with an increase of annealing time, which may lead to the decrease in the free volume required for increasing the viscosity in the shear band. So is there any relationship between the shear band formation and thermal history for metallic glass is still a question.

Based on the mechanism of shear-softening induced shear banding in MGs, Uenishi and Rice(Uenishi and Rice 2003) proposed a theoretical model for the shear softening induced instability. According to these authors (Uenishi and Rice 2003), the critical length of the shear-band embryo depends mainly on the elastic modulus of the elastic confinement and the that characterizes the strength loss in the shear-banding embryonic zone. The critical shear-band nucleation length can be derived as

$$L_{SB} = \alpha \frac{G}{\Theta} = \alpha t_{SB} \frac{G}{(\sigma_c - \sigma_r)/\varepsilon_c} = \alpha t_{SB} \frac{G}{W} \tag{5.2}$$

where α is a dimensionless factor roughly equal to ~1.16 and G is the shear modulus of the MG. Since $\Theta = (\sigma_c - \sigma_r)/\Delta$, where Δ is the critical shear displacement at which the initial softening process is completed, t_{SB} is the shear-band thickness (10-20 nm) (Zhang and Greer 2006), ε_c is the critical shear strain (=Δ/t_{SB}) and W is the linear softening rate measured in terms of the strength loss per unit shear strain (= (σ_c - σ_r)/ε_c). Taking $\alpha \sim 1$, $t_{SB} \sim 20$ nm, with different shear modulus for samples, the linear softening rate W can be extracted and we found that thermal history did not significantly change the softening rate. So the increment of critical length is mainly cause by the change of shear modulus. In previous work(Ye et al. 2010, Huo et al. 2013), their results have indicated that the structure of MGs is intrinsically heterogeneous which composed of liquid-like and solid-like regions in nanoscale. As shown in Figure 5.9, the solid-like regions (blue spheres) form an elastic matrix as the "back bone" of the MG while the liquid like regions (red spheres) encaged as flow units. It should be emphasized here that it should not be misunderstood as the real composite structure of MGs. There is no physical boundary between the liquid-like and solid-like regions. The purple spheres in Figure 5.9 are try to illustrate that there is a continuous distribution of atom packing and the whole structure is still amorphous. Compared with the solid-like region, the liquid-like region exhibits a lower packing density and local modulus. The quasi-static

shear modulus $G=G_{\infty}-G_{II}=G_{\infty}(1-\alpha)$(Huo et al. 2013), here G_{∞} is the unrelaxed shear modulus, G_{II} represents a modulus mainly from the liquid-like region and α scales with volume fraction of the liquid-like region. According to the equation above, G could increase by thermal annealing because the liquid-like regions can be reduced as shown in Figure 5.9. It shows that the liquid-like regions turns to solid-like regions after annealing. The increment of solid-like region means the increasing confinement of the elastic matrix that encapsulates the individual 'flow units' will suppress the propagation of the shear band nucleation and the critical length will be larger than the same composition which is not annealed. This variation of the critical length is mainly caused by the increment of the elastic matrix bonding. This result provides reasonable explanation for the previous studies. In Zhang's work(Zhang et al. 2006), he found the diminishing of the noticeable shear bands in the annealed sample, which indicates that a longer time annealing would potentially suppress shear banding. In my research, we found that the thermal history changes the shear band instability. With the increase of Young's modulus, the shear band will hard to form, which leads to the brittleness of metallic glass.

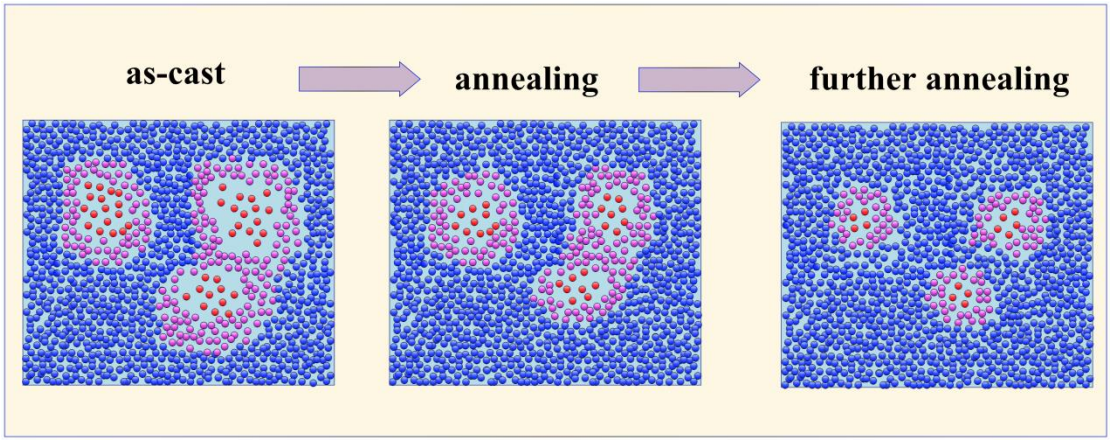

Figure 5.9 Schematic illustrations of the structure evolution of MGs (red sphere= loosely packed atom, purple sphere=less densely packed atom, blue sphere= densely packed atom)

Table 5.1 The critical length and softening rate for sample 2

Sample 02	Ribbon	As-cast	Annealing-61h	Annealing-256h
L_{SB} (nm)	~444	~474	~521	~535

5.4 Conclusion

To conclude, we extract the mechanical properties of the samples with different thermal history. It is shown that both the hardness and Young's modulus rises with increase of annealing time, while the ribbon one lower than the other three. Meanwhile, the experiment results confirm the theoretical model based on the notion of size-controlled shear-band nucleation. The shear band nucleation length extracted from the indentation size effect. The increment of solid-like region, which is caused by annealing, results in the increasing confinement of the elastic matrix that encapsulates the individual 'flow units' will suppress the propagation of the shear band nucleation and the critical length

will be larger than the same composition which is not annealed.

5.5 Reference

Argon, A. S. (1979) Plastic-Deformation in Metallic Glasses. *Acta Metallurgica,* 27**,** 47-58.

Byrne, C. J. & M. Eldrup (2008) Materials science - Bulk metallic glasses. *Science,* 321**,** 502-503.

Cheng, Y. T. & W. L. Johnson (1987) Disordered Materials - a Survey of Amorphous Solids. *Science,* 235**,** 997-1002.

Dyre, J. (2008) Mysteries of the glass transition. *Physics Today,* 61**,** 15-15.

Egami, T. (2011) Mechanical failure and glass transition in metallic glasses. *Journal of Alloys and Compounds,* 509S**,** S82-S86.

Greer, A. L. (1993) Materials Science - Confusion by Design. *Nature,* 366**,** 303-304.

Huo, L. S., J. F. Zeng, W. H. Wang, C. T. Liu & Y. Yang (2013) The dependence of shear modulus on dynamic relaxation and evolution of local structural heterogeneity in a metallic glass. *Acta Materialia,* 61**,** 4329-4338.

Lee, S. C., C. M. Lee, J. W. Yang & J. C. Lee (2008) Microstructural evolution of an elastostatically compressed amorphous alloy and its influence on the mechanical properties. *Scripta Materialia,* 58**,** 591-594.

Lewandowski, J. J., W. H. Wang & A. L. Greer (2005) Intrinsic plasticity or brittleness of metallic glasses. *Philosophical Magazine Letters,* 85**,** 77-87.

Loffler, J. F. (2003) Bulk metallic glasses (vol 11, pg 529, 2003). *Intermetallics,* 11**,** 979-979.

Oliver, W. C. & G. M. Pharr (1992) An Improved Technique for Determining Hardness and Elastic-Modulus Using Load and Displacement Sensing Indentation Experiments. *Journal of Materials Research,* 7**,** 1564-1583.

Packard, C. E., E. R. Homer, N. Al-Aqeeli & C. A. Schuh (2010) Cyclic hardening of

metallic glasses under Hertzian contacts: Experiments and STZ dynamics simulations. *Philosophical Magazine,* 90**,** 1373-1390.

Spaepen, F. (1977) Microscopic Mechanism for Steady-State Inhomogeneous Flow in Metallic Glasses. *Acta Metallurgica,* 25**,** 407-415.

Spaepen, F. (1987) The Art and Science of Microstructural Control. *Science,* 235**,** 1010-1014.

Uenishi, K. & J. R. Rice (2003) Universal nucleation length for slip weakening rupture instability under nonuniform fault loading. *J. Geophys. Res.,* 108**,** 2042.

Ye, J. C., J. Lu, C. T. Liu, Q. Wang & Y. Yang (2010) Atomistic free-volume zones and inelastic deformation of metallic glasses. *Nature Materials,* 9**,** 619-623.

Zhang, G. P., Y. Liu & B. Zhang (2006) Effect of annealing close to T-g on notch fracture toughness of Pd-based thin-film metallic glass for MEMS applications. *Scripta Materialia,* 54**,** 897-901.

6 A Critical Length Scale Controlling Homogeneous Nucleation of Shear Band for different BMGs

6.1 Introduction

Since the advent of metallic glasses (MGs)(W. Klement 1960) in the 1960s, they have been attracting extensive research interest owing to their exclusive properties such as superb strength and hardness, excellent elastic limit as well as good corrosion resistance(Byrne and Eldrup 2008, Cheng and Johnson 1987, Spaepen 1987, Dyre 2008, Greer 1993, Loffler 2003). In particular, the superior strength of MGs, as witnessed across different chemical compositions, has been taken as their hallmark. In comparison to that of crystalline metals, the high strength in MGs is commonly attributed to the lack of crystalline-like defects. By comparison, the strength of crystalline metals varies as their microstructure is tuned or their size is reduced. This strength size effect, known for crystalline metals, could be generally ascribed to the interplay between the external sizes, such as sample dimension or deformation field, and the internal sizes, such as grain size and dislocation spacing. Interestingly, MGs also exhibit a similar size effect despite the lack of any internal microstructural features. To rationalize this size effect, a number of theories have been proposed in the literature, including the early theory of Weibull statistics(Lai 2008) and the recent one entailing the nucleation energetics of shear banding(Yang, Liu and Nieh 2006). Particularly, the recent molecular dynamics (MD) simulations clearly indicate that, as the sample size reduces to the nanometer scale, the shear strength of a MG could rise up from the macroscopic value of ~G/50 to

the intrinsic strength limit of ~G/10, where G denotes the MG shear modulus.

Should the MG strength be governed by shear band nucleation, the next question is at what size a bona-fide shear band would be formed out of an embryo. Unfortunately, as of today, there is still no definitive answer to this question. According to the atomistic simulations, Li et al.(Li and Li 2007) and Shi(Shi 2010) estimated that the critical size for shear-band nucleation should be around 10-20 nm or even less. On the other hand, if the shear-band nucleation size was taken to equal the sample dimension at which the MG deformation mode transits from a localized to a distributed or even homogeneous plastic deformation, several researchers reported that the shear-band nucleation size could range from ~100 nm to ~400 nm. Noticing the large difference among the claimed shear-band nucleation sizes, one can only conclude that, at the present time, the problem of shear band nucleation in MGs is not yet fully understood. Nevertheless, there are a few issues coming to our attention, which may partially explain the aforementioned data discrepancy.

First, in most of the small-scale experiments, focused-ion-beam (FIB) fabricated micropillars were used to study the size effect. Because of the FIB damage and the non-uniform stress distribution along the micropillar, shear bands may preferentially nucleate at the sample surface or from the interface between the micropillar and the compressing platen. This scenario of heterogeneous nucleation may cause a large variation in the strength measurement, thus affecting the estimated shear-band

nucleation size. Second, the parameters used for sample preparation and testing, such as the quenching rates, applied strain or stress rate and the temperature, also vary from experiment to experiment, which may also influence shear-band nucleation. Nevertheless, how such external and internal parameters change the shear-band nucleation scenario is still largely unknown. In our current study, we aim to provide a comprehensive study of shear band nucleation in MGs.

6.2 Experiment

The nominal chemical compositions of the five BMGs are $La_{60}Al_{25}Ni_{15}$, $Au_{49}Ag_{5.5}Pd_{2.3}Cu_{26.9}Si_{16.3}$, $Pd_{40}Cu_{30}P_{20}Ni_{10,}$ $Fe_{60}Cr_{10}Mo_9C_{13}B_6Er_2$, $Fe_{60}Cr_{10}Mo_9C_{13}B_6Er_2$ and $Zr_{52.5}Ti_5Cu_{17.9}Ni_{14.6}Al_{10}$ (in at.%). For brevity, descriptions of the fabrication process are omitted here. The structure of the BMG samples was examined by X-ray diffractometry (XRD, Co radiation) before testing. The XRD patterns only display a broad diffraction maximum without any detectable sharp Bragg peaks, indicative of an overall amorphous structure. Fragility index (*m*) was investigated using differential scanning calorimetry (DSC) (Perkin Elmer, Waltham, MA; DSC 7). The local mechanical properties were first measured on the Hysitron™ NanoIndenter system (Hysitron Inc, Minneapolis, MN) with a Berkovich diamond tip. Then the spherical nanoindentation experiments were subsequently carried out at strain control on the Hysitron™ Nanoindentation System. For a systematic investigation, the following tip radii were used in the spherical indentation tests: 0.1μm, 0.4μm, 2μm,

5μm, 10μm, 20μm. In order to keep a constant strain rate, $dP/dt/P$ was set to be a constant, where dP/dt is the indentation loading rate and P the indentation load. This leads to an exponential increase of P with the time, t, in the loading segment. For simplicity, unloading was programed to follow a constant unloading rate.

6.3 Results and discussion

The hardness and modulus of five samples were first measured with a Berkovich diamond tip. To ensure data reproducibility, adjacent indentation marks were set 30μm apart. With the method of Oliver-Pharr(Oliver and Pharr 1992), the most widely used method for the extraction of hardness and modulus by Berkovich nanoindentation, the local hardness and Young‘s Modulus of all the BMG samples were measured by nanoindentation. The measured modulus and hardness values for all MG samples listed in the Table 6.1.

Table 6.1The modulus and hardness values for all MG samples

	La-based	Au-based	Pd-based	Fe-based-01	Fe-based-02
E(GPa)	44±4	90±5	~101±4	192±13	248±11.3
H(GPa)	2.7±0.3	3.8±0.3	5.7±0.4	11.9±1.5	9.9±1.3

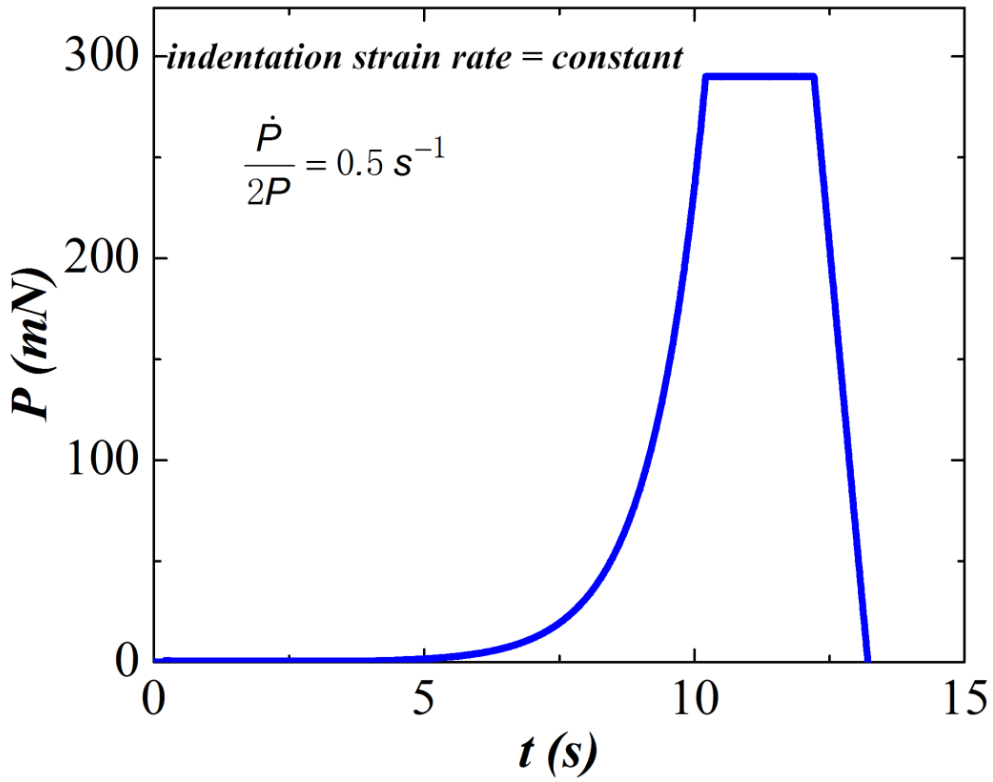

Figure 6.1 The programmed indentation load function for a constant strain-rate indentation test

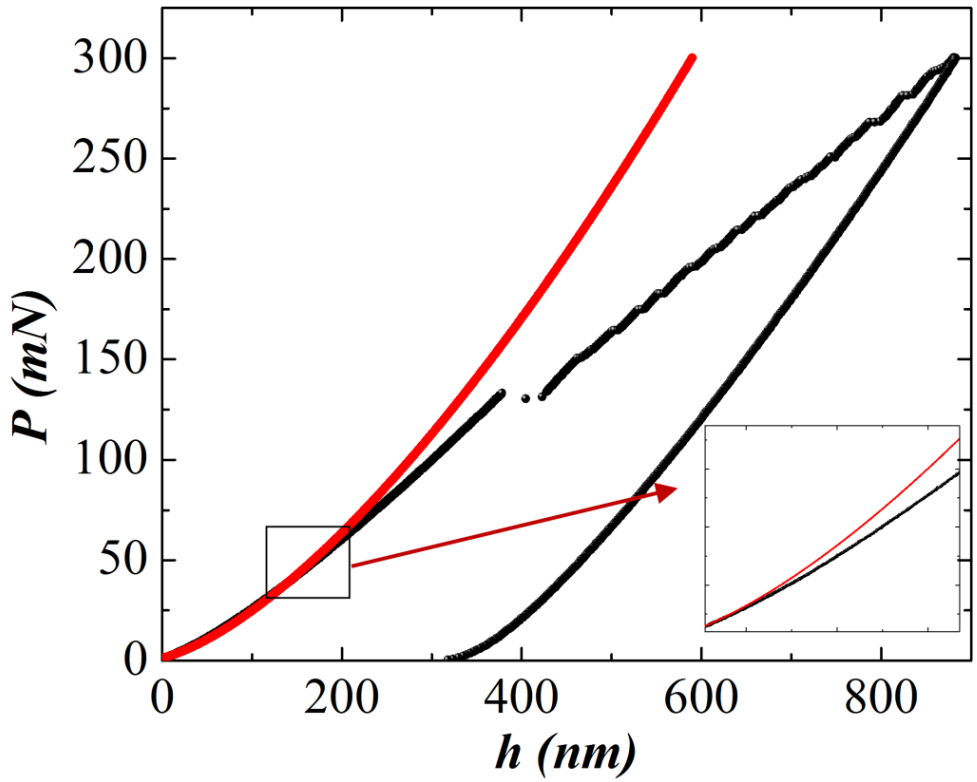

Figure 6.2 The typical indentation *P-h* curve of Pd-based sample (the black curve) in comparison with the Hertzian theory (the red curve) (inset = the enlarged view of the departure of the *P-h* curve from the Hertzian curve)

As shown in Fig 6.1, a load function with constant strain rate was employed. Figure 6.2 shows a typical load-displacement (*P-h*) curve of the Pd-based specimen at $\dot{\varepsilon} = 0.2s^{-1}$ and $R = 20\mu m$. According to the Hertzian theory, $P = (4E_rR^{1/2}/3)h^{3/2}$ for elastic indentation, where E_r denotes the reduced elastic modulus. In order to measure E_r reliably, the experimental *P-h* curve was first converted to the $P\text{-}h^{3/2}$ curve and, subsequently, the linear portion of the latter was utilized to fit out E_r via linear regression, as shown in Fig. 6.3. In this way, we can obtain E_r from the linear fitting

with a high correlation coefficient (> 98%). Afterwards, the real modulus, E, of the MG can be extracted from E_r by assuming a Poisson's ratio of ~0.397.

Once E_r is obtained, it appears that we may 'conceptually' determine the global yielding load as the departure of the experimental P-h curve from the elastic Hertzian solution. However, from the experimental viewpoint, it needs to point out that pinpointing the yielding loading P_c by examining and matching two nonlinear curves is not easy and sometimes lack of consistency. Most often, the value of P_c so obtained depends on how close you look into the details of the two curves and how many data are available near the point of cross-over Alternatively, we can extrapolate the experimental data already bypassing the yielding point backward, and the interception of the extrapolation with the elastic Hertzian solution then determines an effective yielding load P_c, as shown in Fig. 6.3. Compared to the previous method, the yielding load P_c determined this way is insensitive to the data acquisition rate and the local curvatures of the experimental curves. Here, it is worth emphasizing that the pop-in event is not corresponding to the activation of STZs. The local elastic confinement firstly breakdown and the liquid-like zone start to percolate through local confinement. Once the critical length of the shear band reached, the whole system will be global yielding. But the pop- in event is just the shear band which is though the surface of the sample.

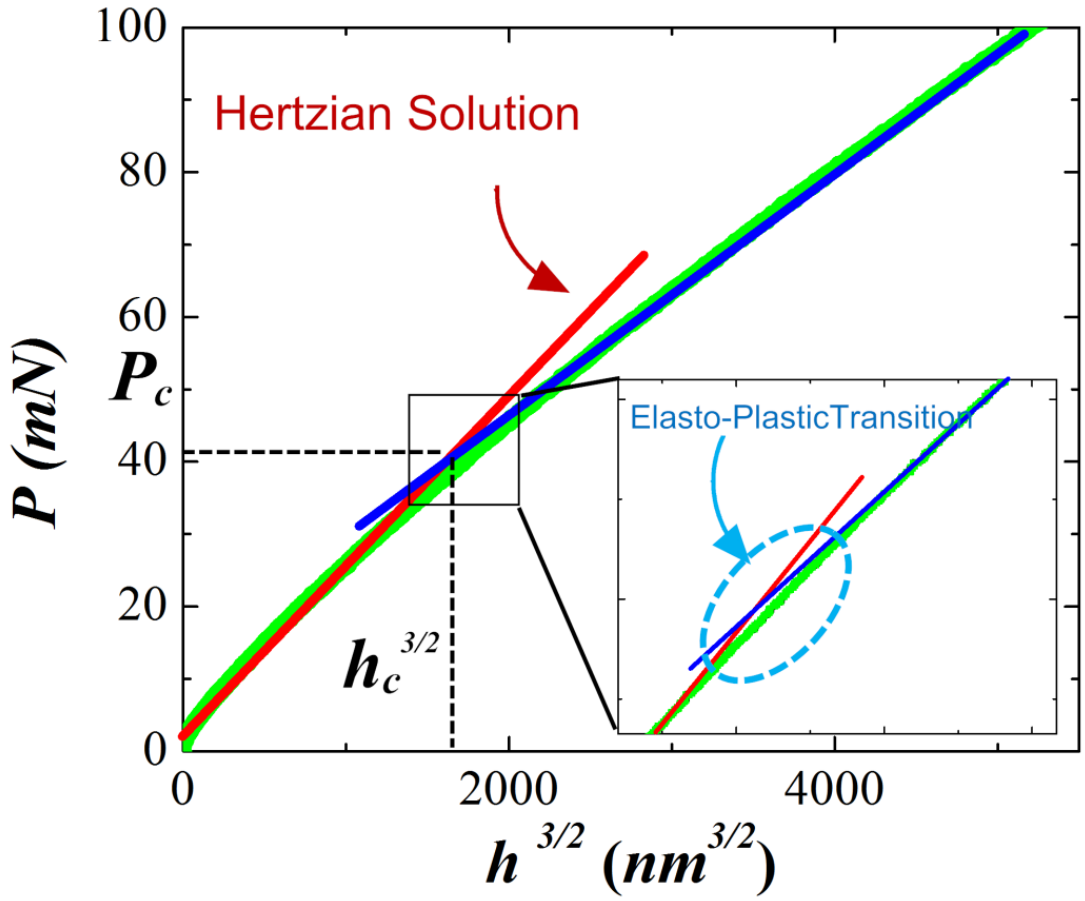

Figure 6.3 The linear fitting of the elastic portion (red curve) and the global plastic portion (blue curve) of the P-$h^{3/2}$ curve.

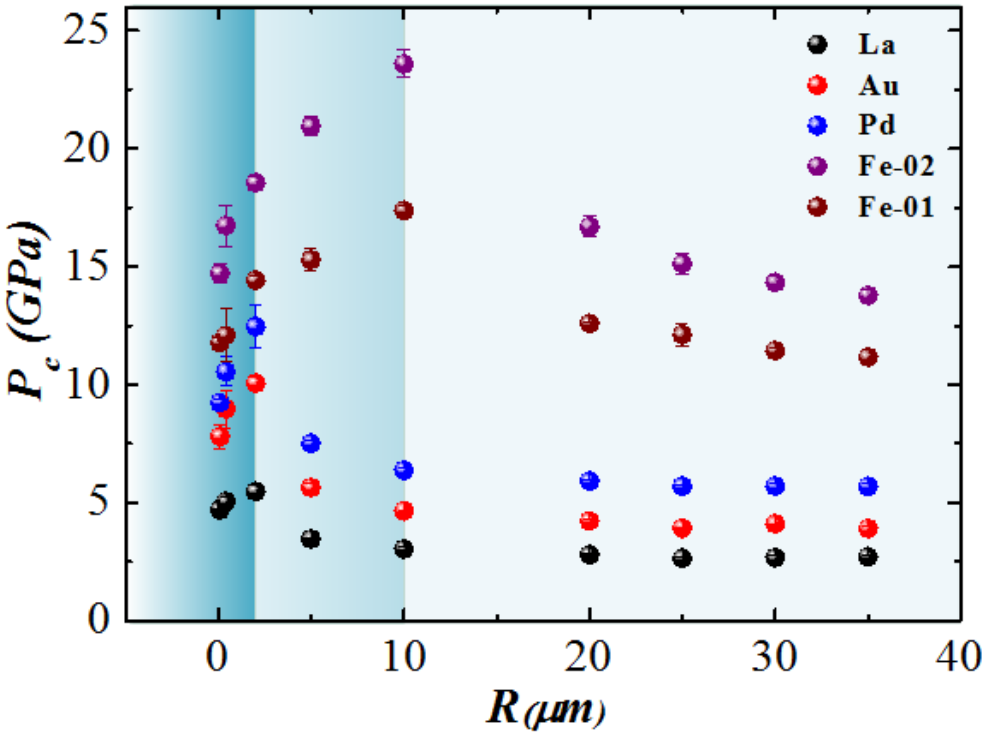

Figure 6.4 The strength size effect reverse size effect of the mean pressure in the different tip radius of different specimen

According to the Hertzian theory, the maximum pressure under the indenter is given by

$$p_c = \left(\frac{6 P \hat{E}^2}{\pi^3 R^2} \right)^{\frac{1}{3}} \tag{6.1}$$

Figure 6.4 shows the p_c at different tip radius. For each sample, we conducted around 10 nanoindentation tests were on the sample surface. Regardless of the different sample, the measured E is roughly same with the result from the Berkovich result as

shown in Table 6.1. But the different with the previous chapters is that here we employed 0.1μm and 0.4μm spherical indenters. We found the size effect which is same as previous findings when the tip radius larger than 2μm for La-， Au- and Pd-based metallic glass. In contrast, the reverse size effect was found for the tip radius at 0.1μm and 0.4μm. For the two Fe-based samples, we also found the maximum mean pressure P_c at R= 10μm. The tendency of p_c changing with R is roughly the same for all these samples. Previous research (Bei, Lu and George 2004, Wright, Saha and Nix 2001) studied the theoretical strength of metallic glasses with spherical indenter, resulting in high values of the extracted yield stress. Bei *et al.* (Bei et al. 2004) reported yield stresses over 3 times the actual shear strength for Zr-based glasses. At the same time, Wright *et al.*(Wright et al. 2001) also found that the yield stresses around 3 times the shear yielding stress for different Zr- based glass. Compared with relatively large testing volume for conventional experiment, they attribute the discrepancy to the small probing volume in nanoindentation experiments, which are likely to be defect free. In other's work (Bei et al. 2010), it is found that maximum shear stress decreases with increasing indenter radius. This is a possible consequence of the increased probability of finding defects in the highly stressed zone underneath the indenter which increases with increasing indenter size. In the study of Packard(Packard and Schuh 2007), he found a reverse size effect, in which smaller indentations return somewhat lower yield strengths. So the reason for these conflicts should be uncovered. From the dimensional consideration, the plastic zone size scales with the tip radius, *R*, of the spherical indenter for a given indentation mean pressure p_c. In that regard, a size effect arises if different

sized indenters are used to deform the same MG. For large sized indenters, the overall and local yielding points roughly the same with each other because plastic zone size could be already sufficient to initiate shear instability. In this size regime, the strength or hardness of MGs can be effectively attributed to the activation of local plasticity events for either the models such as free-volume (Spaepen 1977) and shear transformation zone model (Argon 1979), and the recent models based on structural heterogeneity (Liu, Yang and Liu 2013, Huo et al. 2013). However, for small-sized indenters, we must consider the size different with plastic zone and the critical length. The subcritical growth of such small local plastic zone which needed to trigger shear instability is easily touching the surface boundary. As a result, the mean pressure p_c will show a reverse size effect once the indenter size near or lower than the critical length. At the same time, we also should consider the surface imperfections, which play an important role if the yield occurs not in the bulk beneath the indentation, but via a shear band that actually connects with the surface. As the indentation size is reduced, the relative importance of surface irregularities increases, and lower measured strengths could be expected. For the indenter size of 0.1μm and 0.4μm, like a berkovich indenter, the plastic deformation is easily formed even the indent force is extremely small.

In Chapter 3, it is obviously shows that the p_c remains at a constant value as the increased R which is equal to the hardness results from the classic Berkovich nanoindentation. So we can use hardness as p_0 which is size-free mean pressure. We fit the L_{SB} with the part of the p_c decrease with the increase of the tip radius. According to

$p_c = p_0 + C_0 E_r \left(\frac{L_{SB}}{R} \right)^{C_1}$ in Chapter 3 which predicts that *pc-p0* should scale with 1/*R* to the power of 1.45, we can now compare the experimental data to this scaling relation. It should be noticed that we use the size effect part to fit the $L_{SB.}$ The prediction captures the experimental data very well for both samples. Furthermore, the shear band nucleation length L_{SB} can be extracted by fitting the experimental data to the theory. Fig. 6.5 shows a comparison of the L_{SB} for various MGs.

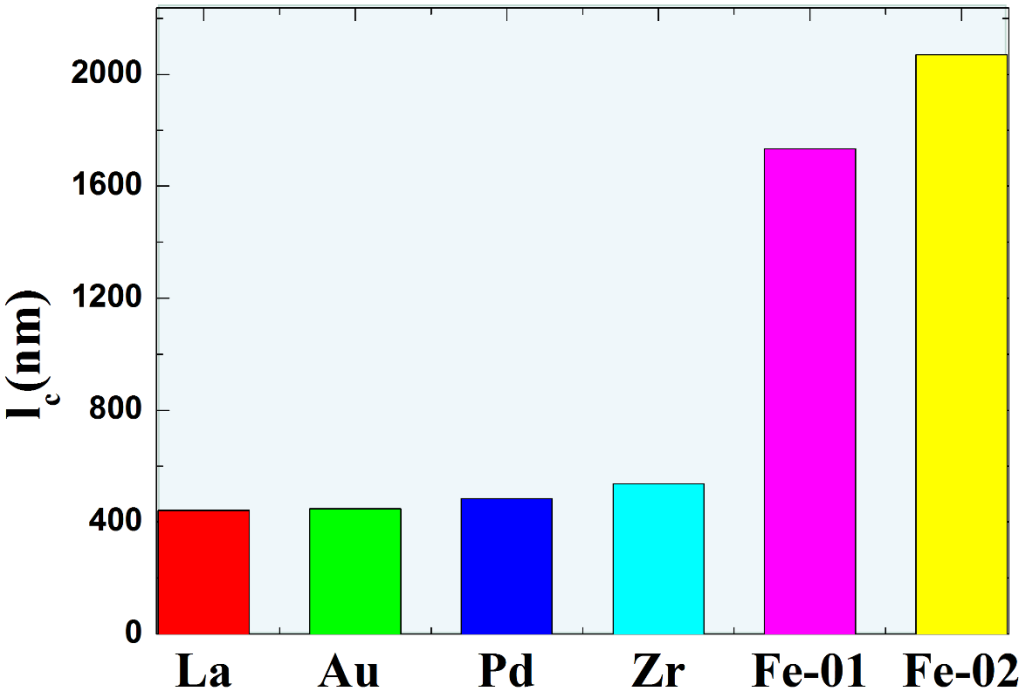

Figure 6.5 The comparison of L_{SB} for six different samples

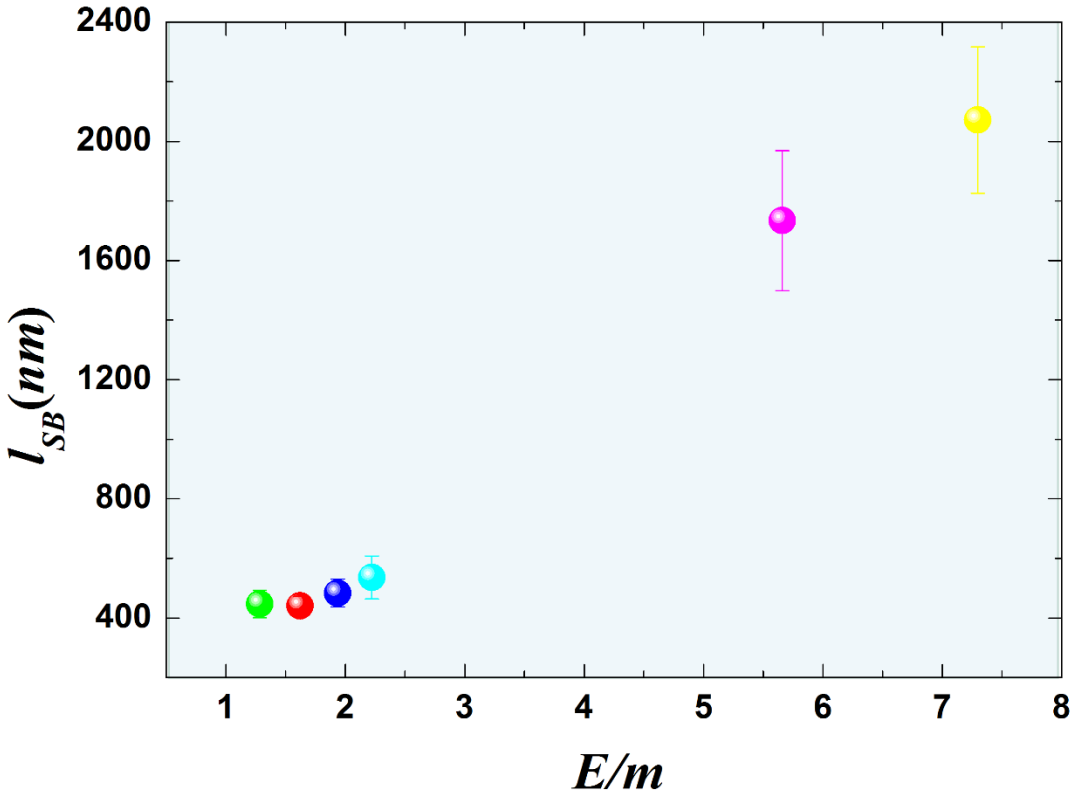

Figure 6.6The relationship between critical length L_{SB} and E/m

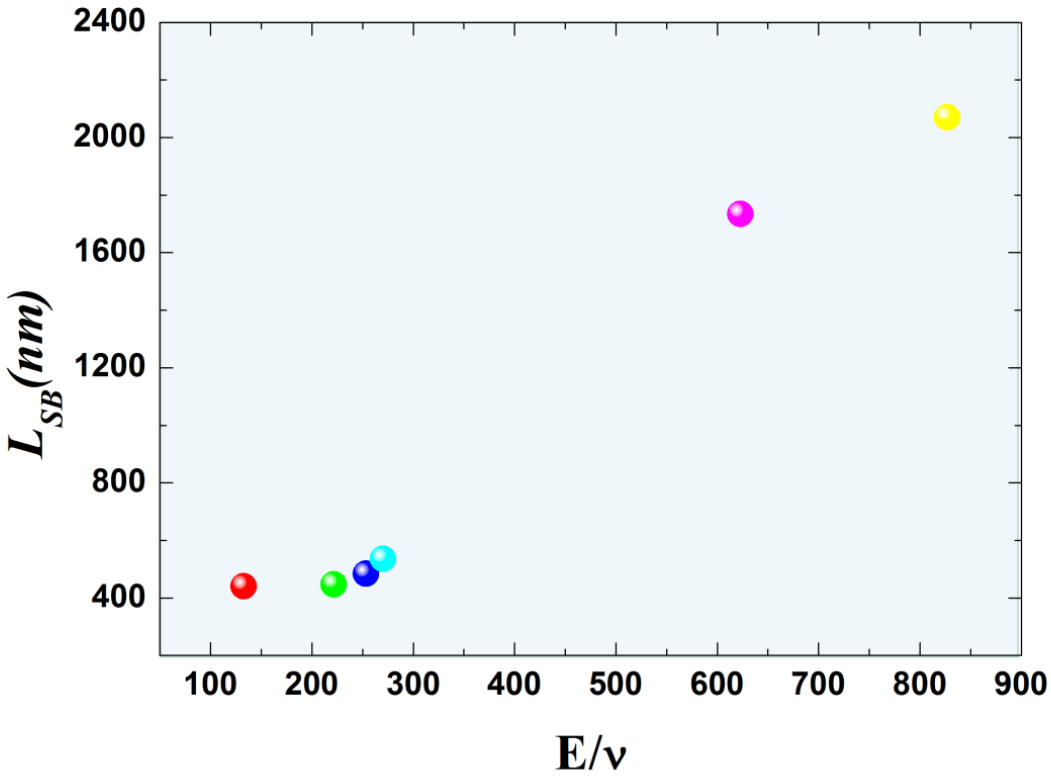

Figure 6.7 The relationship between critical length L_{SB} and E/m

In Table 6.2, we summarized the fragility m and passion ratio for all the samples, including the Zr-based which we have discussed in previous chapter. The fragility of metallic glass has been extensively studied to link the liquid dynamics and the property. Fragility of liquids is defined as the change of viscosity, η, with the temperature approaching T_g of glass forming liquids. (Angell 1985)

$$m = \left. \frac{d \log_{10} \eta}{d(Tg/T)} \right|_{T = Tg} \tag{6.2}$$

The strong glass is one which viscosity obeying Arrhenius law, such as SiO_2, while fragile glasses deviate from Arrhenius. Most of BMG alloys are classified into

intermediate glass. Novikov(Novikov and Sokolov 2004) reported a correlation between fragility m and ν for a variety of glass-forming systems, showing fragility m increasing with ν. So in the following part we are trying to link the shear band nucleation with the fragility and Poisson's ratio. In previous chapter we have discussed the process of shear band nucleation with the atomic-scale softening mechanism. In principle, the mechanism of 'shear-softening-induced-instability' applies not only to shear banding in MGs but also to a similar defect nucleation process in many other types of materials

Table 6.2 The fragility and Poisson's ratio values for all MG samples

	La- based	Au- based	Pd- based	Zr- based	Fe-based-01	Fe-based-02
m	27	70	52	45	34	34
ν	0.33	0.406	0.404	0.37	0.309	0.3

Based on the theoretical model of Uenishi and Rice(Uenishi and Rice 2003) , the critical length of the shear-band embryo depends mainly on two factors. One is the elastic modulus of the surrounding media that confines the subcritical growth of the embryo, and the other is the softening rate that characterizes the strength loss in the shear-banding embryonic zone. So from the equation $L_{SB} = \alpha \frac{G}{\Theta}$, we can found that any change in modulus G or softening rate Θ could result in the variation in L_{SB}. We focus on relationship between the softening rate, fragility and Poisson's ratio. Figures 6.6 and 6.7 shows the relationship between the L_{SB} , E , m and v. It could be found that several BMGs exhibits a linear correlation between L_{SB} and E/m, and the correlation between

L_{SB} and E/m shows the same tendency. We know that the large plastic bulk metallic glasses BMGs usually have larger Poisson's ratio. From the energy aspect, the activation energy barrier is relatively lower for operation of a small cluster of randomly close-packed atoms. From the atomic viewpoint, due to the weak atomic bonding, fragile MGs needs less de-bonding energy which creates a localized distortion of the surrounding atoms and triggers the formation of shear band embryo. For a fragile MG with higher Poisson's ratio and fragility m, it comprises more loose-packed regions for triggering the activation of STZs. This means lowering activation energy compared with that of strong BMGs. So the nucleation length for fragile BMG is relatively smaller than that of the strong one and better plasticity expected. In Egami's(Egami 2006) work, he assumes that the local heating within the shear band embryo is enough to make the temperature in the band exceeding the glass transition temperature. For the fragile MGs with larger Poisson's ratio, the viscosity of liquid will quickly decrease. The softening rate in the shear band embryonic zone is relatively high for fragile MGs. And this high strength loss will results in the smaller shear band nucleation length. At the same time, the STZ volumes of plastic flow of BMGs are also found to increase with Poisson's ratio ν(Pan et al. 2008). This means that a larger STZ volume compared with small one enables a lesser number of STZs to be activated for nucleation of a shear band. Thus STZ with a large size reinforce the shear capability of the metallic glass and promote the formation of multiple shear bands. So the MGs with a higher fragility and Poisson's ratio represent a higher possibility for a BMG to have better plasticity and to form shear band.

6.4 Reference

Angell, C. A. (1985) Spectroscopy Simulation and Scattering, and the Medium Range Order Problem in Glass. *Journal of Non-Crystalline Solids,* 73**,** 1-17.

Argon, A. S. (1979) Plastic deformation in metallic glasses. *Acta Metallurgica,* 27**,** 47-58.

Bei, H., Z. P. Lu & E. P. George (2004) Theoretical strength and the onset of plasticity in bulk metallic glasses investigated by nanoindentation with a spherical indenter. *Physical Review Letters,* 93.

Bei, H., Z. P. Lu, S. Shim, G. Chen & E. P. George (2010) Specimen Size Effects on Zr-Based Bulk Metallic Glasses Investigated by Uniaxial Compression and Spherical Nanoindentation. *Metallurgical and Materials Transactions a-Physical Metallurgy and Materials Science,* 41A**,** 1735-1742.

Byrne, C. J. & M. Eldrup (2008) Materials science - Bulk metallic glasses. *Science,* 321**,** 502-503.

Cheng, Y. T. & W. L. Johnson (1987) Disordered Materials - a Survey of Amorphous Solids. *Science,* 235**,** 997-1002.

Dyre, J. (2008) Mysteries of the glass transition. *Physics Today,* 61**,** 15-15.

Egami, T. (2006) Formation and deformation of metallic glasses: Atomistic theory. *Intermetallics,* 14**,** 882-887.

Greer, A. L. (1993) Materials Science - Confusion by Design. *Nature,* 366**,** 303-304.

Huo, L. S., J. F. Zeng, W. H. Wang, C. T. Liu & Y. Yang (2013) The dependence of shear modulus on dynamic relaxation and evolution of local structural heterogeneity in a metallic glass. *Acta Materialia,* 61**,** 4329-4338.

Lai, Y. H. A.-L., C.J. AU - Cheng, Y.T. AU - Chou, H.S. AU - Chen, H.M. AU - Du, X.H. AU - Chang, C.I. AU - Huang, J.C. AU - Jian, S.R. AU - Jang (2008) Bulk and microscale compressive behavior of a Zr-based metallic glass. *Scripta Materialia* 58.

Li, Q. K. & M. Li (2007) Assessing the critical sizes for shear band formation in metallic glasses from molecular dynamics simulation. *Applied Physics Letters,* 91.

Liu, Z., Y. Yang & C. Liu (2013) Yielding and shear banding of metallic glasses. *Acta Materialia,* 61**,** 5928-5936.

Loffler, J. F. (2003) Bulk metallic glasses (vol 11, pg 529, 2003). *Intermetallics,* 11**,** 979-979.

Novikov, V. N. & A. P. Sokolov (2004) Poisson's ratio and the fragility of glass-forming liquids. *Nature,* 431**,** 961-963.

Oliver, W. C. & G. M. Pharr (1992) An Improved Technique for Determining Hardness and Elastic-Modulus Using Load and Displacement Sensing Indentation Experiments. *Journal of Materials Research,* 7**,** 1564-1583.

Packard, C. E. & C. A. Schuh (2007) Initiation of shear bands near a stress concentration in metallic glass. *Acta Materialia,* 55**,** 5348-5358.

Pan, D., A. Inoue, T. Sakurai & M. W. Chen (2008) Experimental characterization of shear transformation zones for plastic flow of bulk metallic glasses. *Proceedings of the National Academy of Sciences of the United States of America,* 105**,** 14769-14772.

Shi, Y. F. (2010) Size-independent shear band formation in amorphous nanowires made from simulated casting. *Applied Physics Letters,* 96.

Spaepen, F. (1977) A microscopic mechanism for steady state inhomogeneous flow in metallic glasses *Acta Metallurgica,* 25**,** 407-415.

Spaepen, F. (1987) The Art and Science of Microstructural Control. *Science,* 235**,** 1010-1014.

Uenishi, K. & J. R. Rice (2003) Universal nucleation length for slip weakening rupture instability under nonuniform fault loading. *J. Geophys. Res.,* 108**,** 2042.

W. Klement, R. H. W., P.O.L. Duwez (1960). *Nature,* 187**,** 869-870.

Wright, W. J., R. Saha & W. D. Nix (2001) Deformation mechanisms of the Zr40Ti14Ni10Cu12Be24 bulk metallic glass. *Materials Transactions,* 42**,** 642-649.

Yang, B., C. T. Liu & T. G. Nieh (2006) Unified equation for the strength of bulk metallic glasses. *Applied Physics Letters,* 88.

7 Conclusion and future work

The objective of this thesis was to provide quantitative insights into the shear-band nucleation mechanism in different glassy alloy systems. I was conducted carefully designed nanoindentation test with different tip radius. Various factors, such as strain rate, residual stress and thermal history, were studied. I try to figure out their effects on the shear band nucleation.

Firstly, I try to develop a theoretical model based on the notion of size-controlled shear-band nucleation to account for the indentation size effect in MGs. Through carefully designed experiments, this model prediction is justified on the Zr-based MG. By fitting the experimental data to the theory, we are able to extract the shear-band nucleation length from the trend of indentation size effect for different indentation strain rates. Our results show that shear band nucleation in the Zr-based MG exhibits slight rate dependence, which can be rationalized by the rate-affected shear softening behavior in MGs. It is worth pointing out that the experimental/theoretical framework herein established is rather general and should be applicable to other MG alloys or even other types of glassy materials, as long as an appropriate constitutive relation is available for describing the local yielding of the glassy material.

For the residual stress effect, we can extract the mechanical properties from the compressive to tensile site, it is shown that the material's elastic modulus keeps at a

constant while its hardness drops more significantly in the compression region than that in the tension region. The trend of indentation size effect for varies residual stress was found. Our results show that shear band nucleation in the Zr-based MG influenced by the presence of compression or tension residual stress, which can be rationalized by the different shear softening rate in MGs. It indicates that compressive residual stress tends to slightly increase the nucleation size for shear band instability.

For the thermally history effect, the hardness increases with annealing time and the ribbon one lower than the other three, demonstrating that denser structure has a higher hardness. Meanwhile, with the increasing annealing time, the Young's modulus increases. We can found that thermal history effect on the nucleation length which is not caused by the significantly change of the softening rate, but the variation of Young's modulus.

At last, I conduct nanoindentation test on various MGs with nine different spherical indenters. I found the size effect which is same as previous findings for large indenters while the reverse size effect was found for smaller one. And the changing point is different for different MGs. Also I found the shear band nucleation length is related with the fragility and Poisson's ratio. The MGs with a higher fragility and Poisson's ratio represent a higher possibility for a BMG to have better plasticity and to form shear band.

Because of the limitation of period and instruments, our recent studies are only focused on the shear band nucleation mechanism at room temperature. It is expected that, by raising experimental temperature, especially approaching the glass transition temperature, the shear band nucleation length may change significantly. Secondly, the structural heterogeneity can be depicted as a nano-scale composite-like structure, which consists of loose- and dense-packing regions. What happens to MGs if these flow units are repeatedly activated in the apparent ‘elastic’ regime. Should the MGs be weakened, we will be facing a problem similar to fatigue nucleation; or, on the contrary, we might find that the MGs can be strengthened by the repeatedly motion of the flow units. At last, if I applied the electrical signal on spherical indenter, it may help me to study the nucleation behavior more clearly. The resolution for the displacement is extremely high compare to the conventional equipment. With nanoECR, the current will be change when the voltage keeps constant. I will analysis the change of the current curve and try to figure out the behavior of the nucleation of shear band and find more details.